Numerical Simulations of Electron Plasma Waves in Semiconductor Devices

Von der Fakultät für Elektrotechnik und Informationstechnik
der Rheinisch-Westfälischen Technischen Hochschule Aachen

zur Erlangung des akademischen Grades eines

Doktors der Ingenieurwissenschaften

genehmigte Dissertation

vorgelegt von

Tobias Linn, M.Sc.

aus Essen, Deutschland

Berichter
Univ.-Prof. Dr.-Ing. Christoph Jungemann
Associate Prof. Sung-Min Hong

Tag der mündlichen Prüfung: 28.03.2022

Contents

Abstract

Motivation, Goal and Task of the Dissertation

The frequency range between about 0.1 THz and 10 THz of the electromagnetic spectrum is commonly referred to as the THz-region. Although there are many promising applications in fields such as security, spectroscopy, communication technology, medicine, biochemistry and more, the efficient generation of THz-radiation is still a challenging task. With rising frequency the efficiency of traditional electronic oscillators diminishes, while for optical devices the opposite is true. This leads to a frequency region, where no efficient method of generation is known, the so-called THz-gap.

In their influental paper from 1993, Dyakonov and Shur theoretically investigated electron plasma oscillations in semiconductor devices, and drew an analogy with the shallow water equations. By applying asymmetric boundary conditions, they predicted the formation of an electron plasma instability, with an oscillation frequency in the THz-range. Devices that exhibit this instability could then be used to efficiently generate THz-radiation. Therefore, the mechanism was proposed as a major step towards closing the THz-gap. Furthermore, the passive detection of THz-waves using such plasma oscillations is another important application.

The goal of this work is the theoretical investigation of electron plasma effects in semiconductor devices by using multiple different models for the electron transport. These models are to be evaluated in terms of their accuracy compared to the Boltzmann transport equation, by applying them to the simple homogeneous device model used by Dyakonov and Shur. In addition, more advanced numerical device simulations are to be perfomed. To that end, a completely new numerical scheme needs to be developed, since commonly used numerical stabilization schemes do not work when plasma effects are included in the transport model.

Major Scientific Contributions

In this work, multiple transport models of various complexity are derived from and compared to the Boltzmann transport equation. The Dyakonov-Shur plasma instability is investigated and it is shown, that it is most likely just an artifact stemming from the improper application of unrealistic boundary conditions. Nevertheless, in the second part of the thesis, numerical device simulations are performed, with the main focus on the development of a novel numerical stabilization scheme. Despite the relative simplicity of the considered transport models, the inclusion of plasma effects fundamentally changes the type of partial differential equations from parabolic to hyperbolic, for which no known stabilization exists in the context of device simulation. Typically, hyperbolic equations often arise in the field of computational fluid dynamics. Therefore, some of the methodologies from that field are adapted to solving the semiconductor device equations. This is, however, not a straightforward process, due to certain properties exhibited by the equations. For instance, in semiconductor devices the carrier density can vary over many orders of magnitude within very small transition regions. Related to that, large source terms occur in the equations, which are usually missing in fluid dynamics. Among other things, the stability problems resulting from these effects are solved within this work. In addition to a low-order numerical scheme, a high-order scheme with superior properties is developed as well. The numerical scheme is also extended from one to two dimensions. Since the developed method is quite general, it can be (and in parts already is) adapted to more advanced equations commonly used for device simulation, e.g. the Boltzmann transport equation.

List of Publications

[1] T. Linn, Z. Kargar, and C. Jungemann, “Investigation of moments-based transport models applied to plasma waves and the Dyakonov–Shur instability,” Semiconductor Science and Technology, vol. 34, no. 1, p. 014002, 2018

[2] T. Linn, K. Bittner, H.-G. Brachtendorf, and C. Jungemann, “Simulation of THz oscillations in semiconductor devices based on balance equations,” Journal of scientific computing, vol. 85, no. 1, pp. 1–15, 2020

[3] C. Jungemann, T. Linn, K. Bittner, and H.-G. Brachtendorf, “Numerical investigation of plasma effects in silicon MOSFETs for THz-wave detection,” Solid-State Electronics, vol. 128, pp. 129–134, 2017

[4] Z. Kargar, T. Linn, D. Ruić, and C. Jungemann, “Investigation of transport modeling for plasma waves in THz devices,” IEEE Transactions on Electron Devices, vol. 63, no. 11, pp. 4402–4408, 2016

[5] Z. Kargar, D. Ruić, T. Linn, and C. Jungemann, “Numerical simulation of plasma waves in a quasi-2D electron gas based on the Boltzmann transport equation,” Journal of Computational Electronics, vol. 16, no. 3, pp. 487–496, 2017

[6] Z. Kargar, T. Linn, and C. Jungemann, “Investigation of the Dyakonov–Shur instability for THz wave generation based on the Boltzmann transport equation,” Semiconductor Science and Technology, vol. 33, no. 10, p. 104001, 2018

[7] M. Noei, T. Linn, and C. Jungemann, “A numerical approach to quasi-ballistic transport and plasma oscillations in junctionless nanowire transistors,” Journal of Computational Electronics, vol. 19, no. 3, pp. 975–986, 2020

[8] M. Noei, T. Linn, P. Luckner, and C. Jungemann, “A Godunov-type stabilization scheme for large-signal simulations of a THz nanowire transistor based on the Boltzmann equation," IEEE Transactions on Electron Devices, vol. 68, no. 11, pp. 5407–5413, 2021

[9] M. Noei, P. Luckner, T. Linn, and C. Jungemann, "Numerical aspects of a Godunov-type stabilization scheme for the Boltzmann transport equation," Journal of Computational Electronics, in press

Notation

x	Scalar quantity
$\boldsymbol{x}$	Vector quantity
$\mathbf{X}$	Matrix quantity
$\underline{x}$	Complex quantity
$\langle x \rangle$	Expected value
$\overline{x}$	Average value
$\widetilde{x}$	Fluctuation, i.e. deviation from average
x^*	Interface value, computed by Riemann solver
x^{s}	Stationary value
x^{d}	Dynamic value
$\mathcal{J}\{\boldsymbol{f}, \boldsymbol{x}\}$	Jacobian matrix, i.e. the derivatives of $\boldsymbol{f}$ w.r.t. $\boldsymbol{x}$
$\operatorname{Div} \boldsymbol{x}$	Surface divergence, defined as $\operatorname{Div} \boldsymbol{x} = \boldsymbol{n}_{1,2} \cdot (\boldsymbol{x}_2 - \boldsymbol{x}_1)$, where $\boldsymbol{x}_1$ and $\boldsymbol{x}_2$ are given by the vector $\boldsymbol{x}$ evaluated on the two sides of a surface, and $\boldsymbol{n}_{1,2}$ is the normal vector of that surface pointing from side 1 to side 2. $\operatorname{Div} \boldsymbol{x} = 0$ implies that the normal component of $\boldsymbol{x}$ is continuous across the surface.
$\operatorname{Rot} \boldsymbol{x}$	Surface rotation, defined as $\operatorname{Rot} \boldsymbol{x} = \boldsymbol{n}_{1,2} \times (\boldsymbol{x}_2 - \boldsymbol{x}_1)$, similar to $\operatorname{Div} \boldsymbol{x}$. $\operatorname{Rot} \boldsymbol{x} = \boldsymbol{0}$ implies that the tangential components of $\boldsymbol{x}$ are continuous across the surface.

Symbols

c	Speed of Light
c_0	Vacuum Speed of Light

c_{T}	Thermal Velocity
C	Capacitance
$\boldsymbol{D}$	Electric Flux Density
e	Positive Elementary Charge
$\boldsymbol{E}$	Electric Field
ε	Electrostatic Permittivity
ε_0	Vacuum Permittivity
ε_{r}	Relative Permittivity
ϵ	Kinetic Energy
f	Frequency, Distribution Function
$\boldsymbol{F}$	Force, Flux Term
H	Hamilton Function
$\hbar$	Reduced Planck Constant
I	Current
$\boldsymbol{j}$	Particle Current Density
$\boldsymbol{k}$	Wave Vector
k_{B}	Boltzmann Constant
L	Length
m^*	Effective Mass
m_{e}	Electron Mass
μ	Mobility
μ_{r}	Relative Permeability
n	Electron Density
N_{A}	Acceptor Concentration
N_{D}	Donator Concentration
n_{i}	Intrinsic Carrier Density
N_{G}	Number of Gauss-Legendre Nodes

ν	Fundamental Solution to the Laplace Equation
ω	Angular Frequency
Ω	Size of a Finite Volume
p	Hole Density
$\boldsymbol{p}$	Momentum
φ	Electrostatic Potential
Φ	Quasi Fermi Potential
ϕ_{MS}	Metal-Semiconductor Workfunction Difference
$\underline{q}$	Plasma Wave Number
$\boldsymbol{r}$	Position Vector
ϱ	Charge Density
s	Shock Wave Speed
$\underline{s}$	Complex Frequency
$S\{f\}$	Scattering Term
$\boldsymbol{S}$	Energy Current Density, Source Term
σ	Growth-Factor
t	Time
T	Temperature
T^*	Dynamic Temperature
T_0	Lattice Temperature
τ	Scattering/Relaxation Time
$\boldsymbol{U}$	Vector of Transport Variables
$\boldsymbol{V}$	Vector of Characteristic Transport Variables
V	Voltage
V_{appl}	Applied Voltage
V_{T}	Thermal Voltage
v	Velocity

v_{d}	Drift Velocity
v_{sat}	Saturation Velocity
W	Energy Density
w	Gauss-Legendre Weight
ξ	Gauss-Legendre Node
$\underline{Y}$	Admittance

Acronyms

2DEG Two-dimensional Electron Gas

BOX Buried Oxide Layer

BTE Boltzmann Transport Equation

CCFVM Cell-Centered Finite-Volume Method

CDD Convective Drift-Diffusion

CHD Convective Hydrodynamic

DD Drift-Diffusion

FET Field Effect Transistor

FVM Finite-Volume Method

HD Hydrodynamic

KCL Kirchhoff Current Law

LDLR Local Double Logarithmic Reconstruction

ME Maxwell Equation

MOSFET Metal-Oxide-Semiconductor Field-Effect Transistor

NLPE Non-Linear Poisson Equation

ODE Ordinary Differential Equation

PDE Partial Differential Equation

PE Poisson Equation

PSS Periodic Steady-State

QCL Quantum Cascade Laser

QFP Quasi-Fermi Potential

SG Scharfetter-Gummel

SHE Spherical Harmonics Expansion

SOI Silicon-On-Insulator

TCAD Technology Computer-Aided Design

TB Thermal Bath

TM Ten Moments

VCFVM Vertex-Centered Finite-Volume Method

1 Introduction

The frequency range of about 0.1 THz up to 10 THz from the electromagnetic spectrum is often referred to as the THz region. Waves from that frequency region can easily penetrate many materials like plastic or paper, while being strongly absorbed by water. These unique properties lead to many promising applications not only in security, spectroscopy, communications but also in medicine and biochemistry. Unfortunately, they prove to be very difficult to generate efficiently. While for traditional electronic oscillators based on solid-state devices (e.g. the sources in [10] or [11]) the efficiency diminishes with rising frequency, for optical devices like Quantum Cascade Lasers (QCLs) it is the opposite case, with diminishing efficiency for falling frequency. This leads to the formation of the so-called THz-gap (see Figure 1.1), where no efficient method of generation is known.

To solve this efficiency problem, Dyakonov and Shur proposed a novel mechanism for THz-wave generation, using the oscillations of the electron plasma in semiconductor devices. Under the right conditions, they predicted an instability which would then lead to the emission of THz-waves [13, 14]. To increase efficiency even further, several more advanced geometries have been proposed [15, 16].

While to the author's knowledge an efficient device operating under this principle has not yet been experimentally shown, in [17, 18, 19] at least the detection of THz-waves by passive resistive mixing was successfully demonstrated, by implementing an actual THz-wave camera operating at about 600 GHz.

A simple way, often used to simulate such devices, is the transmission line approach [18], where the device is replaced by an equivalent circuit, resulting in a single differential equation. This might be sufficient if only qualitative results are needed, however, for more accurate results and especially when more advanced geometries are considered, the actual microscopic electron transport should be modeled.

Accurate results could be gained from transient simulations of the Boltzmann Transport Equation (BTE). However, at this point this is still computationally too demand-

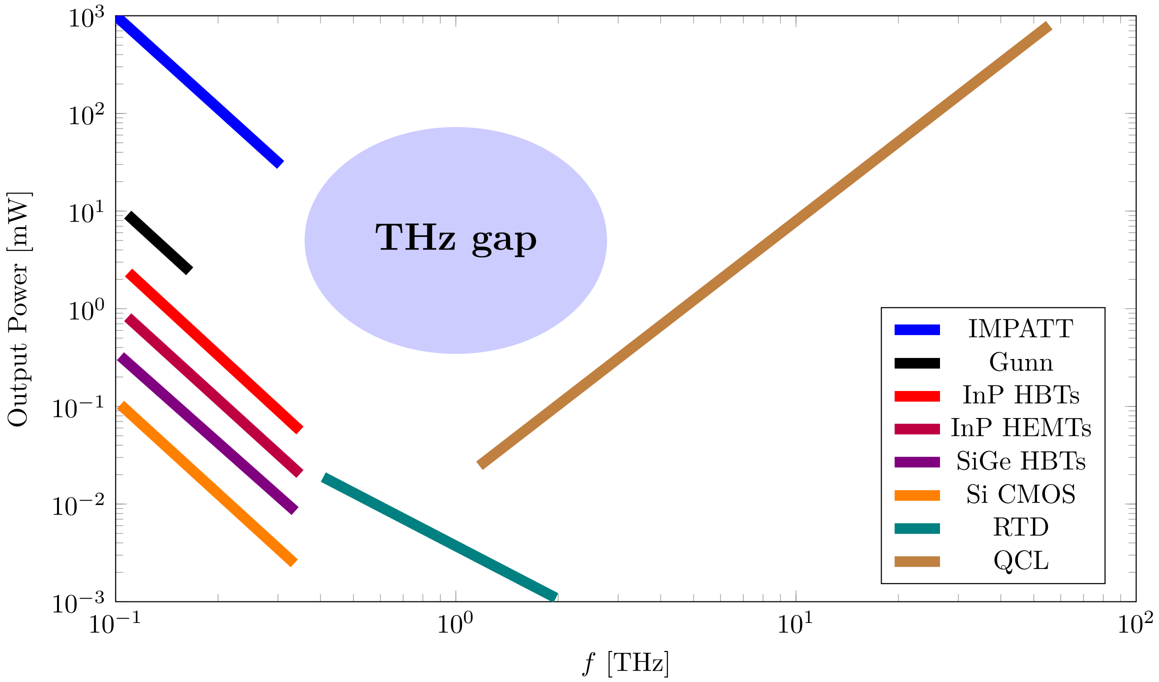

Figure 1.1: Typical output power for various electronic and optical device types at different frequencies [12].

ing, especially in more than one dimension of transport. Alternatively, simplified transport models based on the moments of the BTE, like the Drift-Diffusion (DD) or the Hydrodynamic (HD) model, can be used. These models are also extensively used in commercially available Technology Computer-Aided Design (TCAD) simulators, e.g. Sentaurus Device, though such simulators usually employ rather drastic approximations. For instance, certain time derivatives are neglected, which effectively suppresses any plasma oscillations. This is done to improve the computational efficiency as well as the numerical stability, but at the same time it renders such simulators useless, when plasma effects are to be studied. In this work such moments-based transport models are investigated, but without the usual approximations.

The thesis is structured as follows: In the second chapter the theoretical background of the used equations is outlined. Using the BTE, several moments-based transport models of varying complexity are derived, all of which include the terms necessary to describe plasma oscillations. The instability predicted by Dyakonov and Shur is investigated for homogeneous devices, and the models are compared to results gained from homogeneous BTE simulations. Finally, the influence of the boundary conditions is investigated.

In the third chapter, a stable numerical discretization scheme for one-dimensional devices with a hyperbolic transport model is developed. Results for an N^+-N-N^+-device are calculated and discussed.

In the fourth chapter the discretization scheme is extended to two dimensions, and results for a double-gate Metal-Oxide-Semiconductor Field-Effect Transistor (MOSFET) and a Silicon-On-Insulator (SOI) device are shown.

The last chapter contains a conclusion as well as an outlook.

2 Theoretical Background

To simulate semiconductor devices, a suitable model that includes all the relevant physical effects is needed. Such a model usually leads to a system of coupled Partial Differential Equations (PDEs), which subsequently can be discretized and solved numerically. To be able to describe electron plasma oscillations, the model must first of all include electromagnetic effects, which are described by the Maxwell Equations (MEs). Furthermore, electron transport effects must be included. A well-suited transport model for the nearly mesoscopic devices considered in this work is the semi-classical BTE.

In this chapter, it is shown that the MEs can be approximated by the simpler electrostatic Poisson Equation (PE). In addition to that, due to the high computational cost involved in the solution of the BTE, multiple simplified transport models based on its moments are derived. These models are then applied to a simple device with a homogeneous channel, and the prediction of a plasma instability by Dyakonov and Shur [13, 14, 20] is investigated. Finally the influence of the boundary conditions on the predicted instability is shown.

2.1 Poisson Equation

The speed of light in a medium is given by

$$c = \frac{c_0}{\sqrt{\varepsilon_\mathrm{r}\,\mu_\mathrm{r}}}\,, \tag{2.1}$$

where $c_0 \approx 3 \cdot 10^8\,\mathrm{m/s}$ is the vacuum speed of light, ε_r the relative permittivity and μ_r the relative permeability. In a typical semiconductor, like silicon or gallium arsenide, they are approximately given by $\varepsilon_\mathrm{r} \approx 10$ and $\mu_\mathrm{r} \approx 1$, which results in

$$c \approx 1 \cdot 10^8\,\mathrm{m/s}\,. \tag{2.2}$$

Therefore, for a typical device length of about $L = 1\,\mathrm{\mu m}$, the time it takes for an electromagnetic signal to propagate through the whole device is about

$$t_\mathrm{light} = \frac{L}{c} \approx 1 \cdot 10^{-14}\,\mathrm{s}\,, \tag{2.3}$$

or, expressed as a frequency,

$$f_\mathrm{light} = \frac{1}{t_\mathrm{light}} \approx 100\,\mathrm{THz}\,. \tag{2.4}$$

Since the usual frequencies considered in this work are on the order of $f \approx 1\,\mathrm{THz}$, which is well below f_light, the wave nature of light can be neglected, and it is assumed to propagate instantaneously.

Introducing a quasi-stationary electrostatic potential $\varphi(\boldsymbol{r}, t)$, the electric field is then given by

$$\boldsymbol{E}(\boldsymbol{r}, t) = -\boldsymbol{\nabla}\varphi(\boldsymbol{r}, t)\,, \tag{2.5}$$

where the potential fulfills the PE

$$\boldsymbol{\nabla} \cdot \boldsymbol{D} = -\boldsymbol{\nabla} \cdot (\varepsilon \boldsymbol{\nabla}\varphi) = \varrho\,, \tag{2.6}$$

with the electric flux density $\boldsymbol{D} = \varepsilon\boldsymbol{E} = \varepsilon_\mathrm{r}\varepsilon_0\boldsymbol{E}$ and the charge density ϱ. In a semiconductor, the charge density can be expressed by

$$\varrho = e\,(N_\mathrm{D} - N_\mathrm{A} - n + p)\,, \tag{2.7}$$

where e is the positive elementary charge, N_D and N_A are the donator and acceptor doping concentrations, and n and p the electron and hole densities. Often, instead of n and p, the Quasi-Fermi Potentials (QFPs) for both electrons and holes (Φ^n and Φ^p) are used. The QFPs are defined by the nonlinear transformations

$$n = n_\mathrm{i} \exp\left(\frac{\varphi - \Phi^\mathrm{n}}{V_\mathrm{T}}\right) \quad \text{and} \quad p = n_\mathrm{i} \exp\left(\frac{\Phi^\mathrm{p} - \varphi}{V_\mathrm{T}}\right), \tag{2.8}$$

where n_i is the intrinsic carrier density specific to the semiconductor material and $V_\mathrm{T} = \frac{k_\mathrm{B} T_0}{e}$ is the thermal voltage, with the Boltzmann constant k_B and the lattice temperature T_0.

2.2 Boltzmann Transport Equation

To model electron transport (or transport phenomena in general), solving the BTE is the method of choice, when the requirements for physical accuracy are high and effects like quantum mechanical tunneling can be ignored. It describes, how an ensemble of particles, specified by the particle distribution function $f(\boldsymbol{r}, \boldsymbol{k}, t)$, behaves over time under the influence of external forces and scattering events. Even though the particles are not treated as waves, and obey Newton's laws of motion, instead of the classical momentum $\boldsymbol{p}$ often the quantum mechanical wave vector $\boldsymbol{k}$ is used. Furthermore, the included scattering mechanisms can take quantum mechanical effects into account, with transition rates usually being calculated by Fermi's golden rule. This is why the BTE is often called semi-classical.

The BTE is given by the first-order PDE [21, 22]

$$\left(\frac{\partial}{\partial t} + \boldsymbol{F}^\top \frac{1}{\hbar} \boldsymbol{\nabla}_{\boldsymbol{k}} + \boldsymbol{v}^\top \boldsymbol{\nabla}_{\boldsymbol{r}}\right) f(\boldsymbol{r}, \boldsymbol{k}, t) = S\{f\} \,, \tag{2.9}$$

where $\boldsymbol{F} = \boldsymbol{F}(\boldsymbol{r}, \boldsymbol{k}, t)$ is the external force, $\boldsymbol{v} = \boldsymbol{v}(\boldsymbol{r}, \boldsymbol{k})$ is the particle velocity and $S\{f\}$ is the scattering term. It incorporates all relevant scattering processes, with the most important being electron-phonon interactions and impurity scattering. No further details about it are given here, since in the later derived moments-based transport models, it is approximated quite drastically by a single or multiple macroscopic relaxation times.

Using the Hamilton function $H(\boldsymbol{r}, \boldsymbol{k}, t)$, describing the total energy of a particle, the force and velocity can be expressed as

$$\boldsymbol{F} = -\boldsymbol{\nabla}_{\boldsymbol{r}} H \quad \text{and} \quad \boldsymbol{v} = \frac{1}{\hbar} \boldsymbol{\nabla}_{\boldsymbol{k}} H \,, \tag{2.10}$$

with the reduced Planck constant $\hbar$. In this work, a simple isotropic effective mass approximation is made for both electrons and holes, resulting in parabolic bands. The Hamilton function for electrons and holes is then

$$\begin{aligned} H_\mathrm{n}(\boldsymbol{r}, \boldsymbol{k}, t) &= \epsilon_\mathrm{n} - e\,\varphi(\boldsymbol{r}, t) = \frac{\hbar^2 \boldsymbol{k}^2}{2 m_\mathrm{n}^*} - e\,\varphi(\boldsymbol{r}, t) \\ H_\mathrm{p}(\boldsymbol{r}, \boldsymbol{k}, t) &= \epsilon_\mathrm{p} + e\,\varphi(\boldsymbol{r}, t) = \frac{\hbar^2 \boldsymbol{k}^2}{2 m_\mathrm{p}^*} + e\,\varphi(\boldsymbol{r}, t) \,, \end{aligned} \tag{2.11}$$

where $\epsilon_{\mathrm{n,p}}$ is the kinetic energy and $m^*_{\mathrm{n,p}}$ is the scalar effective mass of electrons and holes, respectively. The forces and velocities are therefore given by

$$\boldsymbol{F}_{\mathrm{n}} = -e\,\boldsymbol{E}\,, \quad \boldsymbol{F}_{\mathrm{p}} = e\,\boldsymbol{E} \quad \text{and} \quad \boldsymbol{v}_{\mathrm{n,p}} = \frac{\hbar\,\boldsymbol{k}}{m^*_{\mathrm{n,p}}}\,. \tag{2.12}$$

2.3 Balance equations

Even though the BTE is well suited for describing electron transport in semiconductors, its dimensionality is prohibitively large. For three-dimensional devices, the complete phase space is actually seven-dimensional, with three dimensions for both $\boldsymbol{r}$ and $\boldsymbol{k}$, as well as one time dimension. To reduce the dimensionality, the BTE can be projected onto a finite number of moments, thus removing the $\boldsymbol{k}$-dependency. Together with appropriate closure relations, this strategy can be used to derive simplified transport models.

Using the placeholder $X(\boldsymbol{k})$ for either a scalar or vectorial microscopic quantity, balance equations for electrons [23, 24, 25, 22, 1]

$$\frac{\partial x}{\partial t} + e\,n \left\langle \frac{1}{\hbar} \boldsymbol{\nabla}_{\boldsymbol{k}} X^{\top} \right\rangle_{\boldsymbol{k}}^{\top} \boldsymbol{E} + \left(\boldsymbol{\nabla}_{\boldsymbol{r}}^{\top} n \left\langle \boldsymbol{v} X^{\top} \right\rangle_{\boldsymbol{k}} \right)^{\top} = -\frac{x - x_{\mathrm{eq}}}{\tau_x} \tag{2.13}$$

can be derived, where expressions in angled brackets are integrated over the full $\boldsymbol{k}$-space. Corresponding to the microscopic quantity $X(\boldsymbol{k})$, the macroscopic quantity $x = x(\boldsymbol{r}, t)$ is given by

$$x(\boldsymbol{r}, t) = n \left\langle X(\boldsymbol{k}) \right\rangle_{\boldsymbol{k}} = \frac{2}{(2\pi)^3} \iiint X(\boldsymbol{k}) f(\boldsymbol{r}, \boldsymbol{k}, t) \,\mathrm{d}^3 k \ , \tag{2.14}$$

where the 2 in the numerator is the spin degeneracy factor. The scattering term is approximated using a corresponding macroscopic relaxation time τ_x for each moment and the equilibrium value

$$x_{\mathrm{eq}} = \frac{2}{(2\pi)^3} \iiint X(\boldsymbol{k}) f_{\mathrm{eq}}(\boldsymbol{r}, \boldsymbol{k}, t) \,\mathrm{d}^3 k \ . \tag{2.15}$$

For $X = 1$ the continuity equation can be derived

$$\frac{\partial n}{\partial t} + \boldsymbol{\nabla} \cdot \boldsymbol{j} = 0\,, \tag{2.16}$$

where $n(\boldsymbol{r}, t) = n \left\langle 1 \right\rangle_{\boldsymbol{k}}$ is the electron density and $\boldsymbol{j}(\boldsymbol{r}, t) = n \left\langle \boldsymbol{v} \right\rangle_{\boldsymbol{k}}$ is the electron current density. Consequently, the next microscopic quantity to consider is therefore $X = \boldsymbol{v}$, leading to a balance equation for $\boldsymbol{j}$

$$\frac{\partial \boldsymbol{j}}{\partial t} + \frac{e}{m^*} n \boldsymbol{E} + \left(\boldsymbol{\nabla}_{\boldsymbol{r}}^{\top} n \left\langle \boldsymbol{v} \boldsymbol{v}^{\top} \right\rangle_{\boldsymbol{k}} \right)^{\top} = -\frac{\boldsymbol{j}}{\tau_{\mathrm{j}}}\,. \tag{2.17}$$

The next moment typically used is the kinetic energy $X = \epsilon$ and correspondingly the macroscopic energy density $x = W$:

$$\frac{\partial W}{\partial t} + e\boldsymbol{j} \cdot \boldsymbol{E} + \boldsymbol{\nabla} \cdot \boldsymbol{S} = -\frac{W - W_{\mathrm{eq}}}{\tau_{\mathrm{W}}}\,, \tag{2.18}$$

where $W_{\mathrm{eq}} = \frac{3}{2} k_{\mathrm{B}} T_0 n$ is the energy density at equilibrium, and $\boldsymbol{S} = n \left\langle \epsilon \boldsymbol{v} \right\rangle_{\boldsymbol{k}}$ is the energy current density. The final balance equation considered here is then given by

$$\frac{\partial \boldsymbol{S}}{\partial t} + \frac{e}{m^*} W \boldsymbol{E} + e\, n \left\langle \boldsymbol{v}\boldsymbol{v}^\top \right\rangle_{\boldsymbol{k}} \boldsymbol{E} + \left(\boldsymbol{\nabla}_{\boldsymbol{r}}^\top n \left\langle \epsilon \boldsymbol{v}\boldsymbol{v}^\top \right\rangle_{\boldsymbol{k}} \right)^\top = -\frac{\boldsymbol{S}}{\tau_{\mathrm{S}}}\,. \tag{2.19}$$

To get a set of closed equations, appropriate closure relations for the remaining unknown terms $n \left\langle \boldsymbol{v}\boldsymbol{v}^\top \right\rangle_{\boldsymbol{k}}$ and $n \left\langle \epsilon \boldsymbol{v}\boldsymbol{v}^\top \right\rangle_{\boldsymbol{k}}$ need to be derived, i.e. expressions depending on the moments n, $\boldsymbol{j}$, W and $\boldsymbol{S}$ must be found.

2.3.1 Drift-Diffusion Model

For the DD model, only the moments $n(\boldsymbol{r}, t)$ and $\boldsymbol{j}(\boldsymbol{r}, t)$, and correspondingly eqs. (2.16) and (2.17) are considered. To close this set of two equations, an expression for $n \left\langle \boldsymbol{v}\boldsymbol{v}^\top \right\rangle_{\boldsymbol{k}}$ in terms of n and $\boldsymbol{j}$ is needed. By making an assumption for the distribution function, it can be directly calculated. For the DD model, a Maxwellian distribution with a temperature equal to the lattice temperature is assumed

$$f_{\mathrm{DD}}(\boldsymbol{r}, \boldsymbol{k}, t) = f_{\mathrm{DD},0} \exp\left(-\frac{\hbar^2 \boldsymbol{k}^2}{2 m^* k_{\mathrm{B}} T_0} \right)\,, \tag{2.20}$$

where $f_{\mathrm{DD},0} = f_{\mathrm{DD},0}(\boldsymbol{r}, t)$ is chosen such that f_{DD} is consistent with the electron density

$$\begin{aligned} n \left\langle 1 \right\rangle_{\boldsymbol{k}}^{\mathrm{DD}} &= \frac{2}{(2\pi)^3} \iiint f_{\mathrm{DD}}(\boldsymbol{r}, \boldsymbol{k}, t)\, \mathrm{d}^3 k \overset{!}{=} n \\ \implies f_{\mathrm{DD},0} &= \frac{1}{2}\, n \sqrt{\left(\frac{2\pi\hbar^2}{m^* k_{\mathrm{B}} T_0} \right)^3}\,. \end{aligned} \tag{2.21}$$

The missing term is then calculated by explicitly performing the integration [1]

$$\begin{aligned} n\left\langle \boldsymbol{v}\boldsymbol{v}^\top \right\rangle_{\boldsymbol{k}}^{\mathrm{DD}} &= \frac{2}{(2\pi)^3}\iiint \boldsymbol{v}\boldsymbol{v}^\top f_{\mathrm{DD}}(\boldsymbol{r},\boldsymbol{k},t)\,\mathrm{d}^3k \\ &= \frac{\hbar^2}{m^{*2}}\,n\sqrt{\left(\frac{\hbar^2}{2\pi m^* k_{\mathrm{B}}T_0}\right)^3}\iiint \boldsymbol{k}\boldsymbol{k}^\top \exp\left(-\frac{\hbar^2\boldsymbol{k}^2}{2m^*k_{\mathrm{B}}T_0}\right)\mathrm{d}^3k \\ &= \frac{k_{\mathrm{B}}T_0}{m^*}\,n\,\hat{\boldsymbol{I}}\,, \end{aligned} \tag{2.22}$$

where the off-diagonal elements $\boldsymbol{k}\boldsymbol{k}^\top$ are odd functions, resulting in zero off-diagonals after integration. This expression is then inserted into eq. (2.17)

$$\frac{\partial \boldsymbol{j}}{\partial t} + \frac{e}{m^*}n\boldsymbol{E} + \frac{k_{\mathrm{B}}T_0}{m^*}\boldsymbol{\nabla} n = -\frac{\boldsymbol{j}}{\tau_{\mathrm{j}}}\,, \tag{2.23}$$

which together with eq. (2.16) constitutes the hyperbolic DD model. Neglection of the time derivative of the current density results in the classical DD model

$$\boldsymbol{j} = -\mu(n\boldsymbol{E} + V_{\mathrm{T}}\boldsymbol{\nabla} n)\,, \tag{2.24}$$

with the electron mobility $\mu = \frac{e\tau_{\mathrm{j}}}{m^*}$.

2.3.2 Convective Drift Diffusion Model

The distribution function used in eq. (2.20) is an even function, and therefore inconsistent with a non-zero current density, because [1]

$$n\left\langle \boldsymbol{v} \right\rangle_{\boldsymbol{k}}^{\mathrm{DD}} = \frac{2}{(2\pi)^3}\iiint \frac{\hbar\boldsymbol{k}}{m^*} f_{\mathrm{DD}}(\boldsymbol{r},\boldsymbol{k},t)\,\mathrm{d}^3k = 0\,. \tag{2.25}$$

To address this problem, the distribution can be shifted, which breaks its symmetry

$$f_{\mathrm{CDD}}(\boldsymbol{r},\boldsymbol{k},t) = f_{\mathrm{DD},0}\exp\left(-\frac{\hbar^2(\boldsymbol{k}-\boldsymbol{k}_0)^2}{2m^*k_{\mathrm{B}}T_0}\right), \tag{2.26}$$

where the scaling factor is the same as before, because the shift does not change the zeroth moment of the distribution function. The shift $\boldsymbol{k}_0 = \boldsymbol{k}_0(\boldsymbol{r},t)$ results in an additional degree of freedom, and is chosen such that

$$\begin{aligned} n\left\langle \boldsymbol{v} \right\rangle_{\boldsymbol{k}}^{\mathrm{CDD}} =& \frac{2}{(2\pi)^3} \iiint \frac{\hbar \boldsymbol{k}}{m^*} f_{\mathrm{CDD}}(\boldsymbol{r}, \boldsymbol{k}, t)\, \mathrm{d}^3 k = \frac{\hbar}{m^*} \boldsymbol{k}_0 n \overset{!}{=} \boldsymbol{j} \neq 0 \\ \Longrightarrow\ \boldsymbol{k}_0 =& \frac{m^*}{\hbar} \frac{\boldsymbol{j}}{n}\,. \end{aligned} \tag{2.27}$$

Like before, the missing term is obtained by calculating the integral [1]

$$\begin{aligned} n\left\langle \boldsymbol{v}\boldsymbol{v}^\top \right\rangle_{\boldsymbol{k}}^{\mathrm{CDD}} &= \frac{2}{(2\pi)^3} \iiint \boldsymbol{v}\boldsymbol{v}^\top f_{\mathrm{CDD}}(\boldsymbol{r}, \boldsymbol{k}, t)\, \mathrm{d}^3 k \\ &= \frac{k_{\mathrm{B}} T_0}{m^*}\, n\, \hat{\boldsymbol{I}} + \frac{\boldsymbol{j}\boldsymbol{j}^\top}{n}\,. \end{aligned} \tag{2.28}$$

Compared to eq. (2.22), there is an extra term $\frac{\boldsymbol{j}\boldsymbol{j}^\top}{n}$, resulting in the constitutive equation

$$\frac{\partial \boldsymbol{j}}{\partial t} + \frac{e}{m^*} n \boldsymbol{E} + \frac{k_{\mathrm{B}} T_0}{m^*} \boldsymbol{\nabla} n + \left(\boldsymbol{\nabla}^\top \frac{\boldsymbol{j}\boldsymbol{j}^\top}{n} \right)^\top = -\frac{\boldsymbol{j}}{\tau_{\mathrm{j}}}\,. \tag{2.29}$$

This model is called Convective Drift-Diffusion (CDD) model, since the additional term $\left(\boldsymbol{\nabla}^\top \frac{\boldsymbol{j}\boldsymbol{j}^\top}{n} \right)^\top$ is related to the transfer of heat in the electron gas (convection).

2.3.3 Hydrodynamic Model

Up until now, the electron gas temperature in the assumed distribution function was fixed to the lattice temperature T_0. However, acceleration and subsequent scattering of electrons can lead to heating of the electron gas, well above the lattice temperature. To take this effect into account, the energy and energy current density as well as the corresponding balance equations should also be considered, resulting in the HD model. As a start, a similar distribution function as for the DD model is used [1]

$$f_{\mathrm{HD}}(\boldsymbol{r}, \boldsymbol{k}, t) = f_{\mathrm{HD},0} \exp\left(-\frac{\hbar^2 \boldsymbol{k}^2}{2 m^* k_{\mathrm{B}} T^*} \right), \tag{2.30}$$

with the dynamic temperature [26] $k_{\mathrm{B}} T^* = \frac{2}{3} \frac{W}{n}$, as opposed to the lattice temperature (for $W = W_{\mathrm{eq}}$ they coincide: $k_{\mathrm{B}} T^*_{\mathrm{eq}} = k_{\mathrm{B}} T_0$). Replacing T_0 by T^*, the results from eqs. (2.21) and (2.22) can be reused

$$f_{\mathrm{HD},0} = \frac{1}{2} n \sqrt{\left(\frac{2\pi\hbar^2}{m^* k_\mathrm{B} T^*}\right)^3} \tag{2.31}$$

$$n \left\langle \boldsymbol{v}\boldsymbol{v}^\top \right\rangle_{\boldsymbol{k}}^{\mathrm{HD}} = \frac{k_\mathrm{B} T^*}{m^*} n \,\hat{\boldsymbol{I}} = \frac{2}{3m^*} W \,\hat{\boldsymbol{I}} \,. \tag{2.32}$$

Additionally [1],

$$n \left\langle \epsilon \boldsymbol{v}\boldsymbol{v}^\top \right\rangle_{\boldsymbol{k}}^{\mathrm{HD}} = \frac{10}{9m^*} \frac{W^2}{n} \hat{\boldsymbol{I}} \tag{2.33}$$

is calculated in a similar way. Together with eqs. (2.16) and (2.18), the HD model is then given by

$$\frac{\partial \boldsymbol{j}}{\partial t} + \frac{e}{m^*} n \boldsymbol{E} + \frac{2}{3m^*} \boldsymbol{\nabla} W = -\frac{\boldsymbol{j}}{\tau_\mathrm{j}} \tag{2.34}$$

$$\frac{\partial \boldsymbol{S}}{\partial t} + \frac{5e}{3m^*} W \boldsymbol{E} + \frac{10}{9m^*} \boldsymbol{\nabla} \frac{W^2}{n} = -\frac{\boldsymbol{S}}{\tau_\mathrm{S}} \,. \tag{2.35}$$

2.3.4 Convective Hydrodynamic Model

Just like f_DD, f_HD is inconsistent with a non-zero current density. To alleviate this issue, shifting the distribution by the same $\boldsymbol{k}_0$ as before [1] yields

$$f_\mathrm{CHD}(\boldsymbol{r}, \boldsymbol{k}, t) = f_{\mathrm{CHD},0} \exp\left(-\frac{\hbar^2 (\boldsymbol{k} - \boldsymbol{k}_0)^2}{2m^* k_\mathrm{B} T}\right), \tag{2.36}$$

where

$$f_{\mathrm{CHD},0} = \frac{1}{2} n \sqrt{\left(\frac{2\pi\hbar^2}{m^* k_\mathrm{B} T}\right)^3} \,. \tag{2.37}$$

The energy density is then given by the thermal energy, in addition to the kinetic energy resulting from the average drift velocity $\frac{\boldsymbol{j}}{n}$:

$$n \left\langle \epsilon \right\rangle_{\boldsymbol{k}}^{\mathrm{HD}} = n \left(\frac{3}{2} k_\mathrm{B} T + \frac{1}{2} m^* \frac{\boldsymbol{j}^2}{n^2}\right) \overset{!}{=} W \tag{2.38}$$

$$\implies k_\mathrm{B} T = \frac{2}{3} \frac{W}{n} - \frac{1}{3} m^* \frac{\boldsymbol{j}^2}{n^2} \,. \tag{2.39}$$

Note, that the distribution function is now consistent with n, $\boldsymbol{j}$ and W, but not with $\boldsymbol{S}$, which would need three additional degrees of freedom. The unknown terms are given by [1]

$$n \left\langle \boldsymbol{v}\boldsymbol{v}^\top \right\rangle_{\boldsymbol{k}}^{\mathrm{CHD}} = \frac{k_\mathrm{B}T}{m^*} n \hat{\boldsymbol{I}} + \frac{\boldsymbol{j}\boldsymbol{j}^\top}{n} = \left(\frac{2}{3m^*} W - \frac{\boldsymbol{j}^2}{3n}\right) \hat{\boldsymbol{I}} + \frac{\boldsymbol{j}\boldsymbol{j}^\top}{n} \tag{2.40}$$

and

$$n \left\langle \epsilon \boldsymbol{v}\boldsymbol{v}^\top \right\rangle_{\boldsymbol{k}}^{\mathrm{CHD}} = \left(\frac{10}{9m^*}\frac{W^2}{n} - \frac{7}{9}\frac{\boldsymbol{j}^2 W}{n^2} + \frac{1}{9} m^* \frac{\boldsymbol{j}^4}{n^3}\right) \hat{\boldsymbol{I}} + \left(\frac{7}{3}\frac{W}{n} - \frac{2}{3} m^* \frac{\boldsymbol{j}^2}{n^2}\right) \frac{\boldsymbol{j}\boldsymbol{j}^\top}{n}\,, \tag{2.41}$$

resulting in

$$\frac{\partial \boldsymbol{j}}{\partial t} + \frac{e}{m^*} n \boldsymbol{E} + \boldsymbol{\nabla}\left(\frac{2}{3m^*} W - \frac{\boldsymbol{j}^2}{3n}\right) + \left(\boldsymbol{\nabla}^\top \frac{\boldsymbol{j}\boldsymbol{j}^\top}{n}\right)^\top = -\frac{\boldsymbol{j}}{\tau_\mathrm{j}} \tag{2.42}$$

and

$$\begin{aligned} \frac{\partial \boldsymbol{S}}{\partial t} + e\left(\left(\frac{5}{3m^*} W - \frac{\boldsymbol{j}^2}{3n}\right) \hat{\boldsymbol{I}} + \frac{\boldsymbol{j}\boldsymbol{j}^\top}{n}\right) \boldsymbol{E} + \boldsymbol{\nabla}\left(\frac{10}{9m^*}\frac{W^2}{n} - \frac{7}{9}\frac{\boldsymbol{j}^2 W}{n^2} + \frac{m^*}{9}\frac{\boldsymbol{j}^4}{n^3}\right) \\ + \left(\boldsymbol{\nabla}^\top \left(\frac{7}{3}\frac{W}{n} - \frac{2}{3} m^* \frac{\boldsymbol{j}^2}{n^2}\right) \frac{\boldsymbol{j}\boldsymbol{j}^\top}{n}\right)^\top = -\frac{\boldsymbol{S}}{\tau_\mathrm{S}}\,. \end{aligned} \tag{2.43}$$

The obtained model is called Convective Hydrodynamic (CHD) model.

2.4 Small-Signal Analysis

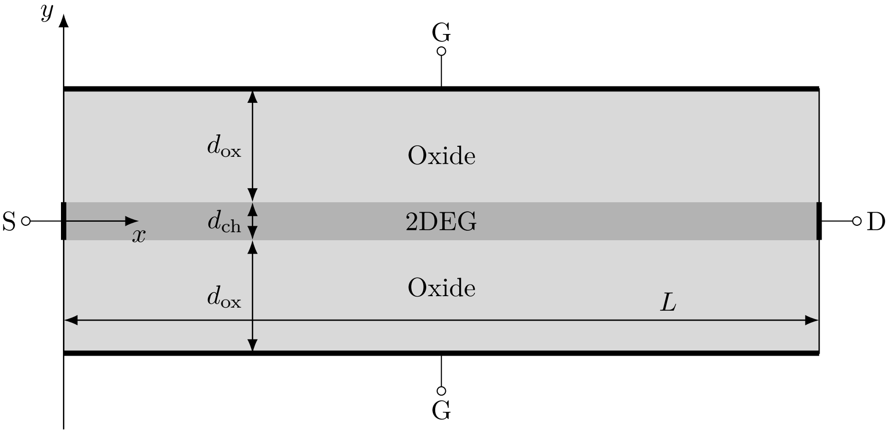

Figure 2.1: Double-gate device with a quasi 2DEG and a homogeneous channel.

To assess the accuracy of the balance equations compared to the BTE, the double-gate device from [1] with a length of $L = 60\,\text{nm}$, shown in Figure 2.1, is used. Sandwiched between two oxide regions with a thickness of $d_{\text{ox}} = 20\,\text{nm}$ and a permittivity of $\varepsilon_{\text{ox}} = 3.9\,\varepsilon_0$, the transport is confined to a quasi two-dimensional layer with $d_{\text{ch}} \ll d_{\text{ox}}$ and a constant electron sheet density of $n_0 = 2 \cdot 10^{12}/\text{cm}^2$. Since the device is assumed to be homogeneous in z-direction, this results in a one-dimensional transport model. For the BTE simulations, the material of the channel is chosen as silicon, with the scattering and band structure model from [27]. For simplicity, the non-parabolicity of the valleys is ignored and an isotropic effective mass of $m^* = 0.28621\,m_{\text{e}}$ is used. The temperature is fixed to $T_0 = 77\,\text{K}$, resulting in a very high electron mobility, which is necessary to not dampen the plasma waves too much.

Under stationary conditions, the electric field as well as all transport moments are assumed to be constant in the channel. The dynamic behavior is then described by a small-signal wave ansatz, where the total quantities are given by

$$E(x,t) = E_0 + \operatorname{Re}\big\{\underline{E}\exp\big(-\mathrm{j}\underline{q}x\big)\exp(\mathrm{j}\underline{\omega}t)\big\} \tag{2.44}$$

$$n(x,t) = n_0 + \operatorname{Re}\big\{\underline{n}\exp\big(-\mathrm{j}\underline{q}x\big)\exp(\mathrm{j}\underline{\omega}t)\big\} \tag{2.45}$$

$$j(x,t) = j_0 + \operatorname{Re}\big\{\underline{j}\exp\big(-\mathrm{j}\underline{q}x\big)\exp(\mathrm{j}\underline{\omega}t)\big\} \tag{2.46}$$

$$\vdots$$

with the wave number $\underline{q}$ and the frequency $\underline{\omega}$. Underlined quantities represent complex numbers, and all transport quantities are two-dimensional sheet quantities.

The small-signal continuity equation then reads [1]

$$\underline{n} = \frac{\underline{q}}{\underline{\omega}}\,\underline{j}\,. \tag{2.47}$$

The remaining equations of each transport model contain scattering terms, which depend on the respective macroscopic relaxation time. These times, as well as their derivative w.r.t. the electric field, are extracted from homogeneous simulations of the BTE for silicon. This involves discretizing the BTE on an energy grid, while the dependence of the distribution function on the direction of $\boldsymbol{k}$ is modeled by a Spherical Harmonics Expansion (SHE) [28, 29, 30, 31]. Thus, the BTE is expressed in terms of the quantities

$$g_{lm}(\boldsymbol{r}, \epsilon, t) = \frac{2}{(2\pi)^3} \iiint \delta(\epsilon - \epsilon(\boldsymbol{k})) Y_{lm}(\theta, \phi) f(\boldsymbol{r}, \boldsymbol{k}, t)\, \mathrm{d}^3 k\ , \tag{2.48}$$

with $l = 0, 1, \ldots, \infty$ and $m = -l, \ldots, l$. $\delta(\epsilon)$ is the Dirac delta function, and $Y_{lm}(\theta, \phi)$ denote the real-valued spherical harmonics, with θ and ϕ being the spherical coordinates of $\boldsymbol{k}$. Even though the quantities g_{lm} are also projections of the distribution function, in contrast to the moments n, j, ..., they are still energy dependent. Therefore this approach is far more accurate (and computationally expensive), since for instance physical scattering processes can be modeled directly.

The expansion is cut off at a certain order, denoted by N_l. It was found that $N_l = 3$ is sufficient, as there is no discernable difference between $N_l = 3$ and $N_l = 5$ in the homogeneous case [1]. In general, going to a higher order increases the amount of anisotropy of the distribution function that can be modeled using this approach.

The electric field used in the BTE simulation is then transformed to a corresponding effective field strength for each transport model, leading to equations of the form [1]

$$\big(\mathbf{M}_0 + \mathrm{j}\underline{\omega}\,\mathbf{P} - \mathrm{j}\underline{q}\,\mathbf{Q}\big)\,\underline{\boldsymbol{U}} + \boldsymbol{r}_\mathrm{E}\,\underline{E} + \big(\boldsymbol{r}_\mathrm{n} - \mathrm{j}\underline{q}\,\boldsymbol{s}_\mathrm{n}\big)\,\underline{n} = \mathbf{0}\,, \tag{2.49}$$

where $\underline{\boldsymbol{U}}$ contains the transport moments except for $\underline{n}$. For the DD and CDD models it is therefore given by $\underline{\boldsymbol{U}} = \big(\underline{j}\big)$, while for the HD and CHD models it is $\underline{\boldsymbol{U}} = \big(\underline{j}\ \ \underline{W}\ \ \underline{S}\big)^\top$. The specific values for $\mathbf{M}_0$, $\mathbf{P}$, $\mathbf{Q}$, $\boldsymbol{r}_\mathrm{E}$, $\boldsymbol{r}_\mathrm{n}$ and $\boldsymbol{s}_\mathrm{n}$ can be found in [1]. For a given $\underline{\omega}$ and

$\underline{q}$, eqs. (2.47) and (2.49) can then be transformed to yield the small-signal mobility [1]

$$\underline{\mu} = -\frac{e}{n_0}\frac{\underline{j}}{\underline{E}}\,. \tag{2.50}$$

2.4.1 Small-Signal Mobility

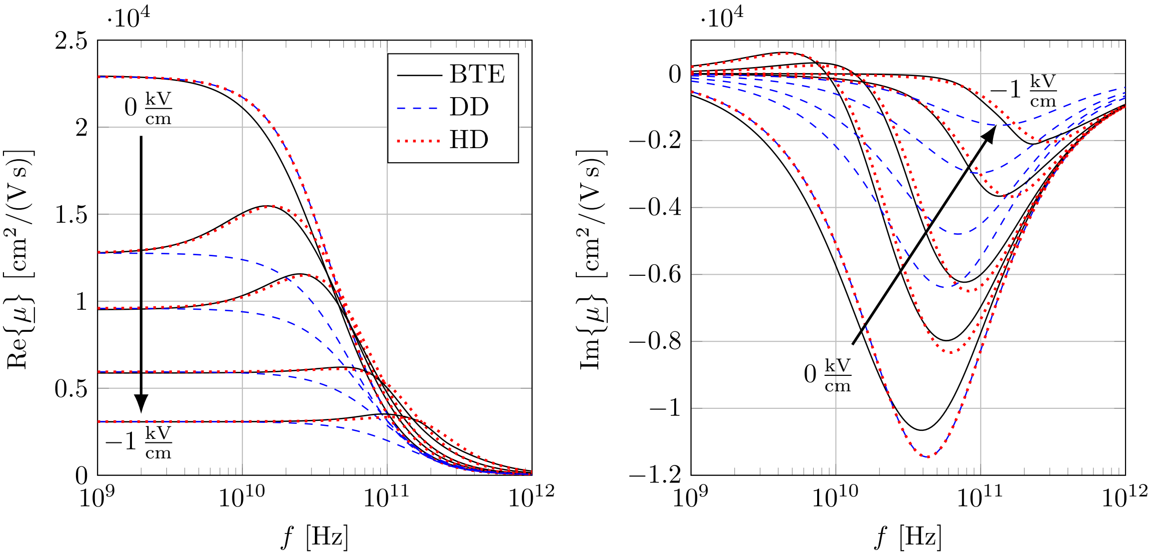

Figure 2.2: Small-signal mobility of bulk silicon at $T_0 = 77\,\mathrm{K}$ for $\underline{q} = 0$ and $E_0 = 0\,\mathrm{kV/cm}$, $-0.1\,\mathrm{kV/cm}$, $-0.2\,\mathrm{kV/cm}$, $-0.5\,\mathrm{kV/cm}$ and $-1\,\mathrm{kV/cm}$.

In Figure 2.2 the small-signal mobility depending on the frequency is compared between the DD, HD and the BTE for different electric field strengths. Since $\underline{q} = 0$ is chosen in this case, the convective derivatives present in the CDD and CHD models have no influence here and thus, these models are omitted from the plot. For small frequencies, the results are consistent with the BTE, originating from the fact, that the relaxation times are directly extracted from the BTE results. In other words, the DC mobility at $f = 0\,\mathrm{Hz}$ is fitted to the BTE result. Under equilibrium conditions ($E_0 = 0\,\mathrm{kV/cm}$) the results from the DD and HD model coincide, since the assumed shape of the distribution function is the same for both models and the drift terms vanish. Compared to the BTE, there is however a deviation for medium to high frequencies due to the approximation of the scattering term by a macroscopic relaxation time [4, 1].

For larger absolute values of the electric field (a positive drift velocity is achieved by applying a negative E_0), the results for the three models differ from one another quite significantly. In the real part of $\underline{\mu}$ an overshoot develops both for the BTE and the HD model, which is completely missing in the DD model. This overshoot stems from the difference in momentum and energy relaxation times, which can not be captured by the single relaxation time assumption in the DD model, as opposed to the HD model [24, 1]. Similarly for $\mathrm{Im}\{\underline{\mu}\}$, the HD model is also in much better agreement to the BTE, compared to the DD, which fails to capture the region of positive $\mathrm{Im}\{\underline{\mu}\}$ at low frequencies under moderately high electric fields [1].

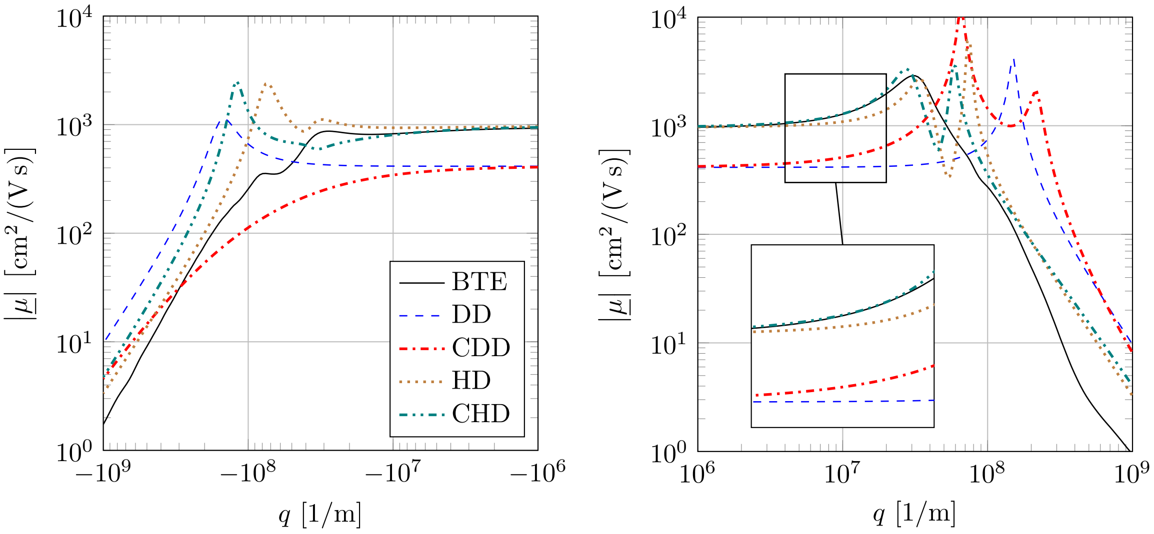

Figure 2.3: Small-signal mobility of bulk silicon at $T_0 = 77\,\mathrm{K}$ for $f = 1\,\mathrm{THz}$ and $E_0 = -1\,\mathrm{kV/cm}$.

Next, the $\underline{q}$ dependency is investigated. In Figure 2.3 the absolute value of the small-signal mobility is shown both for negative and positive real valued q at a frequency of $f = 1\,\mathrm{THz}$ and an electric field of $E_0 = -1\,\mathrm{kV/cm}$ for all models, including the CDD and CHD model. For $q \to 0/\mathrm{m}$, the DD models underestimate the mobility, as opposed to the HD models, which again is related to the single relaxation time that cannot capture the overshoot. For small values of $|q|$, both of the convective models CDD and CHD show a better agreement to the BTE, compared to the DD and HD model. Especially the CHD model is in excellent agreement with the BTE, while the CDD model at least gives a similar shape [1]. This shows, that the assumed shifted Maxwellian distribution function is a good approximation to the BTE result for small q, at least under homogeneous bulk conditions.

For larger values of q, all of the moments-based transport models fail to reproduce the

BTE results. This is to be expected, since the small-signal mobility in eq. (2.50) has only a very small number of poles in the complex $\underline{q}$-plane [1] (whose influence can be seen as peaks in Figure 2.3), compared to the large number of poles for the BTE [4, 5]. Since the position and strength of each pole completely determines the behavior of $\underline{\mu}$ in the whole complex plane, even for the CHD, the correct behavior at small q necessarily results in regions where the behavior is completely wrong; the number of degrees of freedom is simply to small. This means, that if the poles were placed differently, the behavior at large q could be improved, but only at the cost of worse behavior for smaller q. At least for very large $q \to \infty$, all of the models show the correct relation of $|\mu| \propto q^{-2}$ [1].

2.4.2 Dispersion relation

Up to this point, $\underline{\omega}$ and $\underline{q}$ were assumed to be independent. However, when the PE is solved as well, this is no longer the case and a dispersion relation between the two quantities can be found. To that end, a similar small-signal wave ansatz is made for the potential

$$\varphi(x,y,t) = \varphi_0(x,y) + \mathrm{Re}\big\{\underline{\varphi}\,\underline{\psi}(y)\exp\big(-\mathrm{j}\underline{q}x\big)\exp(\mathrm{j}\underline{\omega}t)\big\}\,, \tag{2.51}$$

where the additional y-dependency is modeled by the function $\underline{\psi}(y)$, which is normalized in the channel center to $\underline{\psi}(0) = 1$. Under the assumption of $d_{\mathrm{ch}} \ll d_{\mathrm{ox}}$, the small-signal PE then reads

$$\underline{\varphi}\left(-\underline{q}^2 + \frac{\partial^2}{\partial y^2}\right)\underline{\psi}(y) = -\frac{e}{\varepsilon_{\mathrm{ox}}}\,\delta(y)\,\underline{n}\,. \tag{2.52}$$

The solution is given by [1]

$$\underline{\psi}(y) = \frac{\sinh\big(\underline{q}\,(d_{\mathrm{ox}} - |y|)\big)}{\sinh\big(\underline{q}\,d_{\mathrm{ox}}\big)} \quad \text{and} \quad \underline{\varphi} = -e\,\frac{d_{\mathrm{ch}}}{2\varepsilon_{\mathrm{ox}}}\,\frac{\tanh\big(\underline{q}d_{\mathrm{ox}}\big)}{\underline{q}}\,\underline{n}\,, \tag{2.53}$$

resulting in the small-signal electric field in the channel

$$\underline{E} = \mathrm{j}\,\underline{q}\,\underline{\varphi} = -\mathrm{j}\,e\,\frac{d_{\mathrm{ch}}}{2\varepsilon_{\mathrm{ox}}}\,\tanh\big(\underline{q}d_{\mathrm{ox}}\big)\underline{n}\,. \tag{2.54}$$

For $\big|\underline{q}\big|d_{\mathrm{ox}} \ll 1$, the hyperbolic tangent can be approximated by its argument and a relation consistent with the gradual channel approximation is recovered

$$\begin{aligned} &\underline{\beta}(\underline{q}) = \tanh\bigl(\underline{q}\, d_{\mathrm{ox}}\bigr) \approx \underline{q}\, d_{\mathrm{ox}} \\ \Longrightarrow\ &\underline{\varphi} \approx -e\frac{d_{\mathrm{ch}}\, d_{\mathrm{ox}}}{2\varepsilon_{\mathrm{ox}}}\, \underline{n}\,. \end{aligned} \tag{2.55}$$

When eqs. (2.47) and (2.54) are inserted into the expression for the small-signal mobility (see eq. (2.50)), a nonlinear equation relating $\underline{\omega}$ and $\underline{q}$ can be found [1]:

$$1 - \mathrm{j}\,\frac{n_0}{2\,\varepsilon_{\mathrm{ox}}}\,\frac{\underline{q}}{\underline{\omega}}\,\underline{\beta}(\underline{q})\,\underline{\mu}(\underline{\omega},\underline{q}) = 0\,. \tag{2.56}$$

For a given $\underline{q}$, this can be transformed into an eigenvalue problem in $\underline{\omega}$, or, alternatively, for a given $\underline{\omega}$ and using the approximation from eq. (2.55), into an eigenvalue problem in $\underline{q}$ [1]. Both solution strategies result in multiple branches for the dispersion relation, where the number of branches corresponds to the number of moment equations. The branches with positive and negative real part are grouped such that

$$\mathrm{Re}\{\underline{q}^{+}\} > 0 \quad \text{and} \quad \mathrm{Re}\{\underline{q}^{-}\} < 0\,. \tag{2.57}$$

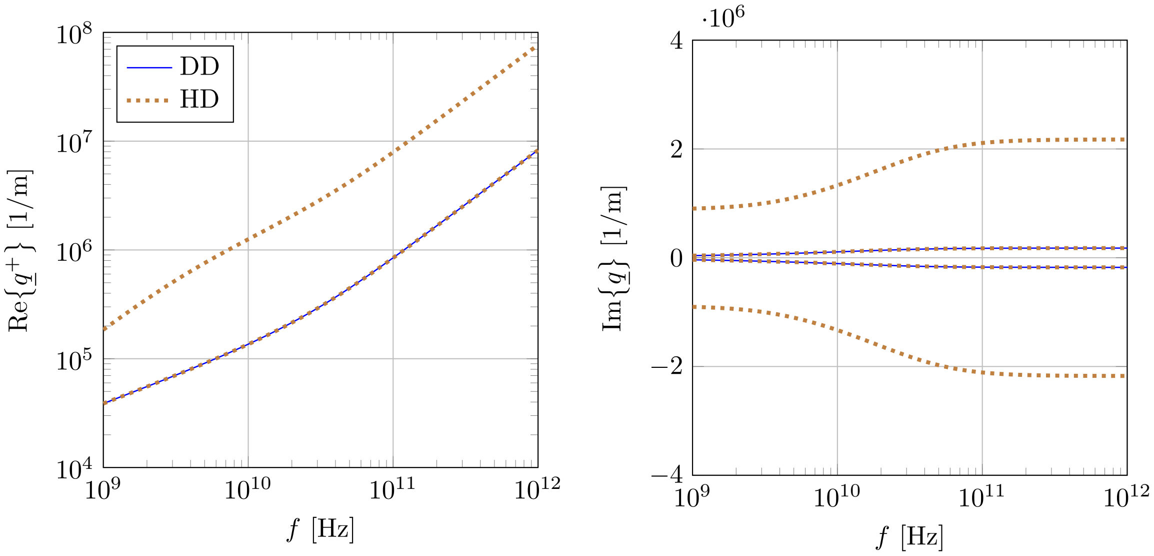

Figure 2.4: Dispersion relation for $E_0 = 0\,\mathrm{kV/cm}$.

In Figure 2.4 the positive branches of $\mathrm{Re}\{\underline{q}\}$ and all branches for $\mathrm{Im}\{\underline{q}\}$ are shown for the DD and HD model under equilibrium conditions. The CDD and CHD model are omitted again, since the convective derivatives have no influence at equilibrium. The HD model yields the same two branches as the DD model, plus an additional two modes which can be separated from the other two, due to their large imaginary parts leading to strong damping. The modes are antisymmetric ($\underline{q}^- = -\underline{q}^+$) [1].

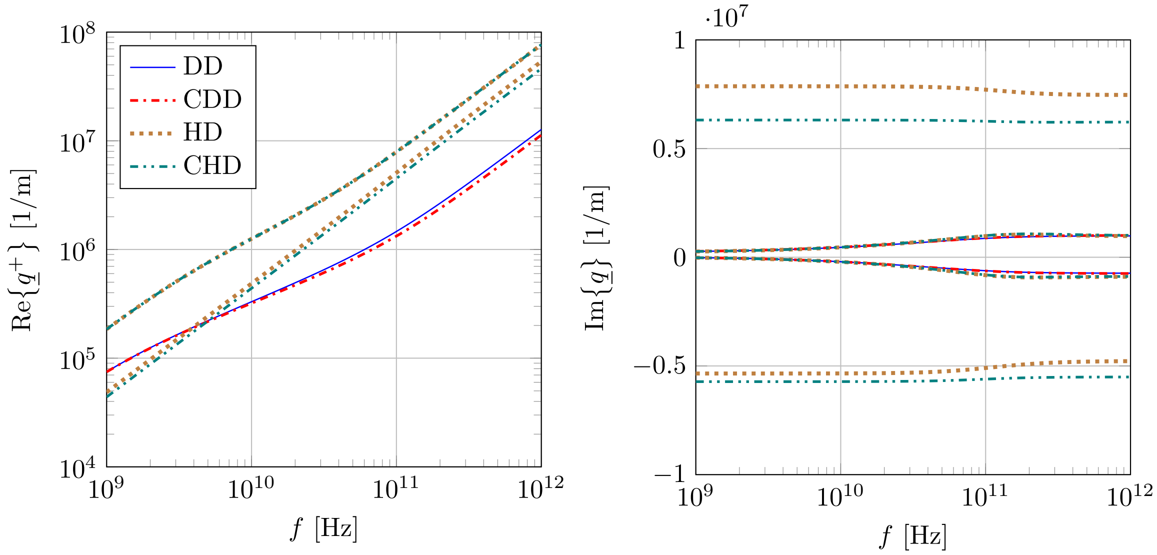

Figure 2.5: Dispersion relation for $E_0 = -1\,\mathrm{kV/cm}$.

Figure 2.5 shows the results under non-equilibrium conditions, including the convective models. For $E_0 \neq 0$, the symmetry between the positive and negative branches is broken, which can be easily seen when $\mathrm{Im}\{\underline{q}^+\}$ and $\mathrm{Im}\{\underline{q}^-\}$ are compared. Even though under these conditions the results from the HD models differ quite substantially from the DD models, it is still possible to select the two modes with a comparatively low amount of damping, as opposed to the highly damped modes, due to their large separation considering $\mathrm{Im}\{\underline{q}\}$.

2.4.3 Dyakonov-Shur Instability

In their influential paper [13], Dyakonov and Shur proposed a new mechanism for the generation of THz-waves, by using the electron plasma oscillations in a ballistic Field Effect Transistor (FET) with a 2DEG. They suggested using the one-dimensional Euler equation [13]

$$\frac{\partial v_\mathrm{d}}{\partial t} + v_\mathrm{d}\frac{\partial v_\mathrm{d}}{\partial x} = -\frac{e}{m^*}E\,, \tag{2.58}$$

to model the electron transport, where v_d is the drift velocity. This equation is actually equivalent to the one-dimensional CDD model, under the assumption of no scattering ($\tau_\mathrm{j} \to \infty$) and a homogeneous density in the channel ($\frac{\partial}{\partial x} n = 0$). Together with the gradual channel approximation for the solution of the PE, an analogy to the shallow water equations [32] can be found, which for asymmetric boundary conditions leads to the prediction of an instability for electron plasma waves. By applying the same procedure to the transport models used in this work, as well as the BTE, they can be evaluated in regards to their applicability to describe THz-wave generation.

The asymmetric boundary conditions used by Dyakonov and Shur consist of fixing the density at the source terminal to a constant value, while on the drain terminal the current is fixed instead. In the small-signal regime this means that the corresponding small-signal quantities should vanish at those points

$$\underline{n}(0) = 0 \quad \text{and} \quad \underline{j}(L) = 0\,, \tag{2.59}$$

where L is the device length (see Figure 2.1). To fulfill both of these boundary conditions, a superposition of two waves with the same frequency is assumed, which, in the case of the two drift-diffusion models, are the two $\underline{q}(\underline{\omega})$ branches with positive and negative real part. For hydrodynamic models, out of the four modes, the two with the least amount of damping are chosen, which are separated from the other ones [1]. For the BTE, the two Vlasov modes are chosen [5].

The small-signal density and current density are then given by

$$\underline{n}(x) = \underline{n}^+ \exp\bigl(-\mathrm{j}\underline{q}^+ x\bigr) + \underline{n}^- \exp\bigl(-\mathrm{j}\underline{q}^- x\bigr) \tag{2.60}$$

$$\begin{aligned} \underline{j}(x) &= \underline{j}^+ \exp\bigl(-\mathrm{j}\underline{q}^+ x\bigr) + \underline{j}^- \exp\bigl(-\mathrm{j}\underline{q}^- x\bigr) \\ &= \frac{\omega}{\underline{q}^+}\underline{n}^+ \exp\bigl(-\mathrm{j}\underline{q}^+ x\bigr) + \frac{\omega}{\underline{q}^-}\underline{n}^- \exp\bigl(-\mathrm{j}\underline{q}^- x\bigr)\,, \end{aligned} \tag{2.61}$$

where $\underline{n}^+$ and $\underline{n}^-$ are constant coefficients. Inserting the source boundary condition yields

$$\underline{n}(0) = \underline{n}^+ + \underline{n}^- \overset{!}{=} 0 \implies \underline{n}^- = -\underline{n}^+\,, \tag{2.62}$$

which together with the drain boundary condition finally gives a nonlinear equation for

$\underline{\omega}$ [1]

$$\frac{\underline{q}^{+}(\underline{\omega})}{\underline{q}^{-}(\underline{\omega})}\exp\bigl(\mathrm{j}\bigl(\underline{q}^{+}(\underline{\omega})-\underline{q}^{-}(\underline{\omega})\bigr)L\bigr)-1=0\,. \tag{2.63}$$

This equation is then solved by a Newton iteration, and the frequency $f=\frac{\mathrm{Re}\{\underline{\omega}\}}{2\pi}$ and growth-factor $\sigma=-\mathrm{Im}\{\underline{\omega}\}$ are extracted from the solution. When $\sigma>0$, the system is unstable, leading to an exponential growth of the plasma modes. This results in the emittance of waves in the THz-range.

The original model by Dyakonov and Shur gives [13]

$$\underline{\omega}^{\mathrm{DS}}=\frac{s^2-v_0^2}{2\,L\,s}\,\pi+\mathrm{j}\,\frac{s^2-v_0^2}{2\,L\,s}\,\log\left(\frac{s+v_0}{s-v_0}\right) \tag{2.64}$$

for the plasma velocity $s=\sqrt{\frac{n_0}{Cm^*}}$ and the DC drift velocity v_0, under the assumption of $s>v_0$. The gate capacitance for a double-gate device is approximated by $C=\frac{2\,\varepsilon_{\mathrm{ox}}}{d_{\mathrm{ox}}}$.

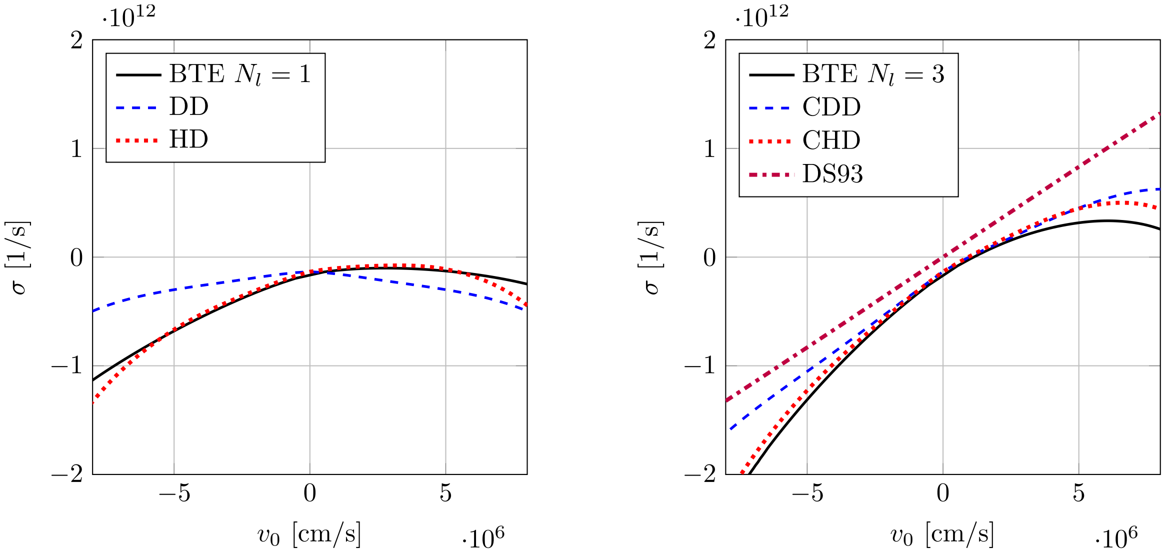

Figure 2.6: Growth factor for the Dyakonov-Shur instability.

In Figure 2.6 the growth-factor depending on the DC drift velocity is shown for the different models. To avoid clutter, the models are split into two different groups with similar characteristics. In the first group, the DD and HD model without convective derivatives are shown, together with the results of a first-order SHE of the BTE. For all three models, the growth-factor stays negative, and the HD model shows excellent agreement to the BTE.

The second group consists of the CDD and CHD model, as well as a third-order SHE of the BTE and the original model by Dyakonov and Shur from [13]. In contrast to the other group of models, here the growth-factor actually becomes positive. As opposed to the first-order SHE, the third-order SHE takes the anisotropy of the distribution function into account, which makes it more accurate. Both the DD and HD model are derived under the assumption of an isotropic distribution function, which explains the similarity to the first-order SHE [1]. All of the models in the second group have a similar slope, which is consistent with the original model by Dyakonov and Shur. However, the original model neglects scattering, which is why the growth-factor is consistently overestimated.

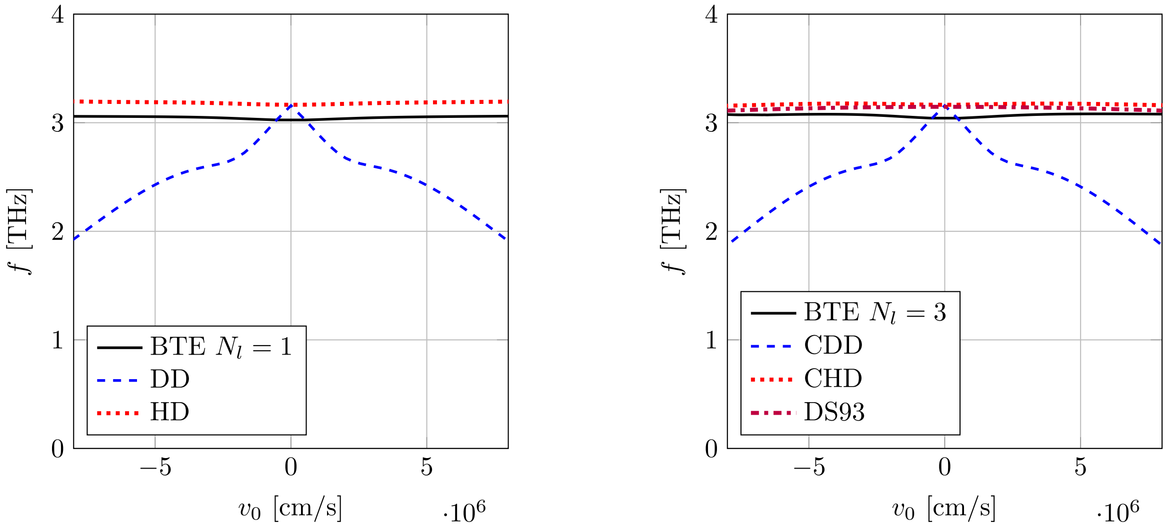

Figure 2.7: Frequency of the Dyakonov-Shur instability.

For small drift velocities, all models give a similar result for the frequency of about $f = 3\,\text{THz}$. For larger electric fields (and therefore larger v_0), a huge discrepancy between the DD and CDD on the one hand, and all other models on the other hand arises. Overall, the best agreement to the BTE results is given by the CHD model [1].

2.4.4 Impact of the Boundary Conditions

Even though the approach by Dyakonov and Shur can provide a good tool for comparing the accuracy of the moments-based transport models to the BTE, its ability to predict actual plasma wave instabilities seems to be at least questionable. In [7] transport through a silicon nanowire transistor was investigated under quasi-ballistic transport conditions using very large electron mobilities, which are also required for the Dyakonov-Shur instability. The BTE was compared to the DD model, as well as a transport model based on Ten Moments (TM). For the BTE, Thermal Bath (TB) boundary conditions were used, where electrons in the contacts follow a Maxwellian distribution. This distribution is then imposed at each contact as a boundary condition only on the inflowing particles, not on the outflowing ones. For the other models both Dirichlet and TB boundary conditions were considered. In the latter case, the TB conditions are included by projection onto the moments.

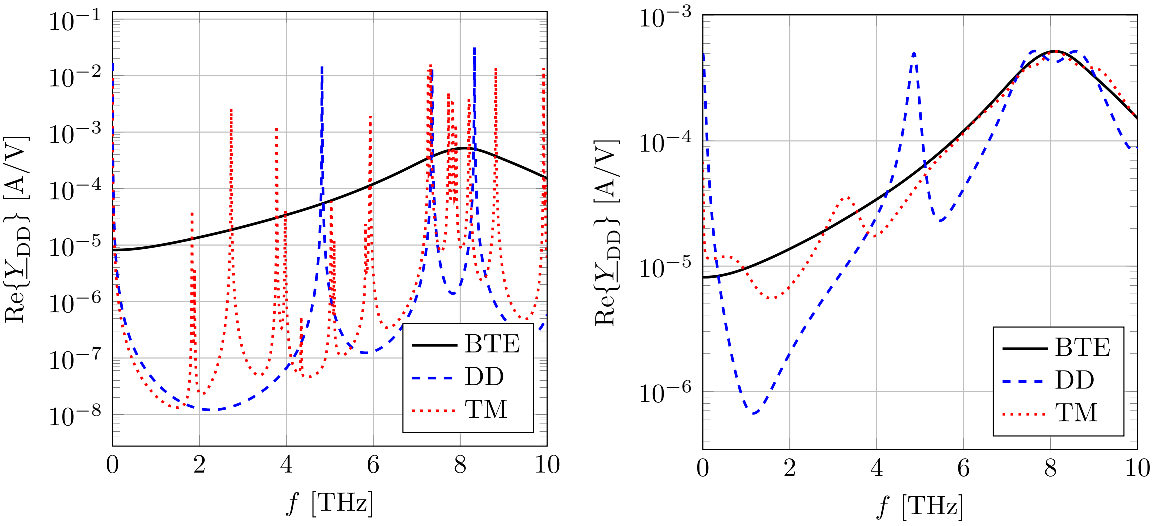

(a) Dirichlet boundary conditions.

(b) Thermal bath boundary conditions.

Figure 2.8: Influence of boundary conditions on plasma resonances.

In Figure 2.8 the resulting small-signal drain self-admittance is shown for both types of boundary conditions. For Dirichlet conditions, which correspond to the kind of boundaries used by Dyakonov and Shur, the DD model shows some very sharp peaks, corresponding to electron plasma resonances. Increasing the number of moments leads to more of these resonances (see results of the TM model). As opposed to that, the BTE, which uses the more realistic TB boundary conditions, does not show any sharp resonances. When TB conditions are applied to the DD and TM model as well, the results are more consistent with the BTE, however there are still large deviations. Especially for low frequencies the moments-based transport models give a far too large value for $\mathrm{Re}\{\underline{Y}_{\mathrm{DD}}\}$ [33, 34, 7].

In conclusion, the moments-based transport models fail in the near-ballistic transport regime, and the situation gets worse for Dirichlet boundary conditions [7]. The plasma instability predicted by Dyakonov and Shur can therefore be interpreted as simply an artifact of the transport model in combination with unrealistic boundary conditions. Nevertheless, the passive detection of THz waves (in contrast to their generation) using electron plasma oscillations is still a possibility. In the diffusive regime even the DD model can give somewhat accurate results [7], and in the remainder of this work, numerical algorithms for the simulation of both one and two dimensional devices using moments-based transport models are developed.

3 One-Dimensional Device Simulation

In this chapter, the focus is on one dimensional devices only, i.e. devices that can be approximated to be homogeneous in all but one direction. The goal is to develop a stable numerical scheme for solving the relevant equations, i.e. the PE coupled to a transport model. Due to simplicity reasons, only the DD and CDD models are considered, serving as a proof of concept. Because of their hyperbolic nature, typically used stabilization strategies do not work anymore, and the scheme needs to be newly developed from the ground up. Using many similar concepts, a low-order and a high-order scheme is created, and stationary as well as small-signal results are presented for a simple one-dimensional device.

3.1 Grid

To solve a system of coupled PDEs numerically, the device under consideration needs to be discretized. For that purpose, a grid is introduced, i.e. a device of length L is split into a finite number of intervals with a finite length each. The interval length can be the same for all intervals (equidistant grid), however that is not necessarily the case.

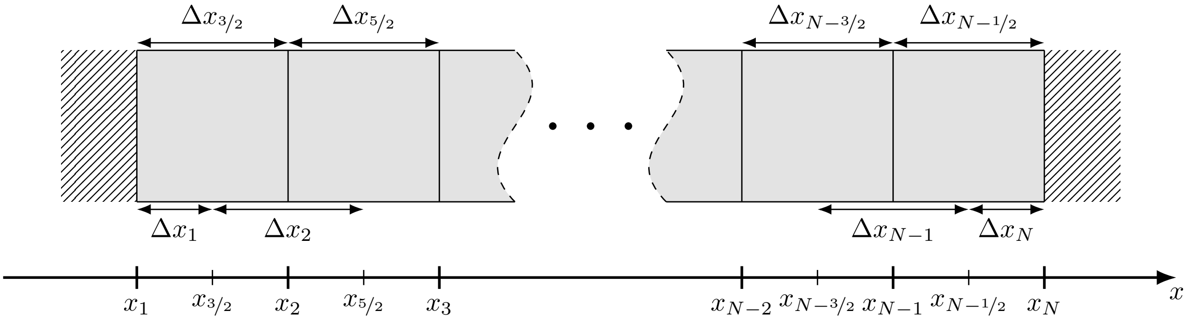

Figure 3.1: Exemplified 1D device where the hatched patterns indicate contacts.

By introducing N grid nodes, denoted by x_i where $1 \leq i \leq N$, the device is split into $N-1$ intervals, which will be called cells here. These cells are then numbered by half-integers (see Figure 3.1), where the cell centers are given by

$$x_{i+1/2} = \frac{1}{2}(x_i + x_{i+1})\,, \tag{3.1}$$

and the corresponding cell extents are

$$\Delta x_{i+1/2} = x_{i+1} - x_i\,. \tag{3.2}$$

In addition to this, adjoint cells, numbered by whole integers, can be defined by using the values $x_{i+1/2}$ as interval end points. For non-boundary cells, the adjoint cell size is

$$\Delta x_i = x_{i+1/2} - x_{i-1/2} = \frac{1}{2}(x_{i+1} - x_{i-1})\,, \tag{3.3}$$

while at the boundaries

$$\Delta x_1 = x_{3/2} - x_1 \quad \text{and} \quad \Delta x_N = x_N - x_{N-1/2}\,. \tag{3.4}$$

All spatially varying material constants, such as the electrostatic permittivity $\varepsilon(x)$ or doping concentrations, are approximated as piecewise constant on the direct grid cells, e.g.

$$\varepsilon(x) = \varepsilon_{i+1/2} \quad \text{for} \quad x \in (x_i, x_{i+1})\,. \tag{3.5}$$

At both ends of the device (at x_1 and x_N), metal-semiconductor contacts are attached, which require special boundary conditions, when solving the device equations.

3.2 Poisson Equation

There are many different methods for discretizing and solving the PE numerically. Most of these methods can be grouped into one of the three categories: Finite-Difference, Finite-Volume and Finite-Elements. Finite-Volume Methods (FVMs) have the advantage, that the conservation of the electric flux can be achieved with relative ease, as opposed to methods from the other two categories. In the context of semiconductor device simulation, usually the Vertex-Centered Finite-Volume Method (VCFVM) is used [35, 36] (often referred to as the "Box-Integration Method"), which is discussed in the next section. In addition to that, in this work a high-order Cell-Centered Finite-Volume Method (CCFVM) is developed, which has a better resolution and can be coupled more easily to the transport model, especially in two dimensions. Coupling to the transport model is achieved by providing an expression for the electric field.

In one dimension the PE reads

$$\frac{\partial}{\partial x} D(x) = \varrho(x)\,, \tag{3.6}$$

where for the sake of brevity the dependence on the time t was dropped. The electric flux density in one dimension is a scalar

$$D(x) = -\varepsilon \frac{\partial \varphi(x)}{\partial x}\,, \tag{3.7}$$

and similarly the electric field is given by

$$E(x) = \frac{D(x)}{\varepsilon} = -\frac{\partial \varphi(x)}{\partial x}\,. \tag{3.8}$$

3.2.1 Vertex-Centered Finite Volume Method

For the VCFVM, the adjoint cells are used as finite volumes (see Figure 3.2). Integrating eq. (3.6) over the interval from $x_{i-1/2}$ to $x_{i+1/2}$ where $i \neq 1, N$ results in

$$\begin{aligned} &\int_{x_{i-1/2}}^{x_{i+1/2}} \frac{\partial}{\partial x} D(x)\,\mathrm{d}x = \int_{x_{i-1/2}}^{x_{i+1/2}} \varrho(x)\,\mathrm{d}x \\ \implies\ & D_{i+1/2} - D_{i-1/2} = \Delta x_i \overline{\varrho}_i \end{aligned} \tag{3.9}$$

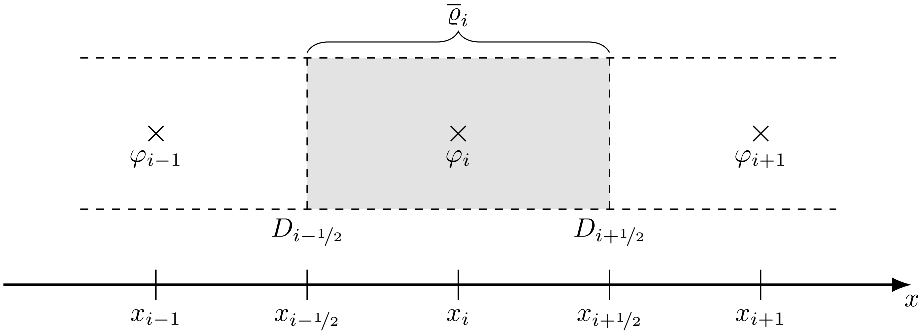

Figure 3.2: Vertex-Centered Finite Volume Method using the adjoint cells as finite volumes.

where $D_{i\pm 1/2} = D\big(x_{i\pm 1/2}\big)$ are the electric fluxes on the adjoint cell boundaries and $\overline{\varrho}_i$ is the average charge density in the interval

$$\overline{\varrho}_i = \frac{1}{\Delta x_i} \int_{x_{i-1/2}}^{x_{i+1/2}} \varrho(x)\, \mathrm{d}x \ . \tag{3.10}$$

Introducing the discrete electrostatic potential $\varphi_i = \varphi(x_i)$ defined at each vertex, the fluxes can be approximated by

$$D_{i+1/2} \approx \frac{\varepsilon_{i+1/2}}{\Delta x_{i+1/2}}(\varphi_i - \varphi_{i+1}) = C_{i+1/2}(\varphi_i - \varphi_{i+1})\,, \tag{3.11}$$

with the capacitance coefficients $C_{i+1/2}$. Since the same expression is used at either side of the cell interface, flux conservation is automatically achieved, i.e. $\operatorname{Div} D\big|_{x_{i+1/2}} = 0$. Inserting eq. (3.11) into eq. (3.9) leads to

$$-C_{i-1/2}\varphi_{i-1} + \big(C_{i-1/2} + C_{i+1/2}\big)\varphi_i - C_{i+1/2}\varphi_{i+1} = \Delta x_i \overline{\varrho}_i\,. \tag{3.12}$$

For the contacted boundary points ($i = 1$ and $i = N$), Dirichlet conditions are applied by setting the potential at these points directly to its boundary value

$$\varphi_1 = V_\mathrm{S} + \phi_\mathrm{MS,S} \quad \text{and} \quad \varphi_N = V_\mathrm{D} + \phi_\mathrm{MS,D}\,, \tag{3.13}$$

where V_S and V_D are the external source and drain contact potential which are shifted by the work function differences at both contacts $\phi_\mathrm{MS,S}$ and $\phi_\mathrm{MS,D}$, respectively. For ideal ohmic contacts and assuming a homogeneous material, the work function differences are given by

$$\phi_{\mathrm{MS}} = V_{\mathrm{T}} \operatorname{asinh}\left(\frac{N_{\mathrm{D}} - N_{\mathrm{A}}}{2n_{\mathrm{i}}}\right) \tag{3.14}$$

when electrons and holes are considered, or

$$\phi_{\mathrm{MS}} = V_{\mathrm{T}} \log\left(\frac{N_{\mathrm{D}}}{n_{\mathrm{i}}}\right) \tag{3.15}$$

when holes are neglected.

Writing φ_i and $\overline{\varrho}_i$ as column vectors, where i denotes the i-th component, eqs. (3.12) and (3.13) can be combined in matrix-vector form yielding

$$\mathbf{C}\boldsymbol{\varphi} = \mathbf{R}\boldsymbol{\varrho} + \boldsymbol{b}_{\mathrm{V}}\,, \tag{3.16}$$

where $\mathbf{C}$ contains the capacitance coefficients, $\mathbf{R}$ is a diagonal matrix containing the cell sizes Δx_i and $\boldsymbol{b}_{\mathrm{V}}$ is a vector containing the right-hand sides of eq. (3.13). Assuming the charge densities $\overline{\varrho}_i$ and the external contact potentials $V_{\mathrm{S,D}}$ are given, the discrete potentials φ_i can then be calculated by solving eq. (3.16). In addition to that, at the adjoint points the electric field can be calculated using the expression

$$E_{i+1/2} = \frac{D_{i+1/2}}{\varepsilon_{i+1/2}} \approx \frac{\varphi_i - \varphi_{i+1}}{\Delta x_{i+1/2}}\,. \tag{3.17}$$

While the VCFVM has the advantage of being quite simple, in general it is only first-order accurate (second-order for equidistant grids). Moreover, eq. (3.17) is only accurate at the adjoint points, which can lead to problems depending on how the transport model is discretized.

3.2.2 Cell-Centered Finite Volume Method

As an alternative to the VCFVM, the CCFVM uses the direct grid cells as finite volumes. Like before, integration over a volume results in a relation between the fluxes at the cell boundaries and the average charge density contained in the cell

$$\begin{aligned} \int_{x_i}^{x_{i+1}} \frac{\partial}{\partial x} D(x)\,\mathrm{d}x &= \int_{x_i}^{x_{i+1}} \varrho(x)\,\mathrm{d}x \\ \implies D_{i+1} - D_i &= \Delta x_{i+1/2}\overline{\varrho}_{i+1/2}\,, \end{aligned} \tag{3.18}$$

with $D_i = D(x_i)$ and $\overline{\varrho}_{i+1/2} = \frac{1}{\Delta x_{i+1/2}} \int_{x_i}^{x_{i+1}} \varrho(x)\,\mathrm{d}x$. Similar to the VCFVM, the flux can now be expressed in terms of the potential, e.g. by connecting the relevant capacitances in series

$$D_i \approx 2\frac{C_{i-1/2}C_{i+1/2}}{C_{i-1/2}+C_{i+1/2}}\left(\varphi_{i-1/2}-\varphi_{i+1/2}\right). \tag{3.19}$$

This results in a method which is very similar to the VCFVM in terms of accuracy. However, in order to achieve a high-order method, where the electric field can be evaluated everywhere in the cell, this approximation will not be used here. Instead, the electric fluxes themselves will be used as discrete solution variables, as well as the cell averages of the potential rather than its value in each cell center. Thus, there is one discrete solution variable per cell (potential) and additionally one per vertex (flux), implying that there also needs to be one discrete equation per cell and one per vertex. The cell equation is already given by eq. (3.18), while for the vertex equation at first an expression for

$$\varphi_{i+1/2}(x) = \varphi(x) \quad \text{for} \quad x \in (x_i, x_{i+1}) \tag{3.20}$$

in each cell is found. Subsequently, the continuity of $\varphi(x)$ at the vertices is enforced, i.e. the left- and right-hand limits at each vertex must coincide

$$\varphi_{i-1/2}(x_i) \overset{!}{=} \varphi_{i+1/2}(x_i), \tag{3.21}$$

which is the desired vertex equation. For the first and last vertex, this equation is replaced by the corresponding Dirichlet boundary condition

$$\varphi_{3/2}(x_1) = V_\mathrm{S} + \phi_\mathrm{MS,S} \quad \text{and} \quad \varphi_{N-1/2}(x_N) = V_\mathrm{D} + \phi_\mathrm{MS,D}. \tag{3.22}$$

In the following, for the sake of brevity the cell indices are dropped. The notation shown in Figure 3.3 is used, and the origin is shifted to the cell center.

The general idea for finding an expression for $\varphi(x)$ is to solve the PE exactly in each cell. To that end, some information about the distribution of charges in the cell is required, i.e. $\varrho(x)$ must be known instead of just $\overline{\varrho}$. It is therefore assumed that the charge density at the Gauss-Legendre quadrature nodes and at the cell boundaries is known

$$\varrho\left(\frac{\Delta x}{2}\xi_k\right) = \varrho_k, \tag{3.23}$$

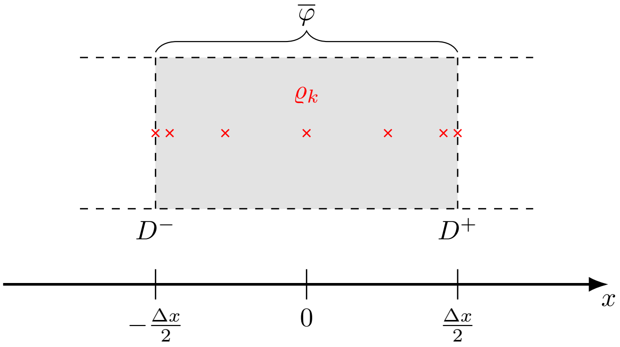

Figure 3.3: Cell-Centered Finite Volume Method using the direct cells as finite volumes. The red markers indicate the position of the $N_\mathrm{G} = 5$ Gauss-Legendre nodes as well as the boundary values ϱ_0 and $\varrho_{N_\mathrm{G}+1}$.

with $k \in \{0, 1, \ldots, N_\mathrm{G}, N_\mathrm{G} + 1\}$, where N_G is the number of utilized Gauss-Legendre nodes. The Gauss-Legendre quadrature rule then gives an approximation for the cell-average charge density

$$\overline{\varrho} \approx \frac{1}{2} \sum_{k=0}^{N_\mathrm{G}+1} w_k \varrho_k = \frac{1}{2} \sum_{k=1}^{N_\mathrm{G}} w_k \varrho_k \,. \tag{3.24}$$

The values for ξ_k as well as the corresponding integration weights w_k depending on N_G are given in Table 3.1 [37]. In addition to the values given in the table, the values for the additional nodes at the cell boundaries are

$$\xi_0 = -1\,, \quad \xi_{N_\mathrm{G}+1} = 1 \quad \text{and} \quad w_0 = w_{N_\mathrm{G}+1} = 0\,. \tag{3.25}$$

To get an expression for $\varrho(x)$, the interpolation polynomial through the values ϱ_k is constructed. In the Newton basis it is then given by

$$\varrho(x) = \sum_{r=0}^{N_\mathrm{G}+1} \sum_{s=0}^{N_\mathrm{G}+1} a_{rs} \prod_{t=0}^{r-1} (x - x_t) \varrho_s \,, \tag{3.26}$$

where the values a_{rs} are the newton interpolation coefficients which are calculated by the method of divided differences. Because the Gauss-Legendre nodes are more densely distributed at the interval endpoints than in the middle, Runge's phenomenon [38] is avoided. The interpolation polynomial has a degree of $N_\mathrm{G} + 1$, while polynomials up to a degree of $2N_\mathrm{G} - 1$ are integrated exactly by the quadrature formula. This demands that $N_\mathrm{G} \geq 2$, otherwise the polynomial would not be consistent with the cell average.

N_{G}	Order	ξ_k	w_k
1	1	0	2
2	3	$\pm\frac{1}{\sqrt{3}}$	1
3	5	$\pm\sqrt{\frac{3}{5}}$ 0	$\frac{5}{9}$ $\frac{8}{9}$
4	7	$\pm\sqrt{\frac{3}{7}-\frac{2}{7}\sqrt{\frac{6}{5}}}$ $\pm\sqrt{\frac{3}{7}+\frac{2}{7}\sqrt{\frac{6}{5}}}$	$\frac{1}{2}+\frac{1}{6}\sqrt{\frac{5}{6}}$ $\frac{1}{2}-\frac{1}{6}\sqrt{\frac{5}{6}}$
5	9	$\pm\frac{1}{3}\sqrt{5-2\sqrt{\frac{10}{7}}}$ $\pm\frac{1}{3}\sqrt{5+2\sqrt{\frac{10}{7}}}$ 0	$\frac{322+13\sqrt{70}}{900}$ $\frac{322-13\sqrt{70}}{900}$ $\frac{128}{255}$

Table 3.1: Gauss-Legendre nodes and weights for different values of N_{G}. Polynomials with a degree up to the given order are integrated exactly.

Assuming the charge density to be given by eq. (3.26), in the following the PE is solved exactly, resulting in an expression for $\varphi(x)$ in terms of the $\varrho_k \in \{\varrho_0, \dots, \varrho_{N_{\mathrm{G}}+1}\}$, D^+, D^- and $\overline{\varphi}$, which is the cell average of the potential

$$\overline{\varphi} = \frac{1}{\Delta x} \int_{-\Delta x/2}^{\Delta x/2} \varphi(x) \, \mathrm{d}x \; . \tag{3.27}$$

Since the permittivity ε in the cell is constant, the PE can be written as

$$\frac{\mathrm{d}^2}{\mathrm{d}x^2} \varphi(x) = -\frac{\varrho(x)}{\varepsilon} \, , \tag{3.28}$$

where the fluxes D^- and D^+ imply inhomogeneous Neumann boundary conditions:

$$\begin{aligned} \frac{\mathrm{d}}{\mathrm{d}x}\varphi(x)\bigg|_{-\Delta x/2} &= -\frac{D^-}{\varepsilon} \\ \frac{\mathrm{d}}{\mathrm{d}x}\varphi(x)\bigg|_{+\Delta x/2} &= -\frac{D^+}{\varepsilon} \, . \end{aligned} \tag{3.29}$$

This problem in connection with eq. (3.27) is well-posed, as long as eq. (3.18) is fulfilled. The solution strategy is to split the charge density into an average and a fluctuation

$$\varrho(x) = \overline{\varrho} + \widetilde{\varrho}(x)\,, \tag{3.30}$$

where

$$\begin{aligned}\widetilde{\varrho}(x) &= \sum_{r=0}^{N_\mathrm{G}+1} \sum_{s=0}^{N_\mathrm{G}+1} a_{rs} \prod_{t=0}^{r-1} (x - x_t)(\varrho_s - \overline{\varrho}) \\ &= \sum_{r=0}^{N_\mathrm{G}+1} \sum_{s=0}^{N_\mathrm{G}+1} a_{rs} \prod_{t=0}^{r-1} (x - x_t) \sum_{u=0}^{N_\mathrm{G}+1} \Big(\delta_{us} - \frac{w_u}{2}\Big) \varrho_u\,. \end{aligned} \tag{3.31}$$

Because of the linearity of the PE, it is useful to split the potential in a similar manner

$$\varphi(x) = \varphi^\mathrm{a}(x) + \widetilde{\varphi}(x)\,, \tag{3.32}$$

where $\varphi^\mathrm{a}(x)$ should not be confused with $\overline{\varphi}$ (which is constant). In fact, it is the solution to the modified problem

$$\frac{\mathrm{d}^2}{\mathrm{d}x^2}\varphi^\mathrm{a}(x) = -\frac{\overline{\varrho}}{\varepsilon}\,, \tag{3.33}$$

which should also fulfill eq. (3.27) and the boundary conditions from eq. (3.29). The solution is given by the second degree polynomial

$$\varphi^\mathrm{a}(x) = \overline{\varphi} + \frac{1}{\varepsilon}\bigg(\frac{\Delta x}{24} - \frac{x}{2}\Big(1 + \frac{x}{\Delta x}\Big)\bigg) D^+ + \frac{1}{\varepsilon}\bigg(-\frac{\Delta x}{24} - \frac{x}{2}\Big(1 - \frac{x}{\Delta x}\Big)\bigg) D^-\,. \tag{3.34}$$

Note that even though this result does not depend on $\overline{\varrho}$, it is still consistent with the right-hand side of eq. (3.33), as long as eq. (3.18) is satisfied.

The potential fluctuation can then be calculated by solving the PE with the charge fluctuation on the right-hand side

$$\frac{\mathrm{d}^2}{\mathrm{d}x^2}\widetilde{\varphi}(x) = -\frac{\widetilde{\varrho}(x)}{\varepsilon} \tag{3.35}$$

together with homogeneous Neumann boundary conditions, where

$$\frac{1}{\Delta x}\int_{-\Delta x/2}^{\Delta x/2} \widetilde{\varphi}(x)\,\mathrm{d}x = 0 \quad \text{and} \quad \frac{1}{\Delta x}\int_{-\Delta x/2}^{\Delta x/2} \widetilde{\varrho}(x)\,\mathrm{d}x = 0\,. \tag{3.36}$$

This Neumann boundary problem is also well-posed, resulting in

$$\widetilde{\varphi}(x) = -\sum_{r=0}^{N_\mathrm{G}+1}\sum_{s=0}^{N_\mathrm{G}+1}\frac{a_{rs}}{\varepsilon}\int_{-\Delta x/2}^{x}\int_{-\Delta x/2}^{x'}\prod_{t=0}^{r-1}(x''-x_t)\,\mathrm{d}x''\,\mathrm{d}x'\sum_{k=0}^{N_\mathrm{G}+1}\Big(\delta_{ks}-\frac{w_k}{2}\Big)\varrho_k+\widetilde{\varphi}_0\,, \tag{3.37}$$

with

$$\widetilde{\varphi}_0 = \sum_{r=0}^{N_\mathrm{G}+1}\sum_{s=0}^{N_\mathrm{G}+1}\frac{a_{rs}}{\varepsilon\Delta x}\int_{-\Delta x/2}^{\Delta x/2}\int_{-\Delta x/2}^{x}\int_{-\Delta x/2}^{x'}\prod_{t=0}^{r-1}(x''-x_t)\,\mathrm{d}x''\,\mathrm{d}x'\,\mathrm{d}x\sum_{k=0}^{N_\mathrm{G}+1}\Big(\delta_{ks}-\frac{w_k}{2}\Big)\varrho_k\,. \tag{3.38}$$

By converting the product to the monomial basis

$$\begin{aligned}\prod_{t=0}^{r-1}(x-x_s) &= x^r-\sum_{t=0}^{r-1}x_t x^{r-1}+\sum_{t=0}^{r-2}\sum_{u=t+1}^{r-1}x_t x_u x^{r-2}-\sum_{t=0}^{r-3}\sum_{u=t+1}^{r-2}\sum_{v=u+1}^{r-1}x_t x_u x_v x^{r-3}+\dots\\ &=\sum_{n=0}^{r}b_{rn}x^n\,,\end{aligned} \tag{3.39}$$

the integrals can be solved, finally giving

$$\widetilde{\varphi}(x) = \sum_{s=0}^{N_\mathrm{G}+1}d_s(x)(\varrho_s-\overline{\varrho})\,, \tag{3.40}$$

where

$$d_s(x) = \sum_{r=0}^{N_\mathrm{G}+1}\frac{a_{rs}}{\varepsilon}c_r(x) \tag{3.41}$$

and

$$\begin{aligned}c_r(x) = \sum_{n=0}^{r}\frac{b_{rn}}{(n+1)(n+2)}\Bigg(&\frac{\Delta x^{n+2}(1+(2n(n+4)+7)(-1)^n)}{2^{n+3}(n+3)}\\ &+\frac{(-\Delta x)^{n+1}(\Delta x(n+1)+2(n+2)x)}{2^{n+2}}-x^{n+2}\Bigg)\,.\end{aligned} \tag{3.42}$$

Alternatively, the potential fluctuation can be expressed solely in terms of the ϱ_s

$$\widetilde{\varphi}(x) = \sum_{s=0}^{N_\mathrm{G}+1}\widetilde{d}_s(x)\varrho_s\,, \tag{3.43}$$

with

$$\widetilde{d}_s(x) = \sum_{u=0}^{N_\mathrm{G}+1} d_u(x)\Big(\delta_{us} - \frac{w_s}{2}\Big)\,. \tag{3.44}$$

Inserting eqs. (3.34) and (3.43) into eq. (3.32), the potential can now be evaluated with high accuracy at every point inside of the cell, as well as on its boundaries. Writing eqs. (3.18) and (3.21) in matrix form results in an equation system

$$\begin{pmatrix} \mathbf{0} & \mathbf{C}_\mathrm{cl} \\ \mathbf{C}_{\mathrm{vt},\varphi} & \mathbf{C}_{\mathrm{vt},D} \end{pmatrix} \cdot \begin{pmatrix} \boldsymbol{\varphi} \\ \boldsymbol{D} \end{pmatrix} = \begin{pmatrix} \mathbf{R}_\mathrm{cl} \\ \mathbf{R}_\mathrm{vt} \end{pmatrix} \boldsymbol{\varrho} + \begin{pmatrix} \mathbf{0} \\ \boldsymbol{b}_\mathrm{V} \end{pmatrix}\,, \tag{3.45}$$

which is similar to the one for the VCFVM. However, it is about twice as large due to the introduction of the fluxes D_i as solution variables, and there are also about $N_\mathrm{G}+1$ times as many entries as before in $\boldsymbol{\varrho}$.

After solving the system, the electric field can be evaluated by

$$E(x) = E^\mathrm{a}(x) + \widetilde{E}(x)\,, \tag{3.46}$$

with

$$E^\mathrm{a}(x) = -\frac{\mathrm{d}\varphi^\mathrm{a}}{\mathrm{d}x} = \frac{1}{\varepsilon}\left(\frac{1}{2}\big(D^+ + D^-\big) + \frac{x}{\Delta x}\big(D^+ - D^-\big)\right) \tag{3.47}$$

and

$$\widetilde{E}(x) = -\frac{\mathrm{d}\widetilde{\varphi}}{\mathrm{d}x} = -\sum_{s=0}^{N_\mathrm{G}+1} \frac{\mathrm{d}}{\mathrm{d}x} d_s(x)(\varrho_s - \overline{\varrho}) = -\sum_{s=0}^{N_\mathrm{G}+1} \frac{\mathrm{d}}{\mathrm{d}x}\widetilde{d}_s(x)\varrho_s\,. \tag{3.48}$$

3.2.3 Nonlinear Poisson Equation

In the previous section the charge density was assumed to be known. However, when the quasi Fermi potentials $\Phi^\mathrm{n}(x)$ and $\Phi^\mathrm{p}(x)$ are provided instead, the charge density is effectively coupled to the potential

$$\varrho = e\left(N_\mathrm{D} - N_\mathrm{A} - n_\mathrm{i}\exp\left(\frac{\varphi - \Phi^\mathrm{n}}{V_\mathrm{T}}\right) + n_\mathrm{i}\exp\left(\frac{\Phi^\mathrm{p} - \varphi}{V_\mathrm{T}}\right)\right)\,, \tag{3.49}$$

resulting in the Non-Linear Poisson Equation (NLPE). In the case of the VCFVM it can easily be solved by a Newton iteration, since there is the same number of discrete charge densities as there are discrete potential values; the number of equations therefore does not increase and the system size stays the same. However for the CCFVM this is not the case, since the number of charge densities is much larger than the number of potentials and fluxes.

To avoid having to solve a larger system, the solution strategy is to use a two-level Newton iteration, i.e. at the bottom level the NLPE is solved cell-wise by introducing potentials at each Gauss-Legendre node, while the average potential and the fluxes are kept constant. This part of the iteration can be effectively parallelized, because all cells are independent. From the resulting node potentials the charge density at each node and the potential at the cell boundaries can be calculated, which is then used at the top level of the iteration to yield the cell average potentials and the electric fluxes.

Considering a single cell, the potential at the Gauss-Legendre node x_l is

$$\varphi_l = \varphi_l^{\mathrm{a}} + \widetilde{\varphi}_l \,, \tag{3.50}$$

where

$$\varphi_l^{\mathrm{a}} = \overline{\varphi} + \frac{1}{\varepsilon}\left(\left(\frac{\Delta x}{24} - \frac{x_l^2}{2\Delta x}\right)\left(D^+ - D^-\right) - \frac{x_l}{2}\left(D^+ + D^-\right)\right) \tag{3.51}$$

is given by eq. (3.34) and can be evaluated directly. When eq. (3.49) is inserted into eq. (3.43), an indirect equation for the potential fluctuation is received

$$\widetilde{\varphi}_l = \sum_{k=0}^{N_{\mathrm{G}}+1} d_k(x_l) e \left(N_{\mathrm{D}} - N_{\mathrm{A}} - n_{\mathrm{i}} \exp\left(\frac{\varphi_k - \Phi_k^{\mathrm{n}}}{V_{\mathrm{T}}}\right) + n_{\mathrm{i}} \exp\left(\frac{\Phi_k^{\mathrm{p}} - \varphi_k}{V_{\mathrm{T}}}\right)\right) . \tag{3.52}$$

Inserting this relation into eq. (3.50) yields the residual equation

$$\varphi_l - \varphi_l^{\mathrm{a}} - \sum_{k=0}^{N_{\mathrm{G}}+1} d_k(x_l) e \left(N_{\mathrm{D}} - N_{\mathrm{A}} - n_{\mathrm{i}} \exp\left(\frac{\varphi_k - \Phi_k^{\mathrm{n}}}{V_{\mathrm{T}}}\right) + n_{\mathrm{i}} \exp\left(\frac{\Phi_k^{\mathrm{p}} - \varphi_k}{V_{\mathrm{T}}}\right)\right) = f_k(\boldsymbol{\varphi}) \overset{!}{=} 0 \,, \tag{3.53}$$

where the components of $\boldsymbol{\varphi}$ are the sought-after φ_l. Equation (3.53) is a coupled system of $N_{\mathrm{G}} + 2$ equations, which is solved by a Newton iteration. For the initial guess of the solution the values φ_l^{a} can be used, which results in only a few iteration steps in most cases. After the solution has been found, derivatives w.r.t. the parameters $\overline{\varphi}$, D^+, D^- as well as Φ_k^{n} and Φ_k^{p} are calculated by indirect differentiation, e.g.

$$\frac{\partial \boldsymbol{\varphi}}{\partial \overline{\varphi}} = -\mathcal{J}\{\boldsymbol{f}, \boldsymbol{\varphi}\}^{-1} \frac{\partial \boldsymbol{f}}{\partial \overline{\varphi}} \,, \tag{3.54}$$

with the Jacobian matrix $\mathcal{J}\{\boldsymbol{f},\boldsymbol{\varphi}\}$. Finally, with eq. (3.49), the charge density and its derivatives are calculated, after which eqs. (3.18) and (3.21) can be evaluated for the top level of the Newton iteration.

3.2.4 Equilibrium Results

Under equilibrium conditions the QFPs should be zero in the whole device

$$\Phi^{\mathrm{n}}(x) = 0 \quad \text{and} \quad \Phi^{\mathrm{p}}(x) = 0\,, \tag{3.55}$$

and so the NLPE can already be solved for this case, without consideration of any transport model. As an example, an N$^+$-N-N$^+$ device is used here, with a doping concentration of $N_{\mathrm{D}} = 10^{20}\,\mathrm{cm}^{-3}$ in the contact regions and $N_{\mathrm{D}} = 10^{15}\,\mathrm{cm}^{-3}$ in the channel. The electrostatic permittivity is chosen as $\varepsilon = 11.7\varepsilon_0$ and the intrinsic carrier density as $n_{\mathrm{i}} = 10^{10}\,\mathrm{cm}^{-3}$. The lengths of the contact regions and the channel are $L_{\mathrm{S}} = L_{\mathrm{D}} = 40\,\mathrm{nm}$ and $L_{\mathrm{C}} = 160\,\mathrm{nm}$, respectively. An equidistant grid is used with $\Delta x = 5\,\mathrm{nm}$. Holes are neglected.

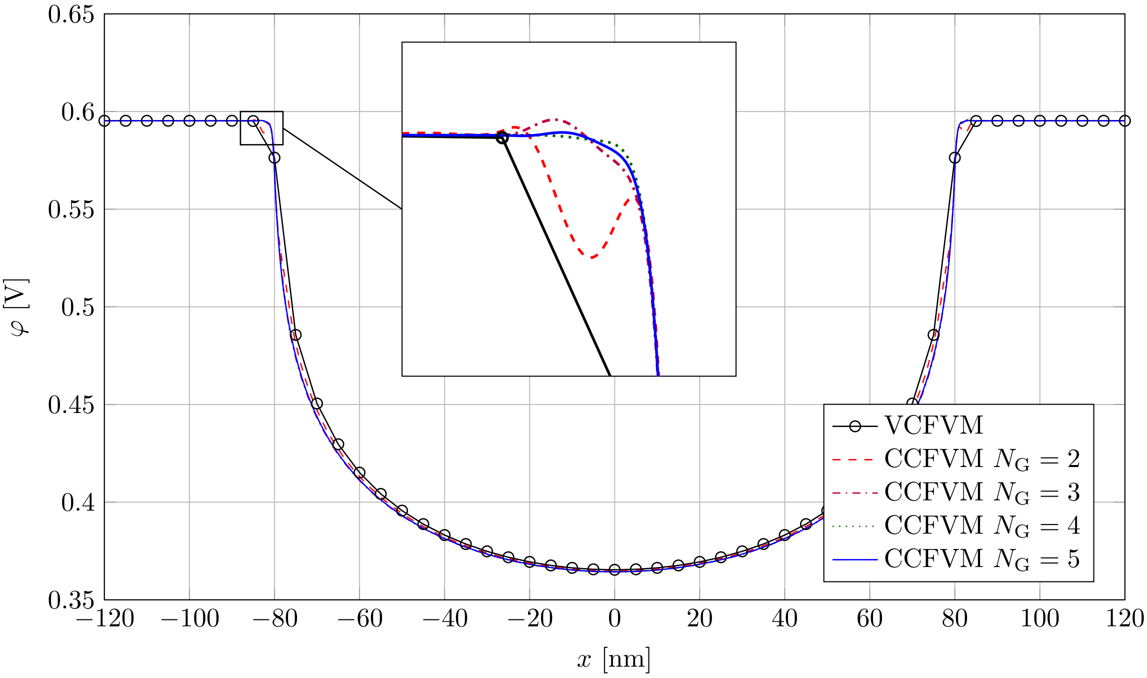

Figure 3.4: Potential for the N$^+$-N-N$^+$ device at equilibrium.

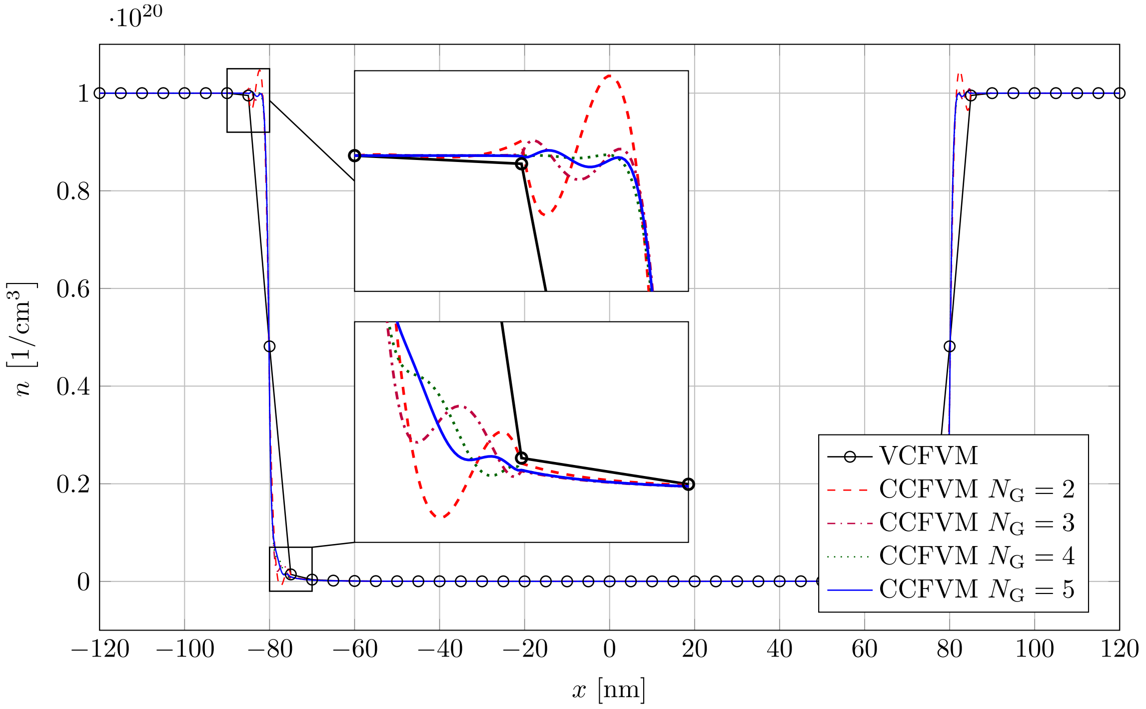

Figure 3.5: Electron density for the N$^+$-N-N$^+$ device at equilibrium.

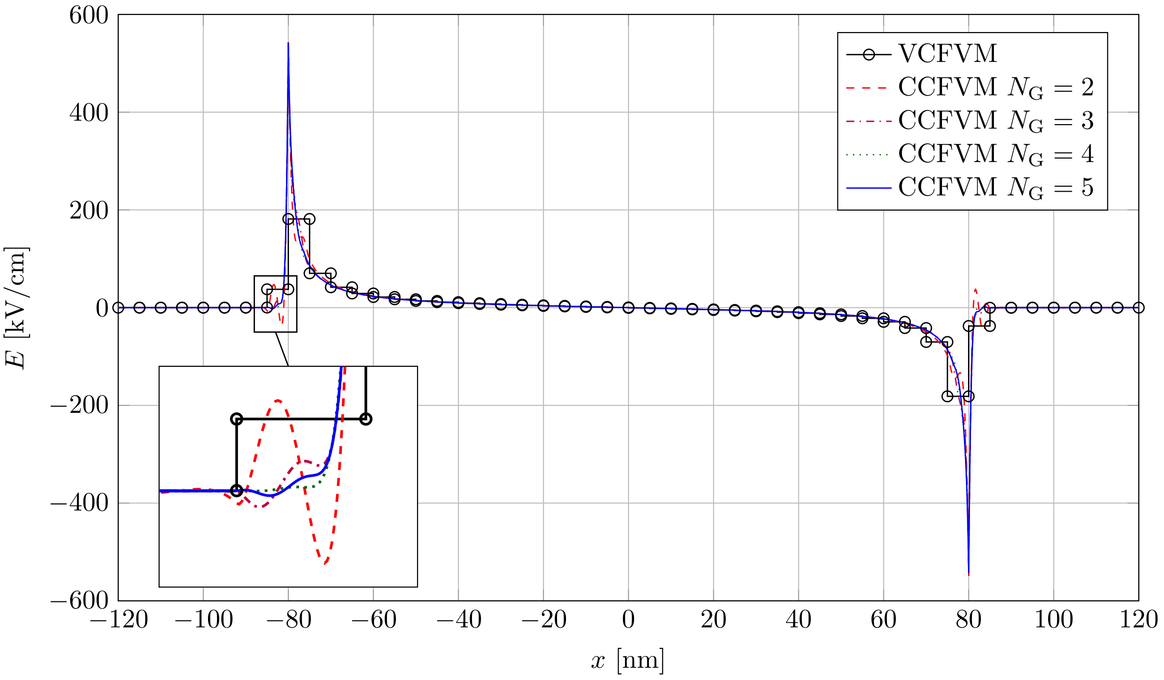

Figure 3.6: Electric field for the N$^+$-N-N$^+$ device at equilibrium.

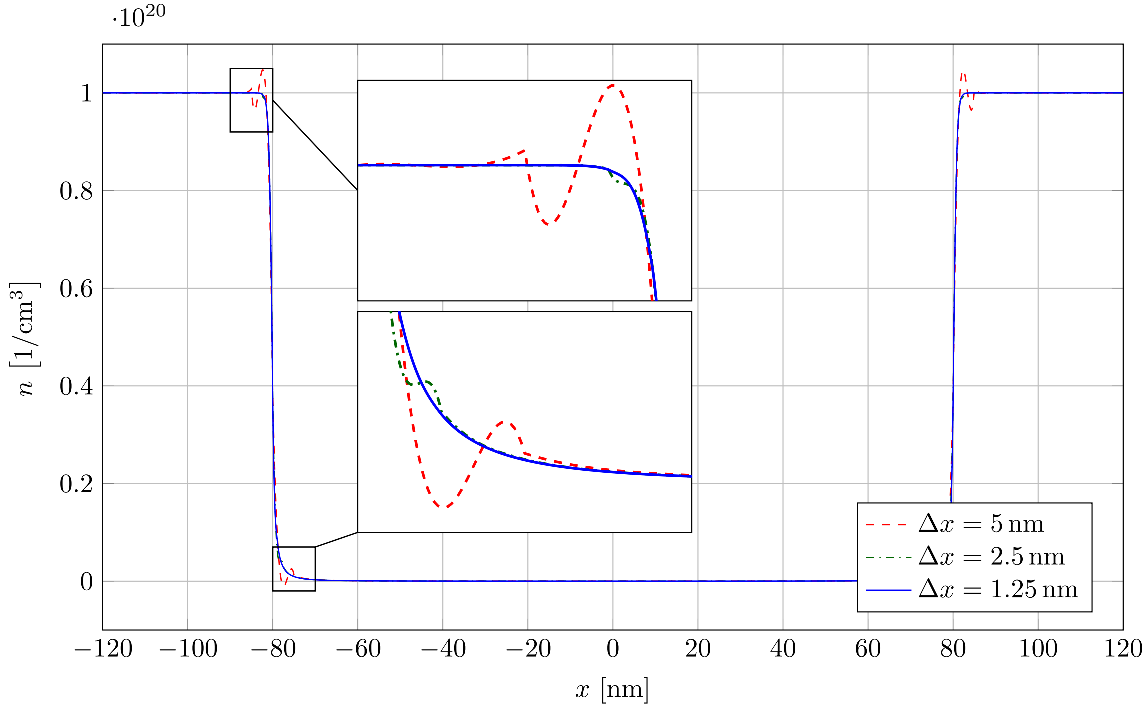

Figure 3.7: Electron density for N$^+$-N-N$^+$ device at equilibrium for the CCFVM with $N_\mathrm{G} = 2$ and different grid constants.

In Figure 3.4 the potential under equilibrium conditions is shown for both the VCFVM and the CCFVM with a varying number of Gauss-Legendre nodes per cell. While all curves have an overall similar shape, differences become apparent at the transition between the highly doped contact regions and the channel. The VCFVM with its piecewise linear behavior has in general the lowest resolution, on the other hand it appears to be also the most stable method, without any over- or undershoots. In contrast to this, the CCFVM shows some oscillatory behavior, which gets worse for smaller values of N_G. This is to be expected, because the interpolation of $\varrho(x)$ should get better, the more nodes are used.

The corresponding graphs for $n(x)$ are shown in Figure 3.5. Due to the exponential relationship between φ and n the oscillations of the CCFVM are even more pronounced here. For $N_\mathrm{G} = 2$, the oscillations become so strong, that even unphysical negative densities occur. However, this can happen only between the interpolation nodes, since for each node k in a cell $n_k = n_\mathrm{i} \exp\left(\frac{\varphi_k - \Phi_k^\mathrm{n}}{V_\mathrm{T}}\right) > 0$. Next, in Figure 3.6 the electric field is shown. Here the problem with the VCFVM becomes apparent, because its low resolution leads to a piecewise constant field. The sharp peak shown by the CCFVM is therefore not resolved properly.

Finally, the effect of the grid constant Δx is shown in Figure 3.7. Using a grid constant of $\Delta x = 2.5\,\mathrm{nm}$, the oscillations are suppressed considerably, even for the small value of $N_{\mathrm{G}} = 2$, and negative densities do not occur anymore. When the grid spacing is reduced even more to $\Delta x = 1.25\,\mathrm{nm}$, the oscillations vanish completely. In conclusion, the CCFVM provides a much better resolution for the electric field inside of a cell than the VCFVM. However, when the grid is not chosen carefully, the CCFVM can be unstable, leading to spurious oscillations that can even produce unphysical negative densities. In addition to using a finer grid, the effect can also be mitigated somewhat by increasing N_{G}.

3.3 Classical Drift-Diffusion Model

Under non-equilibrium conditions, a model is needed to describe electron transport in the device. Here, the classical DD model is presented, which is stabilized using the well-known Scharfetter-Gummel (SG) scheme [39]. It can serve as a benchmark for the numerical schemes developed in the following sections.

Neglecting holes as well as carrier generation and recombination, the classical DD in one dimension is given by the continuity equation

$$\frac{\partial n}{\partial t} + \frac{\partial j}{\partial x} = 0\,, \tag{3.56}$$

where the electron current density $j(x,t)$ is given by

$$j(x,t) = -\mu\left(En + V_{\mathrm{T}}\frac{\partial n}{\partial x}\right), \tag{3.57}$$

with the electron mobility $\mu = \frac{e\tau}{m^*}$. The SG scheme is closely related to the VCFVM for the PE, and is similarly derived by integration over an adjoint finite volume

$$\Delta x_i \frac{\partial n_i}{\partial t} + j_{i+1/2} - j_{i-1/2} = 0\,. \tag{3.58}$$

The current density at the adjoint grid points is calculated by assuming that it is constant on each interval

$$j(x) = j_{i+1/2} = \text{const} \quad \text{for} \quad x \in (x_i, x_{i+1})\,, \tag{3.59}$$

leading to the boundary value problem

$$E_{i+1/2} n + V_{\mathrm{T}}\frac{\partial n}{\partial x} = \text{const}, \quad \text{where} \quad n(x_i) = n_i \quad \text{and} \quad n(x_{i+1}) = n_{i+1}\,. \tag{3.60}$$

The electric field is also assumed to be constant in each interval, and is calculated by eq. (3.17). Solving the boundary value problem yields

$$j_{i+1/2} = -\frac{\mu V_{\mathrm{T}}}{\Delta x_{i+1/2}}\left[B\left(\frac{\varphi_{i+1}-\varphi_i}{V_{\mathrm{T}}}\right)n_{i+1} - B\left(\frac{\varphi_i - \varphi_{i+1}}{V_{\mathrm{T}}}\right)n_i\right], \tag{3.61}$$

where

$$B(x) = \frac{x}{\exp(x)-1} \quad \text{with} \quad B(0) = 1 \tag{3.62}$$

is the non-negative Bernoulli function. Together with the Dirichlet boundary conditions

$$n_1 = n_\mathrm{i} \exp\left(\frac{\phi_\mathrm{MS,S}}{V_\mathrm{T}}\right) \quad \text{and} \quad n_N = n_\mathrm{i} \exp\left(\frac{\phi_\mathrm{MS,D}}{V_\mathrm{T}}\right), \tag{3.63}$$

this results in a stable numerical scheme which guarantees non-negative densities n_i.

3.4 Hyperbolic Transport

To capture the effects of electron plasma oscillations, the time derivative of the current density must be included in the transport model, turning it into a hyperbolic system of partial differential equations. In one dimension such a model can be expressed in the following form

$$\frac{\partial \boldsymbol{U}}{\partial t} + \frac{\partial \boldsymbol{F}}{\partial x} = \boldsymbol{S}\,, \tag{3.64}$$

with the state vector $\boldsymbol{U}$ lumping together all transport variables. The flux is a function of that state $\boldsymbol{F} = \boldsymbol{F}(\boldsymbol{U})$, while the source term $\boldsymbol{S} = \boldsymbol{S}(\boldsymbol{U}, E)$ depends on the state as well, but is additionally dependent on the electric field. For the hyperbolic DD and the CDD model, these vectors are given by

$$\boldsymbol{U} = \begin{pmatrix} n \\ j \end{pmatrix}\,, \quad \boldsymbol{F} = \begin{pmatrix} j \\ c_{\mathrm{T}}^2 n \left[+ \frac{j^2}{n} \right] \end{pmatrix} \quad \text{and} \quad \boldsymbol{S} = \begin{pmatrix} 0 \\ -\frac{e}{m^*} E n - \frac{j}{\tau} \end{pmatrix}\,, \tag{3.65}$$

where the convective term indicated by the square brackets is only present in the CDD model. The thermal velocity $c_{\mathrm{T}} = \sqrt{\frac{k_{\mathrm{B}} T}{m^*}}$ is introduced as an abbreviation, which will make more sense in the context of the later introduced Riemann solvers. As opposed to the parabolic classical DD model, hyperbolic transport models can not be stabilized by the SG scheme, and different methods need to be developed.

3.4.1 Godunov's Scheme

One of the simplest methods to solve equations in the form of eq. (3.64) numerically is Godunov's Scheme [40], which is also a finite volume scheme. Integration of eq. (3.64) over a grid cell leads to

$$\frac{\partial}{\partial t} \overline{\boldsymbol{U}}_{i+1/2} + \frac{1}{\Delta x_{i+1/2}} (\boldsymbol{F}_{i+1} - \boldsymbol{F}_i) = \overline{\boldsymbol{S}}_{i+1/2}\,, \tag{3.66}$$

where $\overline{\boldsymbol{U}}_{i+1/2}$ and $\overline{\boldsymbol{S}}_{i+1/2}$ are cell averages of $\boldsymbol{U}$ and $\boldsymbol{S}$, respectively. In order to ensure conservation, at each cell interface a single numerical flux $\boldsymbol{F}_i$ must be used, which is shared between the two neighboring cells. Using the $\overline{\boldsymbol{U}}_{i+1/2}$ as solution variables, the state in each cell is obtained from the piecewise constant reconstruction

$$\boldsymbol{U}(x) \approx \overline{\boldsymbol{U}}_{i+1/2} \quad \text{for} \quad x \in (x_i, x_{i+1})\,. \tag{3.67}$$

The problem that arises, is that at the cell interfaces the reconstructed state is discontinuous, however, a single, unambiguous flux must be computed to ensure conservation. Using a simple arithmetic average $\boldsymbol{F}_i = \boldsymbol{F}\left(\frac{1}{2}\left(\overline{\boldsymbol{U}}_{i+1/2} + \overline{\boldsymbol{U}}_{i-1/2}\right)\right)$ is highly problematic, since it does not take the direction of information flow into account and therefore leads to spurious oscillations. Instead, the flux must be properly upwinded, to which end a Riemann solver is used. This results in a special interface state

$$\boldsymbol{U}_i^* = \boldsymbol{U}_i^*\left(\boldsymbol{U}\left(x_i^-\right), \boldsymbol{U}\left(x_i^+\right)\right), \tag{3.68}$$

that is given by either an exact or approximate solution of the underlying system of partial differential equations.

3.4.2 Riemann Solver

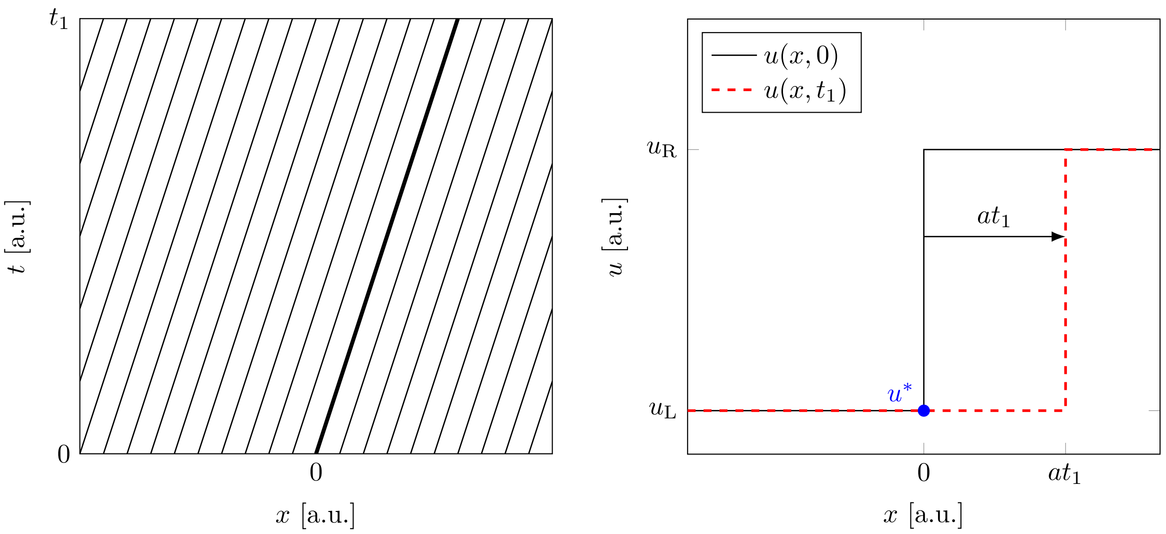

(a) Curves along which $u = \text{const.}$ (b) Corresponding solution.

Figure 3.8: Characteristic curves and the corresponding solution to the linear advection equation with $a > 0$ for the two times $t = 0$ and $t = t_1 > 0$.

To understand the functionality of a Riemann solver, it is best to start with the simplest possible hyperbolic PDE, the linear advection equation

$$\frac{\partial u}{\partial t} + a\frac{\partial u}{\partial x} = 0\,, \tag{3.69}$$

where $u(x,t)$ is a scalar quantity and $a = \text{const}$ is the constant advection velocity. Given the initial data

$$u(x,0) = \begin{cases} u_\mathrm{L} & \text{for} \quad x < 0 \\ u_\mathrm{R} & \text{for} \quad x > 0 \end{cases}\,, \tag{3.70}$$

the solution at a time $t_1 > 0$ can be computed directly by the method of characteristics. It is given by

$$u(x,t_1) = \begin{cases} u_\mathrm{L} & \text{for} \quad x < at_1 \\ u_\mathrm{R} & \text{for} \quad x > at_1 \end{cases}\,. \tag{3.71}$$

The initial discontinuity is therefore traveling as a wave with the constant velocity of a (see Figure 3.8), resulting in the interface state

$$u^* = u(0,t_1) = \begin{cases} u_\mathrm{L} & \text{for} \quad a > 0 \\ u_\mathrm{R} & \text{for} \quad a < 0 \end{cases}\,. \tag{3.72}$$

With this trivial result as a starting point, a Riemann solver for linear systems of PDEs, e.g. the linear DD model is developed first. Next, Burgers' equation is used to showcase the effect of nonlinearity in the underlying PDE system. This is then adapted to the nonlinear CDD model which includes the convective derivative. Finally, for the sake of completeness, Roe's solver is shown as an example for approximate Riemann solvers that can be used for more complex systems.

3.4.2.1 Riemann Solver for the hyperbolic Drift Diffusion Model

The hyperbolic one-dimensional DD model without source term can be written as

$$\frac{\partial}{\partial t}\begin{pmatrix} n \\ j \end{pmatrix} + \frac{\partial}{\partial x}\begin{pmatrix} j \\ c_\mathrm{T}^2 n \end{pmatrix} = \begin{pmatrix} 0 \\ 0 \end{pmatrix}\,. \tag{3.73}$$

The inclusion of the source term would lead to the gradual change of the interface state over time. It can be safely ignored, since only the state at an infinitesimal time $t_1 > 0$

is of interest here.

As before, the initial conditions are assumed to be two constant states connected by a discontinuity

$$n(x,0) = \begin{cases} n_\mathrm{L} & \text{for} \quad x < 0 \\ n_\mathrm{R} & \text{for} \quad x > 0 \end{cases} \quad \text{and} \quad j(x,0) = \begin{cases} j_\mathrm{L} & \text{for} \quad x < 0 \\ j_\mathrm{R} & \text{for} \quad x > 0 \end{cases} \,. \tag{3.74}$$

To get the solution at $t_1 > 0$, the two equations need to be decoupled. To that end, the flux Jacobian $\mathbf{A} = \mathcal{J}\{\boldsymbol{F}, \boldsymbol{U}\}$, containing the derivatives of $\boldsymbol{F}$ w.r.t. $\boldsymbol{U}$, and its eigendecomposition are calculated

$$\mathbf{A} = \begin{pmatrix} 0 & 1 \\ c_\mathrm{T}^2 & 0 \end{pmatrix} = \begin{pmatrix} 1 & 1 \\ -c_\mathrm{T} & c_\mathrm{T} \end{pmatrix} \begin{pmatrix} -c_\mathrm{T} & 0 \\ 0 & c_\mathrm{T} \end{pmatrix} \begin{pmatrix} \frac{1}{2} & -\frac{1}{2c_\mathrm{T}} \\ \frac{1}{2} & \frac{1}{2c_\mathrm{T}} \end{pmatrix} \,. \tag{3.75}$$

Multiplying eq. (3.73) by the left eigenvector matrix then yields the decoupled system

$$\frac{\partial}{\partial t} \begin{pmatrix} \alpha \\ \beta \end{pmatrix} + \begin{pmatrix} -c_\mathrm{T} & 0 \\ 0 & c_\mathrm{T} \end{pmatrix} \frac{\partial}{\partial x} \begin{pmatrix} \alpha \\ \beta \end{pmatrix} = \begin{pmatrix} 0 \\ 0 \end{pmatrix} , \tag{3.76}$$

where both equations have the same form as the linear advection equation, with the two characteristic velocities $\pm c_\mathrm{T}$. The corresponding characteristic variables are

$$\begin{pmatrix} \alpha \\ \beta \end{pmatrix} = \begin{pmatrix} \frac{1}{2} & -\frac{1}{2c_\mathrm{T}} \\ \frac{1}{2} & \frac{1}{2c_\mathrm{T}} \end{pmatrix} \begin{pmatrix} n \\ j \end{pmatrix} = \begin{pmatrix} \frac{n}{2} - \frac{j}{2c_\mathrm{T}} \\ \frac{n}{2} + \frac{j}{2c_\mathrm{T}} \end{pmatrix} \,. \tag{3.77}$$

Since $c_\mathrm{T} > 0$, the interface state for the transformed system is then

$$\begin{aligned} \alpha^* &= \alpha_\mathrm{R} = \frac{n_\mathrm{R}}{2} - \frac{j_\mathrm{R}}{2c_\mathrm{T}} \\ \beta^* &= \beta_\mathrm{L} = \frac{n_\mathrm{L}}{2} + \frac{j_\mathrm{L}}{2c_\mathrm{T}} \,. \end{aligned} \tag{3.78}$$

Back transformation to the original variables finally yields

$$\begin{aligned} n^* &= \frac{1}{2}(n_\mathrm{L} + n_\mathrm{R}) + \frac{1}{2c_\mathrm{T}}(j_\mathrm{L} - j_\mathrm{R}) \\ j^* &= \frac{1}{2}(j_\mathrm{L} + j_\mathrm{R}) + \frac{c_\mathrm{T}}{2}(n_\mathrm{L} - n_\mathrm{R}) \,. \end{aligned} \tag{3.79}$$

In addition to the arithmetic average, this also contains a correction term which mixes n and j. The resulting flux

$$\boldsymbol{F}^* = \frac{1}{2}\begin{pmatrix} j_\mathrm{R} + j_\mathrm{L} \\ c_\mathrm{T}^2 n_\mathrm{R} + c_\mathrm{T}^2 n_\mathrm{L} \end{pmatrix} - \frac{c_\mathrm{T}}{2}\begin{pmatrix} n_\mathrm{R} - n_\mathrm{L} \\ j_\mathrm{R} - j_\mathrm{L} \end{pmatrix} \tag{3.80}$$

is closely related to the Lax-Friedrichs flux [41].

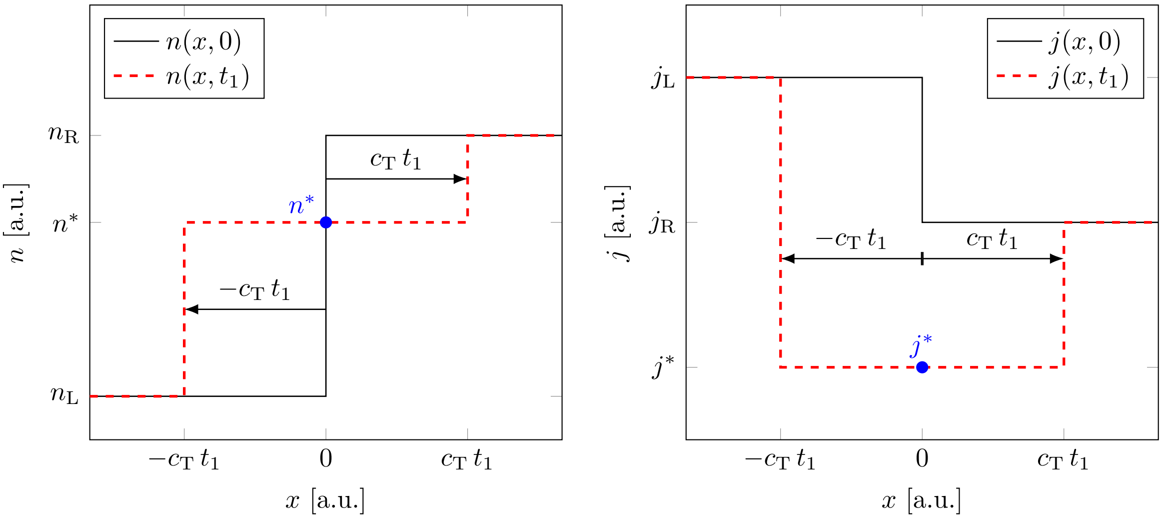

(a) Electron density.

(b) Electron current density.

Figure 3.9: Example solution for the linear, hyperbolic DD model without source term for the times $t = 0$ and $t = t_1$.

In Figure 3.9 an example solution is shown. In contrast to the scalar advection equation, there are now two moving waves with the velocities $\pm c_\mathrm{T}$, in between which a constant state develops.

3.4.2.2 Riemann Solver for Burgers' Equation

The simplest nonlinear hyperbolic PDE is Burgers' equation [42, 43], which in conservative form is given by

$$\frac{\partial u}{\partial t} + \frac{\partial}{\partial x}\left(\frac{1}{2}u^2\right) = 0\,. \tag{3.81}$$

In regions where u is continuously differentiable, this is equivalent to the non-conservative, quasi-linear form

$$\frac{\partial u}{\partial t} + u\frac{\partial u}{\partial x} = 0\,, \tag{3.82}$$

which highlights its similarity to the linear advection equation. However, unlike before, the wave velocity in Burgers' equation is not constant, but rather given by the state variable $u(x,t)$ itself. This has some important consequences, in that the wave is not a simple moving discontinuity anymore. Using the initial conditions

$$u(x,0) = \begin{cases} u_\mathrm{L} & \text{for} \quad x < 0 \\ u_\mathrm{R} & \text{for} \quad x > 0 \end{cases} , \tag{3.83}$$

depending on the relation between u_L and u_R, rarefaction or shock waves can develop.

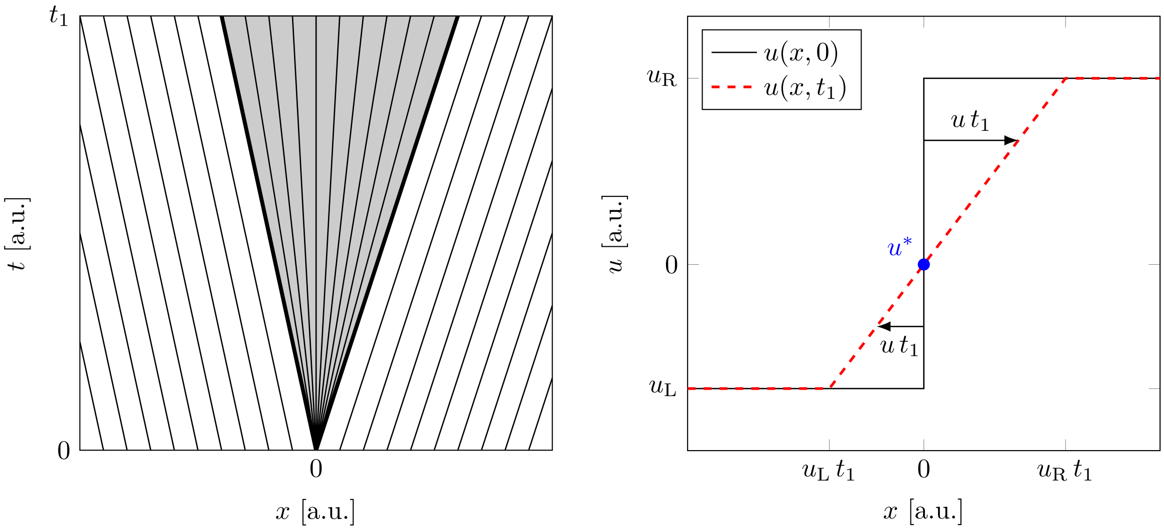

(a) Characteristic curves.

(b) Corresponding solution.

Figure 3.10: Rarefaction Wave for Burgers' Equation with $u_\mathrm{L} < u_\mathrm{R}$, in fact $u_\mathrm{L} < 0$ and $u_\mathrm{R} > 0$.

Starting with the case that $u_\mathrm{L} < u_\mathrm{R}$, it is clear that characteristic curves starting from $x > 0$ will move at a faster speed than curves starting from $x < 0$. Therefore, a gap between the two straight lines

$$x_\mathrm{L}(t) = u_\mathrm{L} t \quad \text{and} \quad x_\mathrm{R}(t) = u_\mathrm{R} t \tag{3.84}$$

will form (see Figure 3.10). Since all information about the solution at $t > 0$ must be contained in the initial data from $t = 0$ (otherwise the entropy condition would be violated), all characteristic curves must start at $t = 0$, and so in the gap a so-called rarefaction fan develops (shaded area in Figure 3.10a).

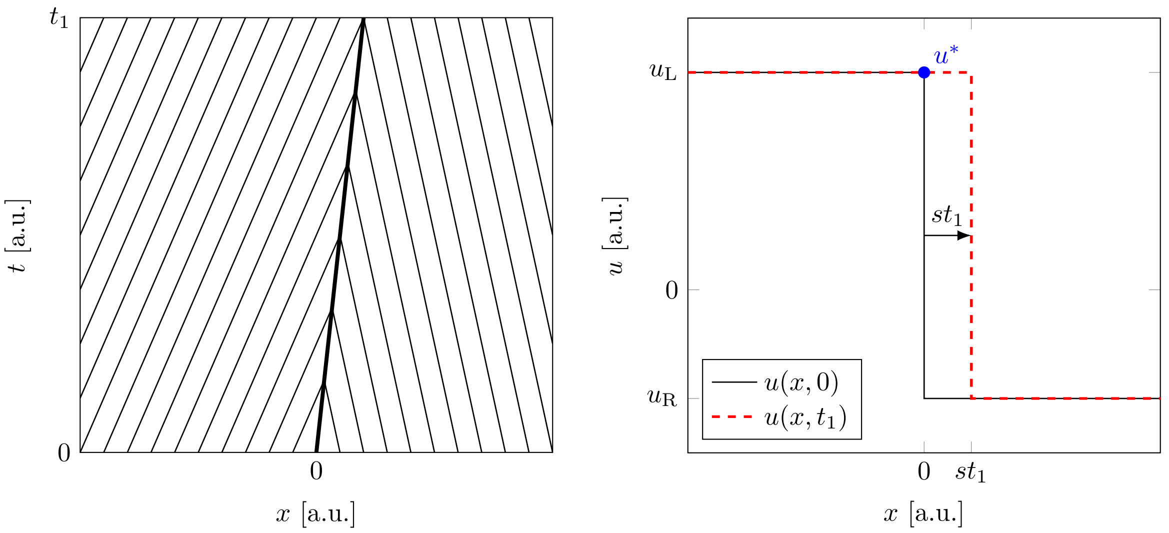

(a) Characteristic curves.

(b) Corresponding solution.

Figure 3.11: Shock wave for Burgers' Equation with $u_\mathrm{L} > u_\mathrm{R}$.

In the opposite case, where u_L is larger than u_R, the curves will collide with each other and a shock wave will form (see Figure 3.11). The velocity of the shock wave is given by the Rankine-Hugoniot jump conditions [44, 45, 46], where the flux difference is assumed to be proportional to the state difference over the wave

$$s(u_\mathrm{R} - u_\mathrm{L}) = \frac{1}{2}u_\mathrm{R}^2 - \frac{1}{2}u_\mathrm{L}^2\,, \tag{3.85}$$

with the proportionality factor s being the velocity of the shock wave. In this case it is given by

$$s = \frac{1}{2}(u_\mathrm{L} + u_\mathrm{R})\,. \tag{3.86}$$

The solution procedure consists of determining the kind of wave that will develop by checking whether $u_\mathrm{L} < u_\mathrm{R}$ (rarefaction) or $u_\mathrm{L} > u_\mathrm{R}$ (shock). The interface state is then given by the corresponding value

$$u^*_\mathrm{rare} = \begin{cases} u_\mathrm{L} & \text{for} \quad u_\mathrm{L} \geq 0 \\ 0 & \text{for} \quad u_\mathrm{L} < 0 < u_\mathrm{R} \\ u_\mathrm{R} & \text{for} \quad u_\mathrm{R} \leq 0 \end{cases}\,, \quad u^*_\mathrm{shock} = \begin{cases} u_\mathrm{L} & \text{for} \quad s > 0 \\ 0 & \text{for} \quad s = 0 \\ u_\mathrm{R} & \text{for} \quad s < 0 \end{cases}\,. \tag{3.87}$$

3.4.2.3 Riemann Solver for the nonlinear CDD Model

The nonlinear CDD model without source term is given in conservative form by

$$\frac{\partial \boldsymbol{U}}{\partial t} + \frac{\partial \boldsymbol{F}}{\partial x} = \mathbf{0}\,, \tag{3.88}$$

with

$$\boldsymbol{U} = \begin{pmatrix} n \\ j \end{pmatrix} \quad \text{and} \quad \boldsymbol{F} = \begin{pmatrix} j \\ c_\mathrm{T}^2 n + \frac{j^2}{n} \end{pmatrix}\,. \tag{3.89}$$

Similar to Burgers' equation, in regions where $\boldsymbol{U}$ is continuously differentiable, it is equivalent to the non-conservative, quasi-linear form

$$\frac{\partial \boldsymbol{U}}{\partial t} + \mathbf{A}\frac{\partial \boldsymbol{U}}{\partial x} = \mathbf{0}\,, \tag{3.90}$$

with the flux Jacobian

$$\mathbf{A} = \mathcal{J}\{\boldsymbol{F}, \boldsymbol{U}\} = \begin{pmatrix} 0 & 1 \\ c_\mathrm{T}^2 - \frac{j^2}{n^2} & \frac{2j}{n} \end{pmatrix}\,. \tag{3.91}$$

Diagonalization of the quasi-linear system yields

$$\mathbf{R}^{-1}\frac{\partial \boldsymbol{U}}{\partial t} + \boldsymbol{\Lambda}\mathbf{R}^{-1}\frac{\partial \boldsymbol{U}}{\partial x} = \mathbf{0}\,, \tag{3.92}$$

where

$$\begin{aligned} \mathbf{A} &= \mathbf{R}\boldsymbol{\Lambda}\mathbf{R}^{-1} \\ &= \begin{pmatrix} \alpha & \beta \\ \alpha\left(\frac{j}{n} - c_\mathrm{T}\right) & \beta\left(\frac{j}{n} + c_\mathrm{T}\right) \end{pmatrix} \begin{pmatrix} \frac{j}{n} - c_\mathrm{T} & 0 \\ 0 & \frac{j}{n} + c_\mathrm{T} \end{pmatrix} \begin{pmatrix} \frac{1}{\alpha}\left(\frac{1}{2} + \frac{j}{2c_\mathrm{T} n}\right) & \frac{1}{\alpha}\left(-\frac{1}{2c_\mathrm{T}}\right) \\ \frac{1}{\beta}\left(\frac{1}{2} - \frac{j}{2c_\mathrm{T} n}\right) & \frac{1}{\beta}\left(\frac{1}{2c_\mathrm{T}}\right) \end{pmatrix} \end{aligned} \tag{3.93}$$

with the right eigenvector matrix $\mathbf{R}$ and the eigenvalues $\lambda_1 = \frac{j}{n} - c_\mathrm{T}$ and $\lambda_2 = \frac{j}{n} + c_\mathrm{T}$ corresponding to the wave velocities. The scaling factors $\alpha = \alpha(n, j)$ and $\beta = \beta(n, j)$ are introduced because of the non-uniqueness of eigenvectors. Using characteristic variables, the system can then be written as

$$\frac{\partial \boldsymbol{V}}{\partial t} + \boldsymbol{\Lambda}\frac{\partial \boldsymbol{V}}{\partial x} = \mathbf{0}\,, \tag{3.94}$$

where

$$\frac{\partial \boldsymbol{U}}{\partial V_i} = \boldsymbol{R}_i\,, \tag{3.95}$$

with $\boldsymbol{R}_i$ being the i-th column of $\mathbf{R}$.

Similar to Burgers' equation, the nonlinearity leads to rarefaction and shock waves in the solution to the Riemann problem. However, because there are two characteristic velocities, there will also be two waves like in the linear DD model. Between those two waves, which from here on will be called 1-wave and 2-wave (corresponding to λ_1 and λ_2), a constant state $\boldsymbol{U}_\mathrm{C}$ develops. To calculate this center state, equations relating the states across each wave need to be found.

Starting with a 1-rarefaction wave and using eq. (3.95), the relations

$$\frac{\partial n}{\partial V_1} = \alpha \quad \text{and} \quad \frac{\partial j}{\partial V_1} = \alpha\left(\frac{j}{n} - c_\mathrm{T}\right) \tag{3.96}$$

are found, where the partial derivative w.r.t. V_1 is taken under the assumption that the second characteristic V_2 is kept constant. This is indeed the case across a 1-rarefaction wave, and the two equations can be combined into

$$\frac{\mathrm{d}j}{\mathrm{d}n} = \frac{j}{n} - c_\mathrm{T}\,, \tag{3.97}$$

where the scaling factor α has been canceled. Integration of this separable differential equation yields

$$\frac{j}{n} + c_\mathrm{T}\log\left(\frac{n}{n_0}\right) = \text{const} = V_2\,, \tag{3.98}$$

where the integration constant can be identified as the second characteristic variable V_2. Analogously, for a 2-rarefaction wave the equation

$$\frac{j}{n} - c_\mathrm{T}\log\left(\frac{n}{n_0}\right) = \text{const} = V_1 \tag{3.99}$$

is found. The constants V_1 and V_2 are sometimes referred to as generalized Riemann invariants [47]. The scaling factors can now be determined as

$$\alpha = -\frac{2c_\mathrm{T}}{n} \quad \text{and} \quad \beta = \frac{2c_\mathrm{T}}{n}\,. \tag{3.100}$$

A 1-rarefaction wave connecting the left (L) and the center (C) state then gives

$$j_\mathrm{C} = n_\mathrm{C}\left(\frac{j_\mathrm{L}}{n_\mathrm{L}} + c_\mathrm{T}\log\left(\frac{n_\mathrm{L}}{n_\mathrm{C}}\right)\right). \tag{3.101}$$

For shock waves, eq. (3.95) cannot be used, since $\boldsymbol{U}$ is not continuous across shocks. Instead, similar to Burgers' equation, the Rankine-Hugoniot jump conditions are used, e.g. for a 2-shock, which connects the center (C) and the right (R) state

$$s(\boldsymbol{U}_\mathrm{R} - \boldsymbol{U}_\mathrm{C}) = \boldsymbol{F}(\boldsymbol{U}_\mathrm{R}) - \boldsymbol{F}(\boldsymbol{U}_\mathrm{C}), \tag{3.102}$$

which results in

$$s = \frac{j_\mathrm{R}}{n_\mathrm{R}} + c_\mathrm{T}\sqrt{\frac{n_\mathrm{C}}{n_\mathrm{R}}}, \tag{3.103}$$

and finally

$$j_\mathrm{C} = j_\mathrm{R} + s(n_\mathrm{C} - n_\mathrm{R}). \tag{3.104}$$

Equating eqs. (3.101) and (3.104), the density for the center state n_C can then be found by a Newton iteration.

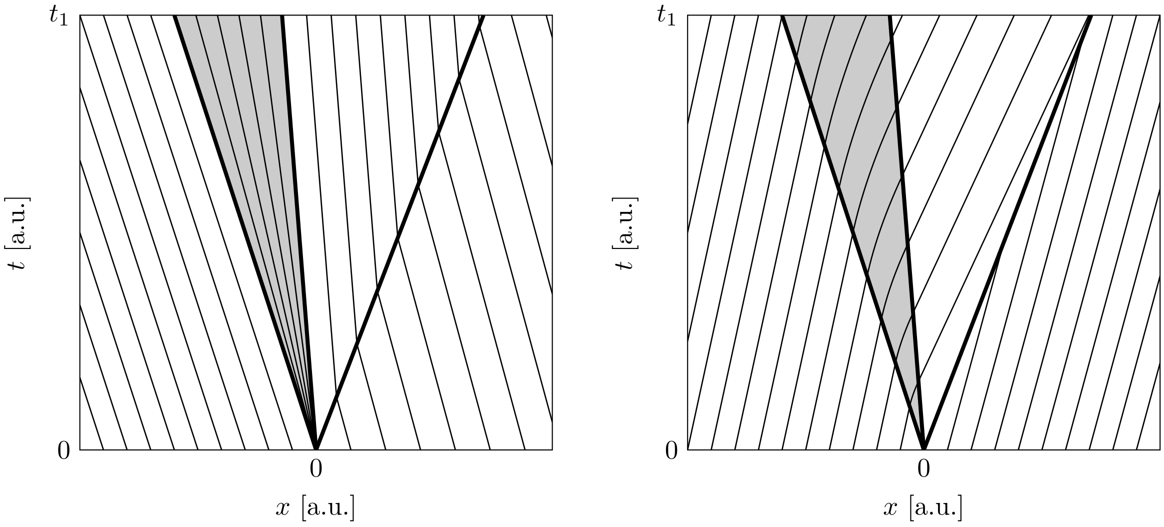

(a) Characteristic curves with $x = \lambda_1 t$.

(b) Characteristic curves with $x = \lambda_2 t$.

Figure 3.12: Example characteristic curves for the nonlinear CDD model with a 1-rarefaction and 2-shock wave for the subsonic case.

Since a 1-rarefaction combined with a 2-shock (see Figures 3.12 and 3.13) is just one

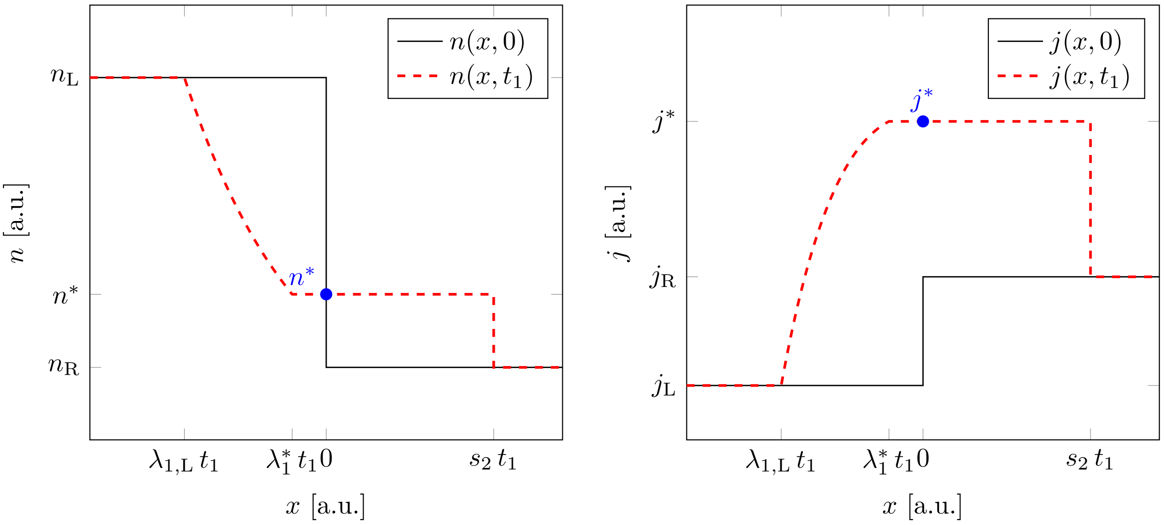

(a) Electron density.

(b) Electron current density.

Figure 3.13: Example Riemann solution for the nonlinear CDD model with a 1-rarefaction and a 2-shock wave for the subsonic case.

of four cases, for simplicity the following function is defined

$$j_2(c', n_1, j_1, n_2) = \begin{cases} n_2\left(\frac{j_1}{n_1} + c' \log\left(\frac{n_1}{n_2}\right)\right) & \text{for} \quad n_1 \geq n_2 \\ j_1 + \left(\frac{j_1}{n_1} - c'\sqrt{\frac{n_2}{n_1}}\right)(n_2 - n_1) & \text{for} \quad n_1 < n_2 \end{cases}, \tag{3.105}$$

which gives the current density of the center state for both 1- and 2-waves. The wave is selected by the sign of c', i.e. $c' = +c_{\mathrm{T}}$ for the 1-wave and $c' = -c_{\mathrm{T}}$ for the 2-wave. Depending on the densities, either the shock or the rarefaction formula is used, in accordance to the entropy condition. Finally, the equation

$$j_2(+c_{\mathrm{T}}, n_{\mathrm{L}}, j_{\mathrm{L}}, n_{\mathrm{C}}) - j_2(-c_{\mathrm{T}}, n_{\mathrm{R}}, j_{\mathrm{R}}, n_{\mathrm{C}}) \overset{!}{=} 0 \tag{3.106}$$

is solved by a Newton iteration to find n_{C} and subsequently j_{C}.

In the subsonic case ($\left|\frac{j}{n}\right| < c_{\mathrm{T}}$ everywhere), the interface state is then given directly by the central state $\boldsymbol{U}^* = \boldsymbol{U}_{\mathrm{C}}$, while in the supersonic case ($\left|\frac{j}{n}\right| > c_{\mathrm{T}}$ everywhere) the interface state is either the left or right initial state. Another possibility is the transsonic rarefaction case (similar to Figure 3.10), where the interface lies somewhere in the middle of a rarefaction wave. One part of the wave therefore travels in positive and another in negative x-direction. In that case, the characteristic speed of the wave at the interface has to be zero: $\lambda \overset{!}{=} 0$. Together with the corresponding rarefaction wave relation, this can be used to calculate $\boldsymbol{U}^*$.

3.4.2.4 Roe's approximate Riemann Solver

For more complex systems, the procedure shown for the CDD model might be too cumbersome, since the number of waves to be considered will be larger and the eigenvalue decomposition of the flux jacobian might also become quite complex (as in complicated, it should of course still be real-valued for hyperbolic systems of PDEs). Instead, the approximate Riemann solver of Roe [48] can be used. The main idea is to linearize the system by replacing the flux Jacobian by a suitable constant matrix, the Roe matrix

$$\overline{\mathbf{A}} = \overline{\mathbf{A}}(\boldsymbol{U}_\mathrm{L}, \boldsymbol{U}_\mathrm{R})\,, \tag{3.107}$$

which depends only on the two initial states, not on the instantaneous state. Additionally, $\overline{\mathbf{A}}$ must be diagonalizable with real eigenvalues to preserve hyperbolicity, and it should be consistent with the nonlinear Jacobian

$$\lim_{\substack{\boldsymbol{U}_\mathrm{L}\to\boldsymbol{U}\\ \boldsymbol{U}_\mathrm{R}\to\boldsymbol{U}}} \overline{\mathbf{A}} = \mathbf{A}(\boldsymbol{U})\,. \tag{3.108}$$

Furthermore, to ensure conservation, it is required that

$$\overline{\mathbf{A}} \cdot (\boldsymbol{U}_\mathrm{R} - \boldsymbol{U}_\mathrm{L}) = \boldsymbol{F}(\boldsymbol{U}_\mathrm{R}) - \boldsymbol{F}(\boldsymbol{U}_\mathrm{R})\,. \tag{3.109}$$

For example, a possible choice for the CDD model is

$$\overline{\mathbf{A}}_\mathrm{CDD} = \begin{pmatrix} 0 & 1 \\ c_\mathrm{T}^2 - \frac{j_\mathrm{L} j_\mathrm{R}}{n_\mathrm{L} n_\mathrm{R}} & \frac{j_\mathrm{L}}{n_\mathrm{L}} + \frac{j_\mathrm{R}}{n_\mathrm{R}} \end{pmatrix}, \tag{3.110}$$

for which eqs. (3.108) and (3.109) can easily be verified.

The approximate system

$$\frac{\partial \boldsymbol{U}}{\partial t} + \overline{\mathbf{A}} \frac{\partial \boldsymbol{U}}{\partial x} = \mathbf{0} \tag{3.111}$$

can then be solved in the same way as described for the linear DD model, by diagonalization of $\overline{\mathbf{A}}$ and therefore as a series of linear advection equations. The eigenvalue decomposition of $\overline{\mathbf{A}}$ can be done numerically, since the analytic result is not needed.

Solving the Riemann problem using the linearized Roe matrix has the effect, that the nonlinear rarefaction and shock waves of the original system are approximated by linear waves, which works reasonably well in most cases. However, a problem arises when the original system develops a transsonic rarefaction wave. In the linearized system this wave is replaced by a single linear wave either traveling in positive or negative x-direction, giving a wildly inaccurate solution for the interface state $\boldsymbol{U}^*$, and violating the entropy condition. To address this issue, a so-called entropy fix [49] can be used, e.g. the one by LeVeque [50], where in the case of a transsonic rarefaction wave, the linearized wave is explicitly split into two waves connected by a constant intermediate state. Assuming the state before and after the k-th wave are denoted by $\boldsymbol{U}_{k,\mathrm{L}}$ and $\boldsymbol{U}_{k,\mathrm{R}}$, a transsonic rarefaction wave is detected, if the wave velocities fulfill $\lambda_k(\boldsymbol{U}_{k,\mathrm{L}}) < 0$ and $\lambda_k(\boldsymbol{U}_{k,\mathrm{R}}) > 0$. In that case, the intermediate state (and therefore the interface state) is given by [50, 51]

$$\overline{\boldsymbol{U}}_k = \frac{\big(\overline{\lambda_k} - \lambda_k(\boldsymbol{U}_{k,\mathrm{L}})\big)\boldsymbol{U}_{k,\mathrm{L}} + \big(\lambda_k(\boldsymbol{U}_{k,\mathrm{R}}) - \overline{\lambda}_k\big)\boldsymbol{U}_{k,\mathrm{R}}}{\lambda_k(\boldsymbol{U}_{k,\mathrm{R}}) - \lambda_k(\boldsymbol{U}_{k,\mathrm{L}})} = \boldsymbol{U}^* \,, \tag{3.112}$$

where $\overline{\lambda_k}$ is the wave velocity of the linearized wave, i.e. the k-th eigenvalue of $\overline{\mathbf{A}}$.

3.4.3 Boundary Riemann Solver

A Riemann solver can be used to determine the interface state at each cell interface inside of the device. However, at the boundaries of the device the solver needs to be modified, since a boundary interface has only one neighboring cell as opposed to inner interfaces, and the appropriate boundary conditions must be taken into account. Starting with contacted boundaries, Dirichlet boundary conditions for the electron density are implemented. Thus, parts of the interface state are already known

$$n^*_{\mathrm{ct}} = n_{\mathrm{ct}} \,, \tag{3.113}$$

where ct is a placeholder for a vertex index of a contact. To get the current density, in the Riemann solver only the wave that flows into the device is considered, and through this, the interface state is connected to the state directly inside of the device. For example, in the case of the CDD model, eq. (3.105) is used to calculate the current density directly, since n^* is already known.

For uncontacted boundaries (not relevant in the one-dimensional case), the normal component of the current density is assumed to be zero on the interface (no incoming/outgoing flow of electrons)

$$j_i^* = 0\,. \tag{3.114}$$

The process is therefore exactly the opposite of the one for contacted boundaries: The current density is known and the density is calculated by connecting the interface state with the device state via the wave flowing into the device, while ignoring the wave that is flowing out.

3.4.4 Source Terms and Well-Balancing

So far in this work, not much thought has been given to the source term. The original scheme [40] does not contain a source term, and a naive approach would be to simply add a cell average of $\boldsymbol{S}$. However, such an approach will only work in rare cases. For pure conservation laws, a stationary solution simply consists of a constant state $\boldsymbol{U}_{\mathrm{stat}}(x) = \mathrm{const}$, since without source terms the condition $\frac{\partial \boldsymbol{U}_{\mathrm{stat}}}{\partial t} = \boldsymbol{0}$ implies that $\frac{\partial}{\partial x}\boldsymbol{F}(\boldsymbol{U}_{\mathrm{stat}}(x)) = \boldsymbol{0}$. Such a constant state can easily be approximated numerically by a finite volume scheme on a grid. On the other hand, balance laws with $\boldsymbol{S} \neq \boldsymbol{0}$ generally exhibit non-constant stationary solutions, where the flux derivative is exactly canceled by the source term

$$\frac{\partial}{\partial x}\boldsymbol{F}(\boldsymbol{U}_{\mathrm{stat}}(x)) = \boldsymbol{S}(\boldsymbol{U}_{\mathrm{stat}}(x))\,. \tag{3.115}$$

These solutions are often smooth [52], even though under certain conditions stationary shock waves will develop, leading to isolated discontinuities [53]. A numerical scheme should be able to approximate these stationary solutions reasonably well, i.e. a smooth stationary solution of the continuous system should be approximated by a smooth stationary solution of the discretized system. The simple finite volume approach as discussed before will treat flux derivatives and source terms quite differently (evaluation of fluxes at the cell surfaces vs. integration of the source term over the cell), making it difficult to exactly balance these terms, while keeping the solution smooth. The naive approach therefore leads to spurious oscillations. On the other hand, a numerical scheme which preserves smooth stationary solutions exactly is called well-balanced [54].

One way to achieve a well-balanced scheme is to introduce a new artificial variable σ, and write the system in quasi-linear form as [55]

$$\frac{\partial}{\partial t}\begin{pmatrix}\boldsymbol{U}\\ \sigma\end{pmatrix}+\begin{pmatrix}\mathbf{A} & -\boldsymbol{S}\\ 0 & 0\end{pmatrix}\frac{\partial}{\partial x}\begin{pmatrix}\boldsymbol{U}\\ \sigma\end{pmatrix}=\begin{pmatrix}0\\ 0\end{pmatrix}, \tag{3.116}$$

where $\mathbf{A}=\mathcal{J}\{\boldsymbol{F},\boldsymbol{U}\}$ is the flux Jacobian and $\frac{\partial}{\partial x}\sigma = 1$ in the continuous case. By making a piecewise constant reconstruction

$$\boldsymbol{U}(x)=\overline{\boldsymbol{U}}_{i+1/2} \quad \text{and} \quad \sigma(x)=x_{i+1/2} \quad \text{for} \quad x\in(x_i,x_{i+1})\,, \tag{3.117}$$

the effects of the source term are therefore shifted to the cell interfaces. The resulting Riemann solution will exhibit an additional stationary wave, since the modified matrix has an additional eigenvalue of 0. This can be treated by using a specialized Riemann solver, e.g. the Rankine-Hugoniot-Riemann solver from [56]. Unfortunately, it will fail in the transsonic regime, where the original waves will mix with the new stationary wave, and a much more complicated exact solver has to be used [57]. Even if such a solver is used, the solution will not necessarily be unique [57, 58], since the system is not strictly hyperbolic anymore and multiple waves can have the same wave velocity of 0. Furthermore, the piecewise constant reconstruction results in a first-order scheme, which will introduce a large amount of damping, especially at high frequencies. Nevertheless, for equations with a linear flux term, like the BTE discretized in k-space, this approach appears to work reasonably well [7, 8].

In this work, it is not necessary to achieve well-balancedness for all possible stationary solutions, since the electron plasma oscillations are simulated by a transient approach around a stationary state. Therefore, the requirement for the numerical scheme, to be well-balanced for all possible stationary solutions, can be relaxed. Instead, it will be balanced only for one particular stationary state. Hence, all variables including the electric field are split into a stationary and a dynamic part [2]

$$\begin{aligned}\boldsymbol{U}(x,t)&=\boldsymbol{U}^{\mathrm{s}}(x)+\boldsymbol{U}^{\mathrm{d}}(x,t)\\ E(x,t)&=E^{\mathrm{s}}(x)+E^{\mathrm{d}}(x,t)\,,\end{aligned} \tag{3.118}$$

where the stationary part must satisfy

$$\frac{\partial \boldsymbol{F}^{\mathrm{s}}}{\partial x} = \boldsymbol{S}^{\mathrm{s}}\,, \tag{3.119}$$

with $\boldsymbol{F}^{\mathrm{s}} = \boldsymbol{F}(\boldsymbol{U}^{\mathrm{s}})$ and $\boldsymbol{S}^{\mathrm{s}} = \boldsymbol{S}(\boldsymbol{U}^{\mathrm{s}}, E^{\mathrm{s}})$. First, the stationary eq. (3.119) is solved separately, while taking special care to ensure a smooth solution. In the next step, eq. (3.119) is subtracted from eq. (3.64), resulting in

$$\frac{\partial \boldsymbol{U}}{\partial t} + \frac{\partial}{\partial x}(\boldsymbol{F} - \boldsymbol{F}^{\mathrm{s}}) = \boldsymbol{S} - \boldsymbol{S}^{\mathrm{s}}\,, \tag{3.120}$$

which will then automatically be well-balanced for the specific solution $\boldsymbol{U}^{\mathrm{s}}(x)$, i.e. inserting $\boldsymbol{U} = \boldsymbol{U}^{\mathrm{s}}$ in eq. (3.120) results in

$$\frac{\partial \boldsymbol{U}}{\partial t} = \mathbf{0}\,. \tag{3.121}$$

That way, most of the problems arising from large source terms, e.g. resulting from the large built-in fields at the transition between different doping regions [2], can be treated by solving eq. (3.119) separately.

3.5 Stationary System

The strategy for solving the stationary system in eq. (3.119) numerically, involves calculating pseudo time derivatives for each cell, and subsequently bringing them to zero by a Newton iteration [2]. To that end, the discrete solution variables

$$\boldsymbol{U}^{\mathrm{s}}_{i+1/2} = \boldsymbol{U}^{\mathrm{s}}\big(x_{i+1/2}\big) \tag{3.122}$$

are introduced. Next, for each direct grid cell, local stationary conditions are assumed, i.e. the Ordinary Differential Equation (ODE)

$$\frac{\partial}{\partial x}\boldsymbol{U}^{\mathrm{s}}_{i+1/2}(x) = \mathbf{A}^{-1}\big(\boldsymbol{U}^{\mathrm{s}}_{i+1/2}(x)\big)\boldsymbol{S}\big(\boldsymbol{U}^{\mathrm{s}}_{i+1/2}(x), E^{\mathrm{s}}_{x,i+1/2}(x)\big) \tag{3.123}$$

is solved separately for each cell, where the discrete values $\boldsymbol{U}^{\mathrm{s}}_{i+1/2}$ are used as initial values. Thus, the ODE is solved both in positive and negative x-direction, starting from the center of each cell, up to the corresponding cell interface. Both the DD and CDD model contain the continuity equation, and so the current density is already known to be constant, and does not have to be solved for:

$$j^{\mathrm{s}}(x) = j^{\mathrm{s}}_{i+1/2} \quad \text{for} \quad x \in (x_i, x_{i+1})\,. \tag{3.124}$$

The ODE for the electron density on the other hand is

$$\frac{\partial n^{\mathrm{s}}}{\partial x} = -\frac{1}{c_{\mathrm{T}}^2}\left(\frac{e}{m^*}E^{\mathrm{s}}\,n^{\mathrm{s}} + \frac{j^{\mathrm{s}}}{\tau}\right) \tag{3.125}$$

for the DD model, and

$$\frac{\partial n^{\mathrm{s}}}{\partial x} = -\frac{\frac{e}{m^*}E^{\mathrm{s}}\,n^{\mathrm{s}} + \frac{j^{\mathrm{s}}}{\tau}}{c_{\mathrm{T}}^2 - \frac{j^{\mathrm{s}2}}{n^{\mathrm{s}2}}} \tag{3.126}$$

for the CDD model respectively. Note, that because the denominator can become zero, the CDD model does not always have a smooth stationary solution [53], so this method is limited to the subsonic case ($\left|\frac{j}{n}\right| < c_{\mathrm{T}}$).

When the PE is discretized by the VCFVM, the ODE for the DD model can be solved analytically, since the electric field is constant in each interval. The result is consistent with the SG scheme. In contrast to this, for the cell centered approach and for the CDD model in general, the ODE is solved by utilizing a numerical ODE solver. Because the ODE is stiff in general, a fifth-order fully implicit Runge-Kutta ODE solver of type Radau IIa [59] with adaptive step-size control was chosen.

This procedure results in two values at each cell interface coming from both of the two neighboring cells

$$\boldsymbol{U}_i^{\mathrm{s}-} = \lim_{x \uparrow x_i} \boldsymbol{U}^{\mathrm{s}}(x) \quad \text{and} \quad \boldsymbol{U}_i^{\mathrm{s}+} = \lim_{x \downarrow x_i} \boldsymbol{U}^{\mathrm{s}}(x)\,. \tag{3.127}$$

Integration of the original PDE system then yields [2]

$$\frac{\partial}{\partial t}\boldsymbol{U}^{\mathrm{s}}_{i+1/2} + \frac{1}{\Delta x_{i+1/2}}\big(\boldsymbol{F}\big(\boldsymbol{U}^{\mathrm{s}*}_{i+1}\big) - \boldsymbol{F}(\boldsymbol{U}^{\mathrm{s}*}_{i})\big) = \frac{1}{\Delta x_{i+1/2}} \int_{x_i}^{x_{i+1}} \boldsymbol{S}(\boldsymbol{U}^{\mathrm{s}}(x))\,\mathrm{d}x\ , \tag{3.128}$$

where the time derivative of the cell average was approximated by $\frac{\partial}{\partial t}\boldsymbol{U}^{\mathrm{s}}_{i+1/2}$. Like before, the states denoted by an asterisk $\boldsymbol{U}_i^{\mathrm{s}*}$ are solutions to the Riemann problem at each cell interface, using $\boldsymbol{U}_i^{\mathrm{s}\pm}$ as initial left and right values. With eq. (3.123), the integral over the source term can then be replaced by a flux derivative, which yields [2]

$$\frac{\partial}{\partial t}\boldsymbol{U}^{\mathrm{s}}_{i+1/2} = \frac{1}{\Delta x_{i+1/2}}\big(-\boldsymbol{F}\big(\boldsymbol{U}^{\mathrm{s}*}_{i+1}\big) + \boldsymbol{F}\big(\boldsymbol{U}^{\mathrm{s}-}_{i+1}\big) + \boldsymbol{F}(\boldsymbol{U}^{\mathrm{s}*}_{i}) - \boldsymbol{F}\big(\boldsymbol{U}^{\mathrm{s}+}_{i}\big)\big)\,. \tag{3.129}$$

Finally, using a Newton iteration, these time derivatives are brought to zero, indirectly resulting in

$$\boldsymbol{U}_i^{\mathrm{s}*} = \boldsymbol{U}_i^{\mathrm{s}+} = \boldsymbol{U}_i^{\mathrm{s}-} = \boldsymbol{U}_i^{\mathrm{s}}\,. \tag{3.130}$$

The solution is therefore not only smooth inside of each cell, but also continuous at the cell interfaces (vertices).

3.5.1 Coupling to the Poisson Equation

The stationary transport model needs to be solved self-consistently with the PE. For a Newton iteration of a fully coupled system, an initial guess that is reasonably close to the actual solution is needed, otherwise the iteration will not converge. To get such an initial guess, a typical relaxation method is the Gummel iteration [60]: Starting with an approximation for the QFP, the NLPE is solved and the electric field is calculated. In the next step, the electric field is kept constant, and the stationary transport model is solved. Finally, the resulting electron density is used in conjunction with the potential to update the QFP. The iteration is repeated, until both the potential and the QFP change from one iteration to the next is smaller than some threshold (usually about 1 mV). For the VCFVM, only one value for the QFP per vertex is needed, while for the CCFVM the QFP at all Gauss-Legendre nodes in the cell and additionally at the vertices is required. Therefore, the solution to the ODE from eq. (3.123) needs to be evaluated at each of the QFP points, such that the electron density at those points is known and the QFP can be updated.

Once the solution is known up to the desired accuracy, a full Newton iteration of the coupled system is executed. For the VCFVM this is quite simple; instead of the QFP, the electron density at the vertices is used directly for solving the PE. In contrast to this, since the CCFVM requires multiple values of either the density or the QFP per cell, additional solution variables are needed. Here, the QFPs located at all of the required positions are used, i.e. $\Phi^{\mathrm{n}}_{i+1/2,k}$ for the k-th Gauss-Legendre node in cell $i + 1/2$ and Φ^{n}_{i} for vertex i, and the NLPE instead of the PE is solved. For the additional variables, additional equations are necessary. Since the NLPE and the stationary transport model both produce values for the electron density, the consistency between them can be used for that purpose. The resulting equations are then given by

$$n^{\mathrm{s}}_{i+1/2,k} - n_{\mathrm{i}} \exp\left(\frac{\varphi_{i+1/2,k} - \Phi^{\mathrm{n}}_{i+1/2,k}}{V_{\mathrm{T}}}\right) \overset{!}{=} 0 \tag{3.131}$$

and

$$n^{\mathrm{s}}_{i} - n_{\mathrm{i}} \exp\left(\frac{\varphi_{i} - \Phi^{\mathrm{n}}_{i}}{V_{\mathrm{T}}}\right) \overset{!}{=} 0\,. \tag{3.132}$$

3.5.2 Stationary Results

The same N$^+$-N-N$^+$ device as in section 3.2.4 is used here. Additional parameters required for the non-equilibrium case are the effective mass of $m^* = 0.28621\, m_{\mathrm{e}}$ and the scattering time $\tau = 0.1\,\mathrm{ps}$, which for simplicity is assumed to be constant. The applied voltage is set to $V_{\mathrm{DS}} = 0.148\,\mathrm{V}$, which is close to the maximal value for that the CDD still has a smooth solution for this particular device. For larger voltages, the subsonic condition $\left|\frac{j}{n}\right| < c_{\mathrm{T}}$ would be violated in the channel region of the device, leading to a zero denominator in eq. (3.126). The solution would not be smooth anymore, in fact even discontinuous [53], and cannot be described using the described approach.

A grid cell size of $\Delta x = 5\,\mathrm{nm}$ was chosen, however, close to the transitions between the contact and the channel regions, this size was gradually reduced until $\Delta x = 0.5\,\mathrm{nm}$, making the grid non-equidistant with a total number of points of $N = 61$. Because for this grid the results for both the VCFVM and the CCFVM are quite similar, only the CCFVM results are shown here. The number of Gauss-Legendre nodes used is $N_\mathrm{G} = 4$.

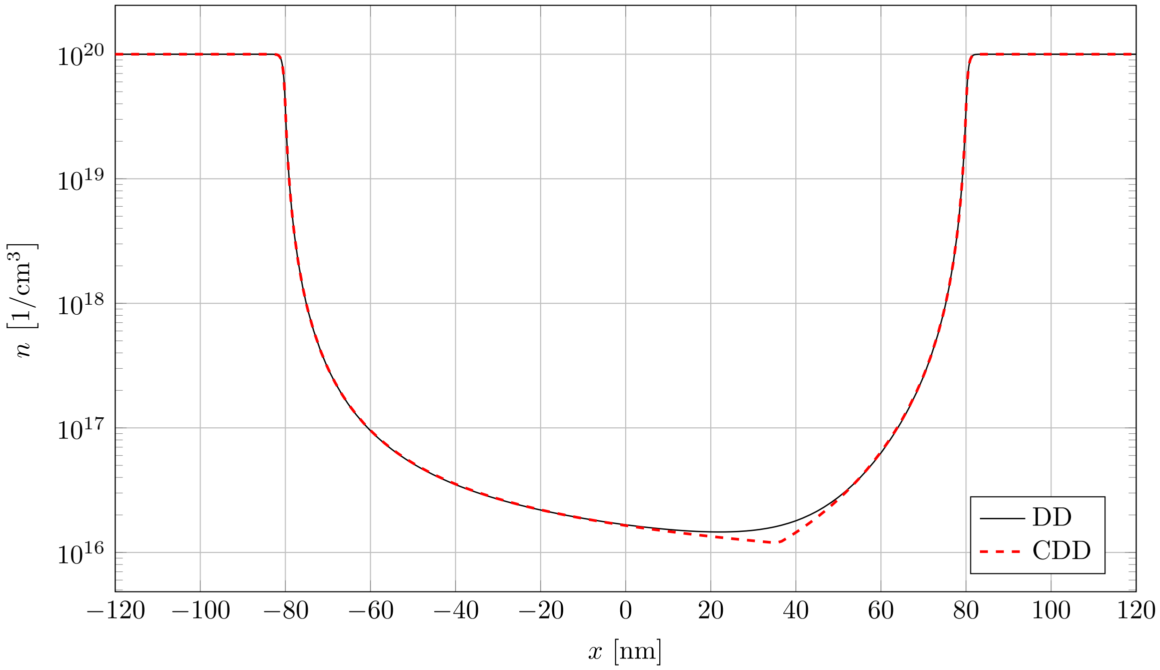

Figure 3.14: Stationary electron density for the N$^+$-N-N$^+$ device.

In Figure 3.14 the electron density for both the DD and the CDD model at the same applied voltage and with the same transport parameters are shown. For most regions in the device, the results are almost identical, only in the region of about $x = 10\,\mathrm{nm}$ to $x = 50\,\mathrm{nm}$ deviations can be seen, with the CDD model producing smaller densities. To understand this result, the additional term of the CDD model has to be examined more closely. Since the current density is constant under stationary conditions, the convective derivative can be written as $\frac{\partial}{\partial x}\frac{j^2}{n} = -\frac{j^2}{n^2}\frac{\partial n}{\partial x}$. For large densities, the n^2 in the denominator results in a negligible effect of this term, so it will only influence the solution in the channel.

Another way to look at it, is to consider the electron drift velocity $v_\mathrm{d} = \frac{j}{n}$, shown in Figure 3.15. The denominator of eq. (3.126) is then $c_\mathrm{T}^2 - v_\mathrm{d}^2$, which becomes zero when $v_\mathrm{d} \to c_\mathrm{T}$; limiting the maximal drift velocity to c_T. However, only when v_d has the same order of magnitude as c_T, the convective derivative becomes non-negligible. For the chosen voltage, the maximum of v_d comes very close to the limit c_T at $x \approx 40\,\mathrm{nm}$,

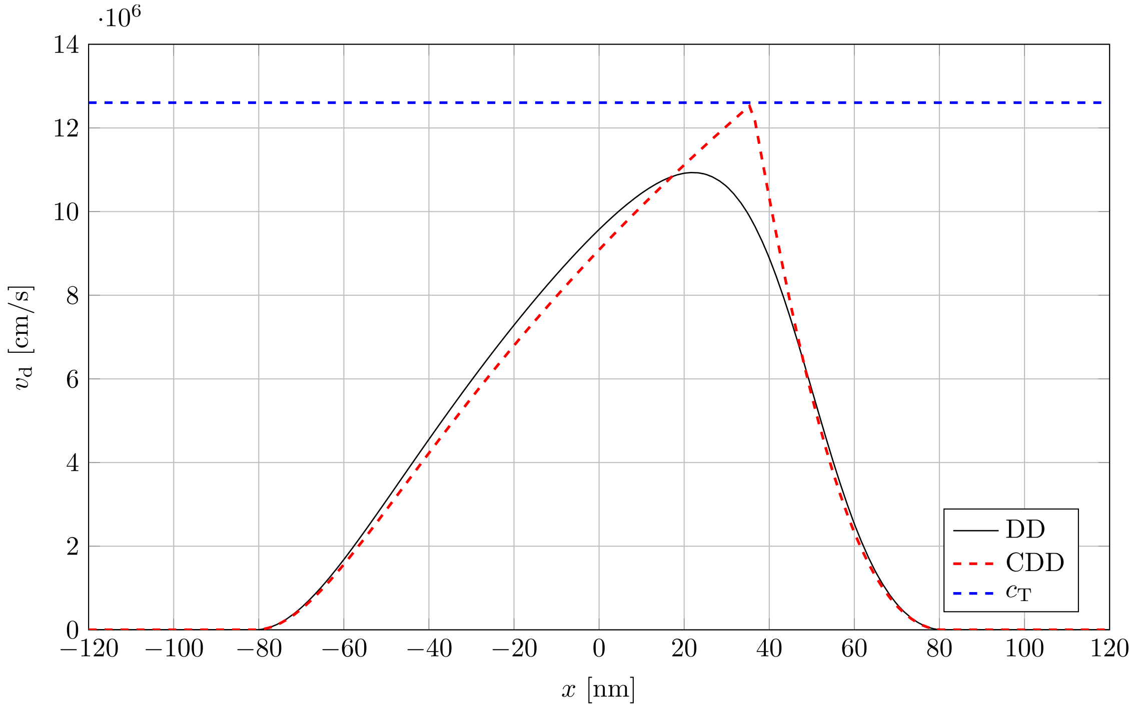

Figure 3.15: Stationary electron drift velocity for the N$^+$-N-N$^+$ device.

and exactly in that area the effects of the term are the most pronounced.

In conclusion, at least under stationary conditions, the convective term appears to be rather unimportant, especially when more advanced mobility models including velocity saturation are considered (not shown here). The model by Caughey and Thomas [61] results in a maximal drift velocity of $v_\mathrm{sat} \approx 11 \cdot 10^6\,\mathrm{cm/s}$ in silicon, which is smaller than $c_\mathrm{T} \approx 12.6 \cdot 10^6\,\mathrm{cm/s}$ at room temperature.

3.6 Dynamic System

3.6.1 Vertex-Centered Discretization of the Dynamic System

The dynamic part of the transport model is discretized differently, depending on whether the VCFVM or the CCFVM is used for the PE, because the finite volumes that are used should be the same, to avoid problems with charge conservation. For the vertex-centered approach, eq. (3.120) is integrated over an inner adjoint cell [2]

$$\Delta x_i \frac{\partial}{\partial t}\overline{\boldsymbol{U}}_i + \big(\boldsymbol{F}_{i+1/2} - \boldsymbol{F}^{\mathrm{s}}_{i+1/2}\big) - \big(\boldsymbol{F}_{i-1/2} - \boldsymbol{F}^{\mathrm{s}}_{i-1/2}\big) = \Delta x_i \big(\overline{\boldsymbol{S}}_i - \overline{\boldsymbol{S}}^{\mathrm{s}}_i\big)\,, \tag{3.133}$$

where $\overline{\boldsymbol{U}}_i = \boldsymbol{U}^{\mathrm{s}}_i + \overline{\boldsymbol{U}}^{\mathrm{d}}_i$. The dynamic part of the state is reconstructed as a piecewise constant function

$$\boldsymbol{U}^{\mathrm{d}}(x) = \overline{\boldsymbol{U}}^{\mathrm{d}}_i \quad \text{for} \quad x \in \big(x_{i-1/2}, x_{i+1/2}\big)\,, \tag{3.134}$$

and the fluxes are given by

$$\boldsymbol{F}_{i+1/2} = \boldsymbol{F}\big(\boldsymbol{U}^{*}_{i+1/2}\big) \quad \text{and} \quad \boldsymbol{F}^{\mathrm{s}}_{i+1/2} = \boldsymbol{F}\big(\boldsymbol{U}^{\mathrm{s}}_{i+1/2}\big)\,. \tag{3.135}$$

$\boldsymbol{U}^{*}_{i+1/2}$ is the Riemann solution with $\boldsymbol{U}^{\mathrm{s}}_{i+1/2} + \overline{\boldsymbol{U}}^{\mathrm{d}}_i$ and $\boldsymbol{U}^{\mathrm{s}}_{i+1/2} + \overline{\boldsymbol{U}}^{\mathrm{d}}_{i+1}$ as the left and right initial states, respectively. The source terms are calculated using weighted averages

$$\overline{\boldsymbol{S}}_i = \frac{1}{\Delta x_i}\left(\frac{\Delta x_{i-1/2}}{2}\boldsymbol{S}\big(\overline{\boldsymbol{U}}_i, E_{i-1/2}\big) + \frac{\Delta x_{i+1/2}}{2}\boldsymbol{S}\big(\overline{\boldsymbol{U}}_i, E_{i+1/2}\big)\right) \tag{3.136}$$

$$\overline{\boldsymbol{S}}^{\mathrm{s}}_i = \frac{1}{\Delta x_i}\left(\frac{\Delta x_{i-1/2}}{2}\boldsymbol{S}\big(\boldsymbol{U}^{\mathrm{s}}_i, E^{\mathrm{s}}_{i-1/2}\big) + \frac{\Delta x_{i+1/2}}{2}\boldsymbol{S}\big(\boldsymbol{U}^{\mathrm{s}}_i, E^{\mathrm{s}}_{i+1/2}\big)\right)\,, \tag{3.137}$$

with the piecewise constant electric fields given by the VCFVM.

At the boundaries, instead of integrating over a finite volume and using the modified boundary Riemann solver, in the vertex-centered approach the state at the corresponding vertex is used directly as a solution variable. The corresponding equation is eq. (3.120), where the flux derivatives are evaluated by finite differences. To that end, an expression for $\boldsymbol{U}(x)$ at these points is needed, which can be derived from the boundary conditions. For ideal ohmic contacts, the electron density is given by a Dirichlet boundary condition, while the current density should satisfy a homogeneous Neumann boundary condition [2]

$$n(x_{\mathrm{ct}}) = n^{\mathrm{s}}(x_{\mathrm{ct}}) \quad \text{and} \quad \left.\frac{\partial j}{\partial x}\right|_{x_{\mathrm{ct}}} = \left.\frac{\partial j^{\mathrm{s}}}{\partial x}\right|_{x_{\mathrm{ct}}} = 0\,, \tag{3.138}$$

where ct denotes the index of the contacted vertex (ct is a placeholder for either 1 or N). Additionally, the state in the adjacent cell at ct ± 1 is used for deriving the expressions [2]

$$n_{\mathrm{ct}}(x) \approx n^{\mathrm{s}}(x) + \overline{n}^{\mathrm{d}}_{\mathrm{ct}\pm 1} \frac{x - x_{\mathrm{ct}}}{x_{\mathrm{ct}\pm 1} - x_{\mathrm{ct}}} \tag{3.139}$$

$$j_{\mathrm{ct}}(x) \approx j^{\mathrm{s}} + j^{\mathrm{d}}_{\mathrm{ct}} + \left(\overline{j}^{\mathrm{d}}_{\mathrm{ct}\pm 1} - j^{\mathrm{d}}_{\mathrm{ct}}\right) \frac{12(x - x_{\mathrm{ct}})^2}{13(x_{\mathrm{ct}\pm 1} - x_{\mathrm{ct}})^2}\,, \tag{3.140}$$

which are consistent with the cell averages $\overline{n}^{\mathrm{d}}_{\mathrm{ct}\pm 1}$ and $\overline{j}^{\mathrm{d}}_{\mathrm{ct}\pm 1}$ in the neighboring cells, as well as the boundary conditions.

Due to the piecewise constant reconstruction, this approach is only first-order accurate. An additional disadvantage is that an extension to two dimensions is not possible, because the two-dimensional current density would have non-constant components even in the stationary case. The piecewise constant reconstruction allows the current density to change only at the integration volume interfaces, which in turn leads to the formation of moving waves with a non-vanishing amplitude, even in the stationary case. This results in artificial oscillations.

3.6.2 Cell-Centered Discretization of the Dynamic System

For the cell-centered approach, eq. (3.120) is integrated over a direct grid cell, resulting in

$$\Delta x_{i+1/2} \frac{\partial}{\partial t} \overline{\boldsymbol{U}}_{i+1/2} + \left(\boldsymbol{F}_{i+1} - \boldsymbol{F}^{\mathrm{s}}_{i+1}\right) - \left(\boldsymbol{F}_{i} - \boldsymbol{F}^{\mathrm{s}}_{i}\right) = \Delta x_{i+1/2} \left(\overline{\boldsymbol{S}}_{i+1/2} - \overline{\boldsymbol{S}}^{\mathrm{s}}_{i+1/2}\right), \tag{3.141}$$

where the cell averages $\overline{\boldsymbol{U}}_{i+1/2}$ are the discrete solution variables. The fluxes are given by $\boldsymbol{F}_i = \boldsymbol{F}(\boldsymbol{U}^*_i)$ and $\boldsymbol{F}^{\mathrm{s}}_i = \boldsymbol{F}(\boldsymbol{U}^{\mathrm{s}}_i)$, where the interface states $\boldsymbol{U}^*_i = \boldsymbol{U}^*_i\left(\boldsymbol{U}^-_i, \boldsymbol{U}^+_i\right)$ are calculated with a Riemann solver, with $\boldsymbol{U}^{\pm}_i$ being the state directly to the left and right of each interface.

To evaluate the source term averages, the Gauss-Legendre quadrature is used, similar to the CCFVM for the PE. The averages are then given by

$$\overline{\boldsymbol{S}} \approx \frac{1}{2} \sum_{k=1}^{N_\mathrm{G}} \boldsymbol{S}\big(\boldsymbol{U}_{i+1/2,k}, E_{i+1/2,k}\big) w_k \quad \text{and} \quad \overline{\boldsymbol{S}}^\mathrm{s} \approx \frac{1}{2} \sum_{k=1}^{N_\mathrm{G}} \boldsymbol{S}\big(\boldsymbol{U}^\mathrm{s}_{i+1/2,k}, E^\mathrm{s}_{i+1/2,k}\big) w_k \,, \tag{3.142}$$

with $\boldsymbol{U}^{(\mathrm{s})}_{i+1/2,k} = \boldsymbol{U}^{(\mathrm{s})}\big(x_{i+1/2,k}\big)$ and $E^{(\mathrm{s})}_{i+1/2,k} = E^{(\mathrm{s})}\big(x_{i+1/2,k}\big)$ at the Gauss-Legendre node position $x_{i+1/2,k} = x_{i+1/2} + \frac{1}{2}\Delta x_{i+1/2}\, \xi_k$.

The problem therefore has been reduced to finding approximations for $\boldsymbol{U}$ at the Gauss-Legendre nodes inside of the cell, as well as on the cell interfaces. In contrast to the original first-order scheme by Godunov, a high-order reconstruction is preferable. However, as opposed to the elliptic PE, the transport model system of PDEs is hyperbolic. Thus, $\boldsymbol{U}$ is not necessarily continuous, and any procedure reconstructing functions from cell averages must be able to take shock waves, i.e. moving discontinuities, into account. A simple piecewise polynomial ansatz function for $\boldsymbol{U}$ yields a scheme which is linear with respect to the cell averages. Yet, Godunov's theorem [62] proves that a linear and also monotonicity preserving scheme can be first-order accurate at most. In other words, when considering polynomial reconstructions, only the first-order piecewise constant reconstruction will not introduce spurious oscillations. If a higher order scheme is desired, a nonlinear reconstruction is therefore required.

3.6.3 Local Double Logarithmic Reconstruction

One candidate for such a nonlinear reconstruction is the limiter-free third order Local Double Logarithmic Reconstruction (LDLR) procedure described in [63]. Using the cell averages of three neighboring cells, it yields a reconstruction of a scalar variable for the center cell. In contrast to a polynomial reconstruction, the LDLR is local variation bounded [63], i.e. when a discontinuity is present, the local variation of the function is bounded by the cell size and therefore decreases as the grid becomes finer.

Let $\overline{u}_\mathrm{L}$, $\overline{u}_\mathrm{C}$ and $\overline{u}_\mathrm{R}$ denote the cell averages of the three neighboring cells with the respective sizes of Δx_L, Δx_C and Δx_R. The goal is to find a third order accurate reconstruction $u(x)$ for the center cell. To that end, second order accurate approximations for the slopes at both ends of the cell

$$\begin{aligned}
\frac{\partial}{\partial x}\,u(x)\bigg|_{-\frac{\Delta x_\mathrm{C}}{2}} &= \alpha_\mathrm{L}\,\overline{u}_\mathrm{L} + \alpha_\mathrm{C}\,\overline{u}_\mathrm{C} + \alpha_\mathrm{R}\,\overline{u}_\mathrm{R} + \mathcal{O}\big(\Delta x^2\big) = d_\mathrm{L} + \mathcal{O}\big(\Delta x^2\big) \\
\frac{\partial}{\partial x}\,u(x)\bigg|_{+\frac{\Delta x_\mathrm{C}}{2}} &= \beta_\mathrm{L}\,\overline{u}_\mathrm{L} + \beta_\mathrm{C}\,\overline{u}_\mathrm{C} + \beta_\mathrm{R}\,\overline{u}_\mathrm{R} + \mathcal{O}\big(\Delta x^2\big) = d_\mathrm{R} + \mathcal{O}\big(\Delta x^2\big)\,,
\end{aligned} \tag{3.143}$$

are constructed, with

$$\begin{aligned}
\alpha_\mathrm{L} &= -\frac{4\Delta x_\mathrm{C} + 2\Delta x_\mathrm{R}}{(\Delta x_\mathrm{L} + \Delta x_\mathrm{C})(\Delta x_\mathrm{L} + \Delta x_\mathrm{C} + \Delta x_\mathrm{R})} \\
\alpha_\mathrm{C} &= \frac{6\Delta x_\mathrm{C}(\Delta x_\mathrm{C} + \Delta x_\mathrm{R}) + 2(\Delta x_\mathrm{R}^2 - \Delta x_\mathrm{L}^2)}{(\Delta x_\mathrm{L} + \Delta x_\mathrm{C})(\Delta x_\mathrm{C} + \Delta x_\mathrm{R})(\Delta x_\mathrm{L} + \Delta x_\mathrm{C} + \Delta x_\mathrm{R})} \\
\alpha_\mathrm{R} &= \frac{2(\Delta x_\mathrm{L} + \Delta x_\mathrm{C})}{(\Delta x_\mathrm{C} + \Delta x_\mathrm{R})(\Delta x_\mathrm{L} + \Delta x_\mathrm{C} + \Delta x_\mathrm{R})}
\end{aligned} \tag{3.144}$$

and

$$\begin{aligned}
\beta_\mathrm{L} &= \frac{2(\Delta x_\mathrm{C} + \Delta x_\mathrm{R})}{(\Delta x_\mathrm{L} + \Delta x_\mathrm{C})(\Delta x_\mathrm{L} + \Delta x_\mathrm{C} + \Delta x_\mathrm{R})} \\
\beta_\mathrm{C} &= -\frac{6\Delta x_\mathrm{C}(\Delta x_\mathrm{L} + \Delta x_\mathrm{C}) + 2(\Delta x_\mathrm{L}^2 - \Delta x_\mathrm{R}^2)}{(\Delta x_\mathrm{L} + \Delta x_\mathrm{C})(\Delta x_\mathrm{C} + \Delta x_\mathrm{R})(\Delta x_\mathrm{L} + \Delta x_\mathrm{C} + \Delta x_\mathrm{R})} \\
\beta_\mathrm{R} &= \frac{4\Delta x_\mathrm{C} + 2\Delta x_\mathrm{L}}{(\Delta x_\mathrm{C} + \Delta x_\mathrm{R})(\Delta x_\mathrm{L} + \Delta x_\mathrm{C} + \Delta x_\mathrm{R})}\,.
\end{aligned} \tag{3.145}$$

Using these two numerical slopes, as well as requiring that

$$\frac{1}{\Delta x_\mathrm{C}}\int_{-\Delta x_\mathrm{C}/2}^{\Delta x_\mathrm{C}/2} u(x)\,\mathrm{d}x = \overline{u}_\mathrm{C}\,, \tag{3.146}$$

the function is then reconstructed as

$$u(x) = \overline{u}_\mathrm{C} + \phi(x) - \frac{1}{\Delta x_\mathrm{C}}\int_{-\Delta x_\mathrm{C}/2}^{\Delta x_\mathrm{C}/2} \phi(x)\,\mathrm{d}x\ , \tag{3.147}$$

where eq. (3.146) is fulfilled by construction and the integral is evaluated by Gaussian quadrature. The actual LDLR then gives an expression for the function $\phi(x)$

$$\begin{aligned}\phi(x) = \frac{\Delta x_{\mathrm{C}}(a-1)}{a^2(2-a)}\Bigg[&((a-1)d_{\mathrm{L}} + d_{\mathrm{R}})\log\left(\left|x + \Delta x_{\mathrm{C}}\left(\frac{1}{2} - \frac{1}{a}\right)\right|\right) \\ &-(d_{\mathrm{L}} + (a-1)d_{\mathrm{R}})\log\left(\left|x - \Delta x_{\mathrm{C}}\left(\frac{1}{2} - \frac{1}{a}\right)\right|\right)\Bigg], \qquad (3.148)\end{aligned}$$

where the “Double Logarithm” in the name refers to the two logarithms used here. The remaining parameter is

$$a = (1 - \mathrm{TOL})\left(1 + \mathrm{TOL} - \frac{2|d_{\mathrm{L}}|^q|d_{\mathrm{R}}|^q + \mathrm{TOL}}{|d_{\mathrm{L}}|^{2q} + |d_{\mathrm{R}}|^{2q} + \mathrm{TOL}}\right), \qquad (3.149)$$

which is evaluated using the recommended values of [63]

$$\mathrm{TOL} = 0.1\,\Delta x_{\mathrm{C}}^q \quad \text{and} \quad q = 1.4\,. \qquad (3.150)$$

Note, that before applying the reconstruction procedure, all quantities have to be normalized to commonly encountered values, to remove physical units as well as scaling factors. For instance, the values of the cell sizes are divided by the total length of the device.

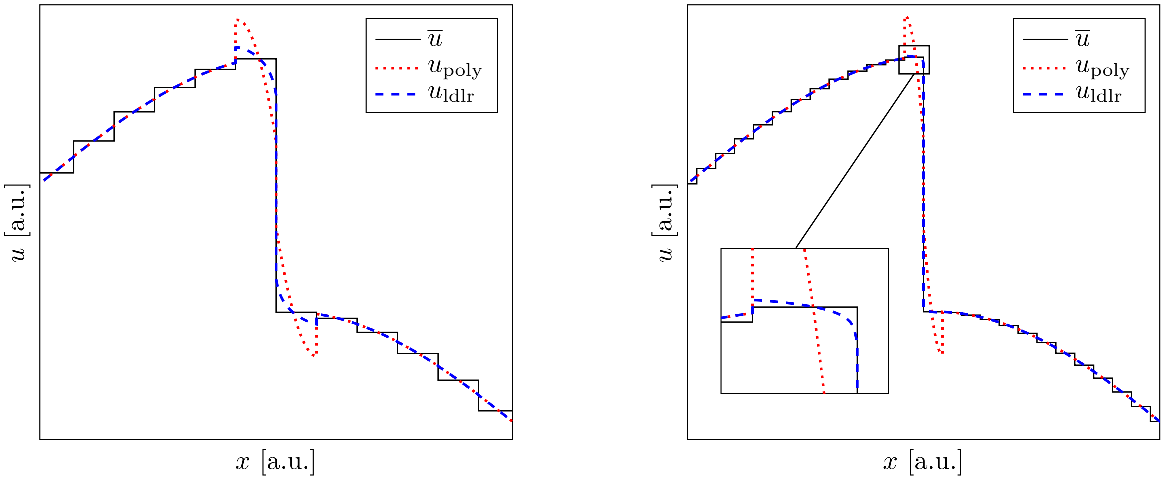

(a) Coarse grid.

(b) Fine grid.

Figure 3.16: Example for the local variation bounded LDLR compared to a polynomial (quadratic) reconstruction.

In Figure 3.16 the LDLR was applied to some example data for two different grid sizes. For comparison, a simple quadratic reconstruction also satisfying eq. (3.143) and eq. (3.146) was included as well. In smooth regions both reconstructions yield almost the same result. However, at the discontinuity the situation is quite different. Even though both functions exhibit over- and undershoots at that point, only the LDLR is local variation bounded, i.e. for finer grids the magnitude of the over- and undershoots becomes smaller, while for the polynomial reconstruction it only becomes narrower. To avoid unphysical spurious oscillations in the solution, this property of local variation boundedness is of utmost importance.

The procedure described so far only works for scalar variables in one dimension. However, $\boldsymbol{U}$ generally has multiple components, e.g. n and j. These have different requirements with regards to positivity: The current density may be positive or negative, while the density must be strictly non-negative. Even though the LDLR is much better than a polynomial reconstruction concerning over- and undershoots, even slight undershoots can result in negative values and are therefore highly problematic. To solve this issue, a modification of the LDLR that only produces non-negative values is introduced and applied to the density. For the current density, there is no requirement of non-negativity and therefore the LDLR can be applied directly. Note that in this case, the splitting into stationary and dynamic parts still needs to be taken into account, i.e. the LDLR is only applied to the dynamic part of the current density.

3.6.4 Non-Negative Local Double Logarithmic Reconstruction

In order to avoid negative values from undershoots in the reconstruction, the LDLR method is modified to work, roughly speaking, on the logarithm of the quantity to reconstruct. Thus, instead of eq. (3.147), the reconstruction of n is given by

$$n(x) = n^{\mathrm{s}}(x) + n^{\mathrm{d}}(x) = n^{\mathrm{s}}(x)\lambda \exp(\phi(x))\,. \tag{3.151}$$

To ensure consistency with the cell average value, it is required that

$$\frac{1}{\Delta x_{\mathrm{C}}} \int_{-\Delta x_{\mathrm{C}}/2}^{\Delta x_{\mathrm{C}}/2} \left(n(x) - n^{\mathrm{s}}(x)\right) \mathrm{d}x = \overline{n}_{\mathrm{C}}^{\mathrm{d}}\,, \tag{3.152}$$

and therefore the scaling factor must be

$$\lambda = \frac{\Delta x_\mathrm{C}\left(\overline{n}_\mathrm{C}^\mathrm{s} + \overline{n}_\mathrm{C}^\mathrm{d}\right)}{\int_{-\Delta x_\mathrm{C}/2}^{\Delta x_\mathrm{C}/2} n^\mathrm{s}(x)\exp(\phi(x))\,\mathrm{d}x}\,, \tag{3.153}$$

where the integral is again evaluated by Gaussian quadrature. Because the exponential term and $n^\mathrm{s}(x)$ are both non-negative, as long as $\overline{n}_\mathrm{C} = \overline{n}_\mathrm{C}^\mathrm{s} + \overline{n}_\mathrm{C}^\mathrm{d}$ is also non-negative, λ and consequently $n(x)$ will be non-negative as well.

To apply the LDLR, the two numerical slopes at the cell boundaries are still needed. To that end, the approximation

$$n(x) \approx n^\mathrm{s}(x)\exp(p(x)) \tag{3.154}$$

is used, where $p(x)$ is the quadratic polynomial

$$p(x) = p_0 + p_x x + \frac{1}{2}p_{xx}x^2\,. \tag{3.155}$$

Using the cell averages for the three cells, the following three equations can be found:

$$\begin{aligned}
\frac{1}{\Delta x_\mathrm{L}}\int_{-\Delta x_\mathrm{L}-\Delta x_\mathrm{C}/2}^{-\Delta x_\mathrm{C}/2} n^\mathrm{s}(x)\exp(p(x))\,\mathrm{d}x &= \overline{n}_\mathrm{L}^\mathrm{s} + \overline{n}_\mathrm{L}^\mathrm{d}\\
\frac{1}{\Delta x_\mathrm{C}}\int_{-\Delta x_\mathrm{C}/2}^{\Delta x_\mathrm{C}/2} n^\mathrm{s}(x)\exp(p(x))\,\mathrm{d}x &= \overline{n}_\mathrm{C}^\mathrm{s} + \overline{n}_\mathrm{C}^\mathrm{d}\\
\frac{1}{\Delta x_\mathrm{R}}\int_{\Delta x_\mathrm{C}/2}^{\Delta x_\mathrm{R}+\Delta x_\mathrm{C}/2} n^\mathrm{s}(x)\exp(p(x))\,\mathrm{d}x &= \overline{n}_\mathrm{R}^\mathrm{s} + \overline{n}_\mathrm{R}^\mathrm{d}\,.
\end{aligned} \tag{3.156}$$

Evaluating the integrals by Gaussian quadrature, Newton's method is then used to find the coefficients p_0, p_x and p_{xx}. The two numerical slopes at the cell boundaries can then be calculated as $d_\mathrm{L} = p_x - \frac{\Delta x_\mathrm{C}}{2}p_{xx}$ and $d_\mathrm{R} = p_x + \frac{\Delta x_\mathrm{C}}{2}p_{xx}$.

In Figure 3.17 the regular LDLR is compared to the non-negative reconstruction using example data for the cell averages, which was generated by directly calculating averages of two smooth functions, one for the stationary and a different one for the total values. Despite the data varying over multiple order of magnitudes, the reconstruction stays positive. In contrast to the non-negative reconstruction, the regular LDLR exhibits a negative undershoot (see Figure 3.17b).

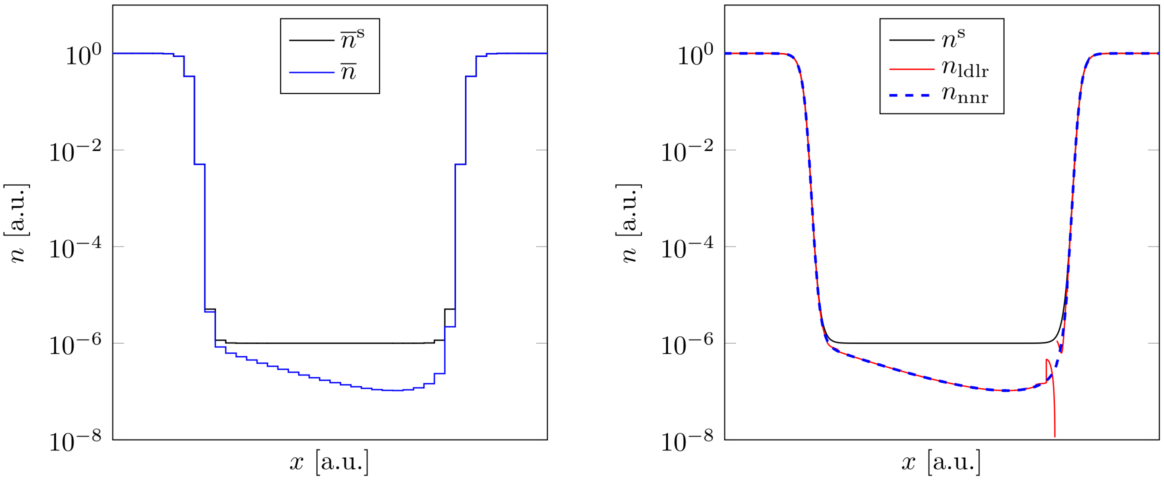

(a) Cell averages.

(b) Reconstruction.

Figure 3.17: Comparison between the non-negative $n_{\mathrm{nnr}}(x)$ and regular LDLR $n_{\mathrm{ldlr}}(x)$.

3.6.5 Testing the Dynamic System

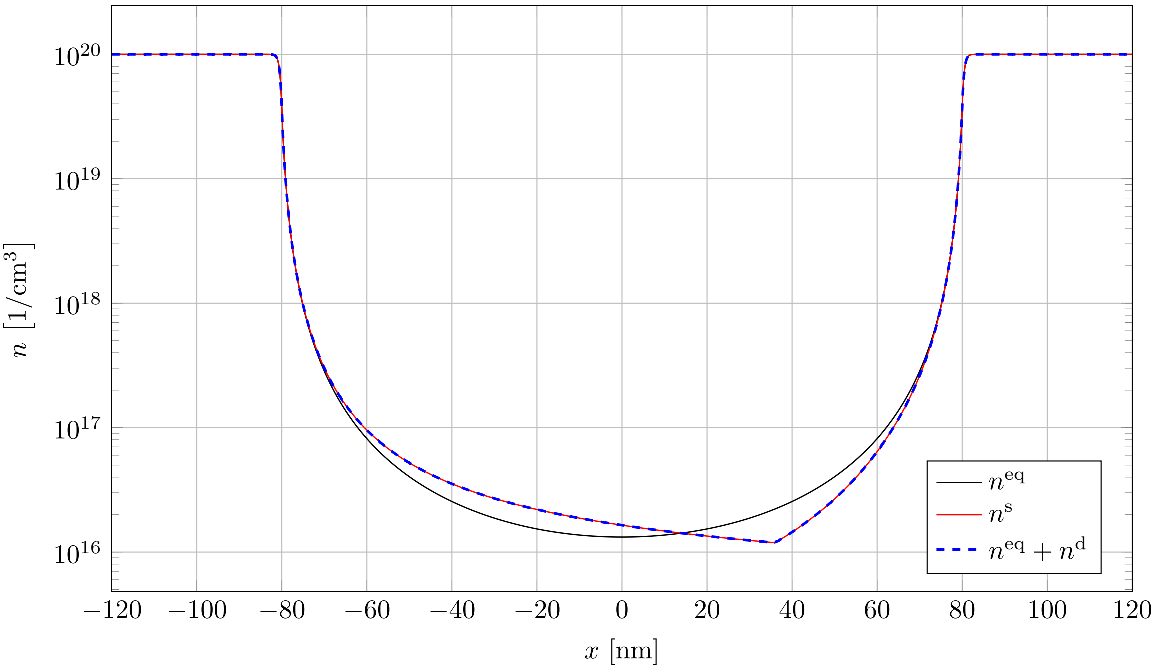

Figure 3.18: Equilibrium, stationary and total electron density for the dynamic system under stationary conditions for $V_{\mathrm{DS}} = 0.148\,\mathrm{V}$ using the CDD transport model.

In this section, both the vertex and the cell centered discretizations of the dynamic system are tested, by solving them under stationary conditions and then comparing them to the solution of the stationary system. The same N$^+$-N-N$^+$ device as before is used (however with a much more refined grid using $N = 263$ points) and the applied voltage is set to $V_{\mathrm{DS}} = 0.148\,\mathrm{V}$. Only the CDD model is considered. The number of Gauss-Legendre nodes per cell for the CCFVM is set to $N_{\mathrm{G}} = 4$.

To solve the dynamic system, an additional stationary solution is still required, which is chosen here to be the equilibrium solution $\boldsymbol{U}^{\mathrm{eq}}(x)$. The full solution to the dynamic system is then given by $\boldsymbol{U}^{\mathrm{eq}}(x) + \boldsymbol{U}^{\mathrm{d}}(x)$, which is compared to the solution to the stationary system $\boldsymbol{U}^{\mathrm{s}}(x)$.

In Figure 3.18 the electron density for both the stationary and the dynamic system is shown. Only the results for the CCFVM are included, since the VCFVM results are practically indistinguishable. There is an excellent agreement between $n^{\mathrm{s}}(x)$ and $n^{\mathrm{eq}}(x)+n^{\mathrm{d}}(x)$, even though the latter is only approximately well-balanced. The solution exhibits no spurious oscillations, and, as expected, the density stays non-negative.

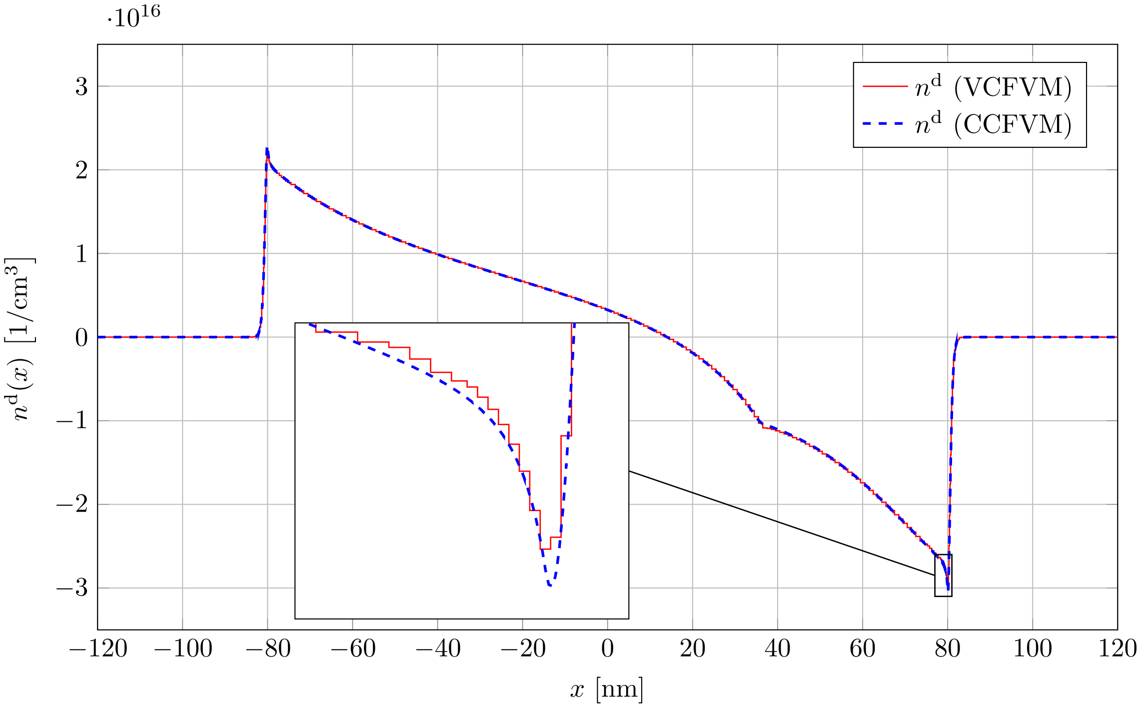

Figure 3.19: Dynamic electron density for both the VCFVM and the CCFVM.

Next, to compare both reconstruction methods, in Figure 3.19 only the dynamic part of the solution is shown. Overall, both methods yield very similar results, however, due to the piecewise constant reconstruction, the VCFVM solution is much more jagged. It is important to note, that even though the solution for the CCFVM appears to be perfectly continuous (in contrast to the VCFVM), this is in fact not the case. At each cell interface a very small discontinuity persists, which, due to its size, is not visible in the graph.

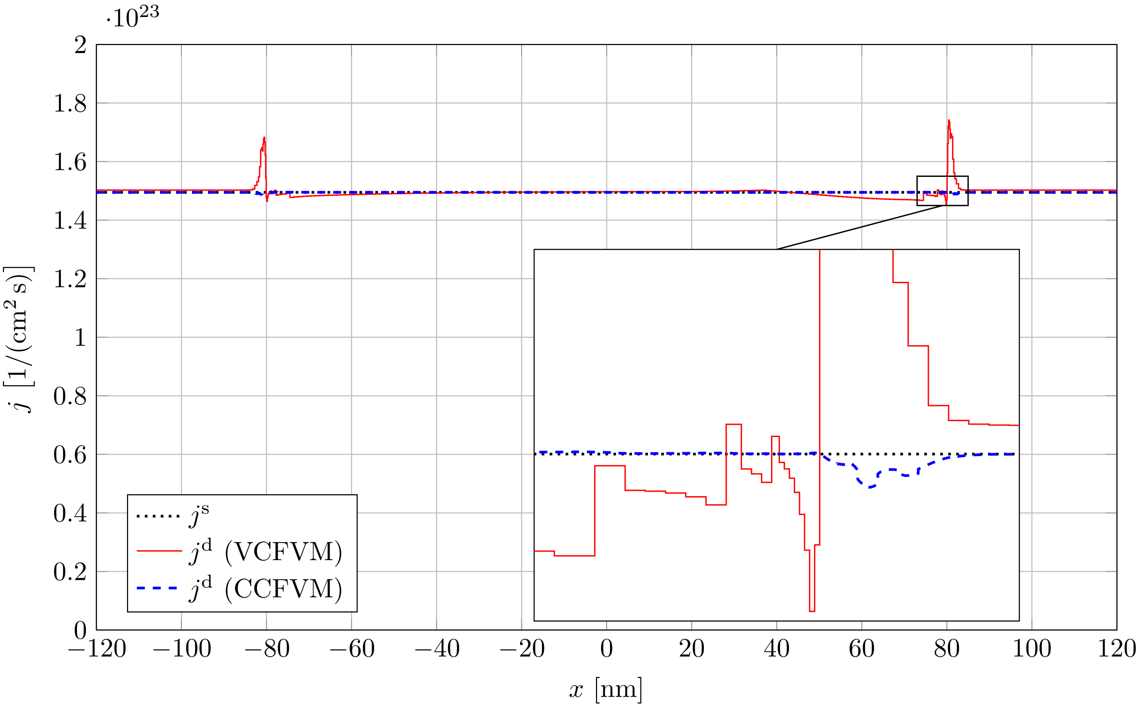

Figure 3.20: Electron current density for the stationary and dynamic system.

In Figure 3.20 the corresponding current density is shown, where j^{d} and j^{s} can be compared directly, because the equilibrium current density is zero. Here, the importance of well-balancedness becomes apparent: Under stationary conditions the current density should be constant ($\partial_x j = 0$), however, only the solution to the stationary system reflects that. While j^{s} is perfectly constant, j^{d} shows some artifacts for both the VCFVM and the CCFVM, especially in the transition regions where the doping concentration changes. Compared to the CCFVM, the VCFVM performs much worse, with artifacts of a much larger magnitude than those of the CCFVM. These artifacts are also found in a much wider area, even though in both cases the same grid was used.

To explain this difference, consider the Riemann solution for the current density. Since in general no analytical solution exists for the CDD model, to keep the explanation simple, the DD model is used as an approximation here (see eq. (3.79)):

$$j^* \approx \frac{1}{2}(j_\mathrm{L} + j_\mathrm{R}) + \frac{c_\mathrm{T}}{2}(n_\mathrm{L} - n_\mathrm{R})\,. \tag{3.157}$$

In addition to the average of the two current densities directly to the left and right of an interface, the difference of the two densities is an important part of the solution for the interface current density. This difference is multiplied by $\frac{c_\mathrm{T}}{2}$, which is a comparatively large value. Even small discontinuities in the density therefore have a large effect on the interface current density. Under stationary conditions it is this interface current density j^* which becomes constant, therefore leading to a discontinuous cell current density for a discontinuous density. Since the VCFVM has larger gaps in the density, unsurprisingly the artifacts in the current density are also much more pronounced. Note that even though the current density is not entirely constant, charge conservation is still guaranteed both for the VCFVM and the CCFVM, since the continuity equation couples only to j^*, which is perfectly constant across the whole device and at each interface it is always the same value for both of the neighboring cells.

3.7 Terminal Equations

To be able to couple the device to an external circuit simulator, it is convenient to define discrete solution variables and associated equations for the external contact potential, as well as the terminal current for each contact. Since the contact potential is given externally, the corresponding equation for the i-th contact is simply given by

$$V_i = V_{\mathrm{appl},i} \,. \tag{3.158}$$

The terminal current on the other hand is given by the integral over the corresponding contact surface of the current density, describing the electrons that enter and leave the device, and, in addition to that, the displacement current which measures the electrons that are charging and discharging the contact itself, but never actually enter the device and thus do not contribute to the current density. The displacement current can be calculated by evaluating the time derivative of the electric flux density, resulting in

$$I_i = \iint \left(\boldsymbol{J} + \frac{\partial}{\partial t} \boldsymbol{D} \right) \cdot \mathrm{d}\boldsymbol{A} \ , \tag{3.159}$$

where $\boldsymbol{J} = e(\boldsymbol{j}_\mathrm{h} - \boldsymbol{j}_\mathrm{e})$ contains both the electron and hole current density. For one dimension and neglecting holes, the total current for a device surface area A through both the source and drain contact is then given by

$$I_\mathrm{S} = \left(-e j_\mathrm{e} + \frac{\partial}{\partial t} D \right) A \quad \text{and} \quad I_\mathrm{D} = \left(+e j_\mathrm{e} - \frac{\partial}{\partial t} D \right) A \,, \tag{3.160}$$

where inflowing currents are counted positive by convention. Depending on the discretization scheme that was used, special care must be taken to avoid losing the property of charge conservation, when evaluating these equations using discrete variables. Charge conservation requires that at all times

$$\sum_i I_i = 0 \,, \tag{3.161}$$

i.e. the Kirchhoff Current Law (KCL) must be fulfilled.

3.7.1 Vertex-Centered Scheme

In the case of the VCFVM, there is no direct access to the electric flux at each contact, since these are located at direct grid points and the electric field is defined only on the adjoint nodes. This makes it difficult to evaluate eq. (3.160) without violating eq. (3.161). Rather than calculating it directly, the Ramo-Shockley theorem [64, 65, 66] is used instead

$$I_i = -\iiint \boldsymbol{\nabla}\nu_i \cdot \boldsymbol{J}\,\mathrm{d}V + \sum_j C_{ij}\frac{\partial}{\partial t}V_j\,, \tag{3.162}$$

where the volume integral runs over the whole device, while $i, j \in \{1, 2, \ldots, N_{\text{contacts}}\}$. The function ν_i is the i-th fundamental solution to the Laplace equation, which is equal to one on the i-th contact, and zero on all other contacts. The capacitance coefficients are given by

$$C_{ij} = \iiint \varepsilon\boldsymbol{\nabla}\nu_i \cdot \boldsymbol{\nabla}\nu_j\,\mathrm{d}V\ . \tag{3.163}$$

Since $\sum_i \nu_i = 1$ everywhere in the device, it is easy to see that the KCL is fulfilled by construction.

For the discrete one-dimensional case, the volume integrals are replaced by weighted sums over all grid cells

$$\iiint (\ldots)\,\mathrm{d}V \rightarrow \sum_{k=1}^{N-1} (\ldots)_{k+1/2}\Delta x_{k+1/2}\,. \tag{3.164}$$

The fundamental solutions are calculated by reusing the PE matrix, where $\nu_{i,k}$ is then the discrete value of ν_i at the k-th vertex. The discrete gradient at an adjoint point is given by

$$(\boldsymbol{\nabla}\nu_i)_{k+1/2} \rightarrow \frac{\nu_{i,k+1} - \nu_{i,k}}{\Delta x_{k+1/2}}\,. \tag{3.165}$$

The capacitance matrix is then

$$C_{ij} = \sum_{k=1}^{N-1} \frac{\varepsilon_{k+1/2}}{\Delta x_{k+1/2}}(\nu_{i,k+1} - \nu_{i,k})(\nu_{j,k+1} - \nu_{j,k})\,, \tag{3.166}$$

and finally, the terminal current is

$$I_i = -\sum_{k=1}^{N-1} (\nu_{i,k+1} - \nu_{i,k}) J_{k+1/2} + \sum_j C_{ij} \frac{\partial}{\partial t} V_j \,. \tag{3.167}$$

3.7.2 Cell-Centered Scheme

As opposed to the VCFVM, for the CCFVM the electric flux density on the cell surfaces is given by discrete solution variables, which means that eq. (3.160) can be evaluated directly at each contact.

To prove the KCL in this case, the general three-dimensional case is considered here, where the device is split into three-dimensional cells. The discrete terminal current can then be written as the sum

$$I_i = \sum_{j \in \mathcal{C}_i} s_j A_j \big(\overline{J}_j + \partial_t \overline{D}_j\big) \,, \tag{3.168}$$

where $\mathcal{C}_i$ denotes the set of cell surfaces belonging to the i-th contact, and A_j is the surface of the j-th cell face. $\overline{J}_j$ and $\overline{D}_j$ are the normal components of the average current and electric flux density on each surface, respectively. The sign $s_j = \pm 1$ is chosen such that inflowing currents are counted positively.

Summing over all terminal currents yields

$$\sum_i I_i = \sum_i \sum_{j \in \mathcal{C}_i} s_j A_j \big(\overline{J}_j + \partial_t \overline{D}_j\big) = \sum_{j \in \mathcal{C}} s_j A_j \big(\overline{J}_j + \partial_t \overline{D}_j\big) \,, \tag{3.169}$$

where $\mathcal{C} = \bigcup_i \mathcal{C}_i$ is the union of all contacted cell faces. Since both the current density and the electric flux density vanish on all uncontacted boundary faces, i.e.

$$\overline{J}_j = 0 \quad \text{and} \quad \overline{D}_j = 0 \quad \text{for} \quad j \in \mathcal{B} \setminus \mathcal{C} \,, \tag{3.170}$$

where $\mathcal{B}$ is the set of all boundary faces, the sum can be extended to

$$\sum_i I_i = \sum_{j \in \mathcal{B}} s_j A_j \big(\overline{J}_j + \partial_t \overline{D}_j\big) \,. \tag{3.171}$$

Assuming the PE was discretized properly, the sum over the electric fluxes can then be expressed in terms of the charge density in each cell

$$\sum_{j\in\mathcal{B}} s_j A_j \overline{D}_j = -\sum_{j\in\mathcal{D}} \Omega_j \overline{\varrho}_j \tag{3.172}$$

where $\mathcal{D}$ is the set of all device cells, and Ω_j is the cell volume. The time derivative is then

$$\sum_{j\in\mathcal{B}} s_j A_j \partial_t \overline{D}_j = -\sum_{j\in\mathcal{D}} \Omega_j \partial_t \overline{\varrho}_j = -\sum_{j\in\mathcal{B}} s_j A_j \overline{J}_j \,, \tag{3.173}$$

where the discrete continuity equation $\Omega_j \partial_t \varrho_j - \sum_k s_k A_k \overline{J}_k = 0$ was used. The index k runs over all surfaces of cell j. The current densities on the inner faces then cancel each other out, as there is only a single current density defined per face, i.e. the current flowing through a face out of one cell, equals the current flowing into the neighboring cell which shares the face. The sum over all currents is therefore

$$\sum_i I_i = 0 \,, \tag{3.174}$$

and the KCL is fulfilled.

3.7.3 Stationary Terminal Current

In Figure 3.21 the stationary output characteristic for the N^+-N-N^+ device is shown for both the DD and CDD model using the CCFVM. For the DD model, the current increases superlinearly with the voltage and does not saturate due to the punch through effect. The CDD model gives very similar results at small voltages, as expected. Only for voltages close to the maximal allowed value of $V_{\mathrm{DS}} = 0.148\,\mathrm{V}$, a slight deviation due to the convective term can be seen. As shown before, higher voltages would lead to a discontinuous solution and can therefore not be simulated with this approach.

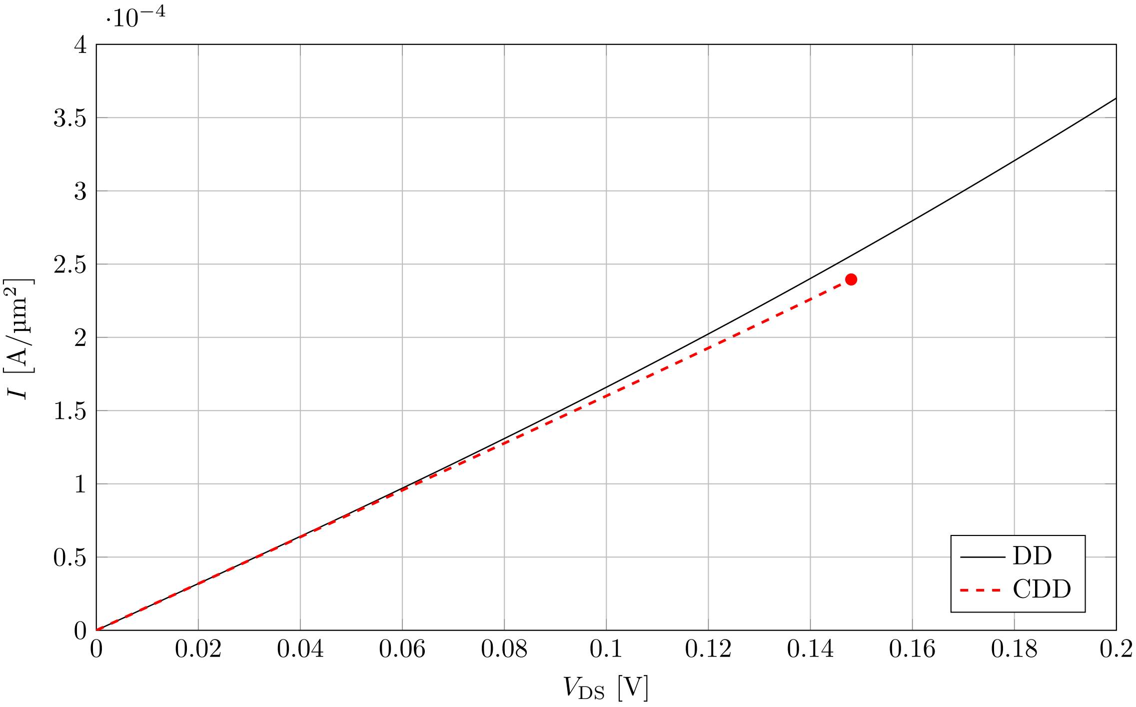

Figure 3.21: Stationary current over voltage for the N$^+$-N-N$^+$ device for both the DD and CDD model.

3.8 Small-Signal Analysis

Including the terminal voltage and current equations, the complete discrete system can be written in the form

$$\mathbf{D}\frac{\partial}{\partial t}\boldsymbol{u} + \boldsymbol{f}(\boldsymbol{u}) = \boldsymbol{0}\,, \tag{3.175}$$

where $\boldsymbol{u}$ contains all of the discrete solution variables, $\mathbf{D}$ is a constant matrix, and $\boldsymbol{f}(\boldsymbol{u})$ is a nonlinear function.

To analyze the small-signal behavior of the system, the equations are linearized around a stationary state, by assuming a harmonic time dependence for all variables

$$\boldsymbol{u} = \boldsymbol{u}_0 + \mathrm{Re}\{\underline{\boldsymbol{u}}\exp(\underline{s}t)\}\,, \tag{3.176}$$

where $\underline{s} = \sigma + j\omega$ is a complex frequency. The small-signal phasor $\underline{\boldsymbol{u}}$ is considered to be small in magnitude compared to the stationary value $\boldsymbol{u}_0$. The linearized equation system is then given by

$$\underline{s}\mathbf{D}\underline{\boldsymbol{u}} + \mathcal{J}\{\boldsymbol{f},\boldsymbol{u}\}\Big|_{\boldsymbol{u}_0}\underline{\boldsymbol{u}} = \boldsymbol{0}\,, \tag{3.177}$$

where the application of the real part operator was dropped.

3.8.1 Admittance

To calculate the small-signal admittance parameters, the terminal voltage equations in eq. (3.177) are replaced by

$$\underline{V}_i = \delta_{ij}\,, \tag{3.178}$$

with the Kronecker delta δ_{ij}, assuming that the j-th contact is analyzed. Since this does not have a physical unit, all results will be normalized to the corresponding voltage, e.g. instead of the actual terminal currents, the admittance parameters $\underline{Y}_{ij} = \frac{\underline{I}_i}{\underline{V}_j}$ will be received.

The modified equation system then contains a right-hand side

$$\left(\underline{s}\mathbf{D} + \mathcal{J}\{\boldsymbol{f},\boldsymbol{u}\}\Big|_{\boldsymbol{u}_0}\right)\underline{\boldsymbol{u}}_j = \boldsymbol{b}_j\,, \tag{3.179}$$

which is given by the Kronecker delta for the terminal voltage equations, and is zero everywhere else. For a given frequency, this system can be solved to yield the small-signal quantities $\underline{\boldsymbol{u}}_j$ for a sinusoidal voltage source at the j-th contact.

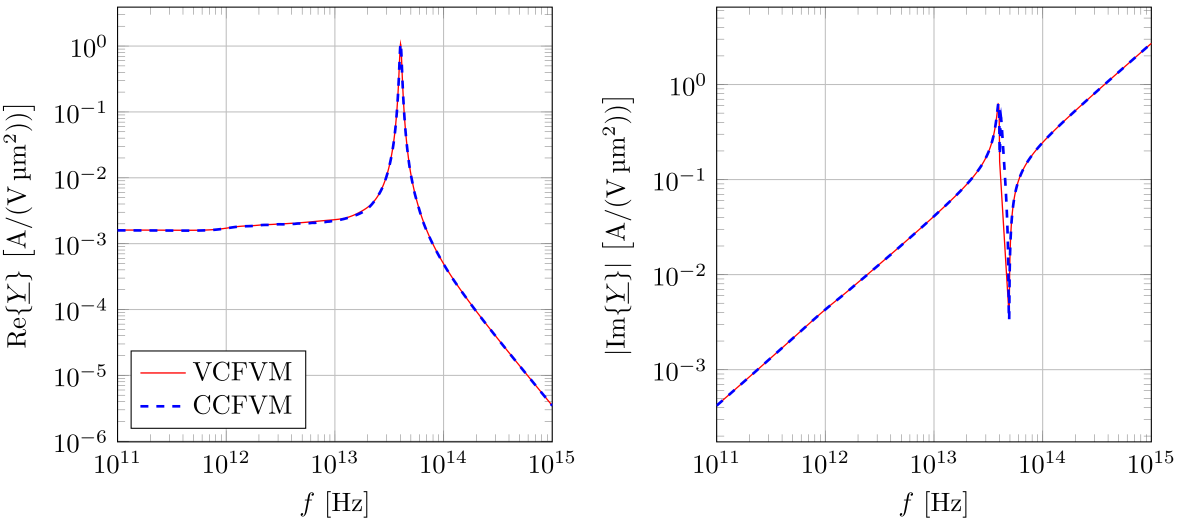

(a) Real part of $\underline{Y}$.

(b) Absolute value of $\mathrm{Im}\{\underline{Y}\}$.

Figure 3.22: Small-Signal admittance at equilibrium for the one-dimensional N$^+$-N-N$^+$ device.

Using the same N$^+$-N-N$^+$ device as before, in Figure 3.22 the small-signal parameters $\underline{Y} = \frac{\underline{I}}{\underline{V}}$ are plotted over a real-valued frequency $f = \frac{\omega}{2\pi}$ with $\sigma = 0$. The applied DC voltage is set to zero (equilibrium conditions). As expected, $\mathrm{Re}\{\underline{Y}\}$ is greater than zero for the whole range of frequencies, implying that the device is asymptotically stable at equilibrium. Both the VCFVM and the CCFVM deliver similar results, even though the VCFVM should have a larger dampening effect at high frequencies, due to its first-order piecewise constant reconstruction [2], which is not visible for this device. There is only a single resonance at about 40 THz, which is closely related to the length of the highly doped contact regions, and therefore of no special interest. At even higher frequencies, the real part of $\underline{Y}$ drops off quickly with $\mathrm{Re}\{\underline{Y}\} \propto \frac{1}{f^2}$.

3.8.2 Eigenvalues

Equation (3.177) has the form of a generalized eigenvalue problem. Because the PE and the terminal voltage equations do not contain a time derivative, the matrix $\mathbf{D}$ is not invertible. To simplify the calculation, these equations can be eliminated leading to a regular eigenvalue problem. For this purpose, the rows and columns of the system are permuted, such that the equations (and the corresponding variables), that are to be eliminated, are located in the upper rows of the system. In block form the system then reads

$$\underline{s}\begin{pmatrix}\mathbf{0} & \mathbf{0}\\ \mathbf{D}_{21} & \mathbf{D}_{22}\end{pmatrix}\begin{pmatrix}\underline{\boldsymbol{u}}_1\\ \underline{\boldsymbol{u}}_2\end{pmatrix}+\begin{pmatrix}\mathbf{J}_{11} & \mathbf{J}_{12}\\ \mathbf{J}_{21} & \mathbf{J}_{22}\end{pmatrix}\begin{pmatrix}\underline{\boldsymbol{u}}_1\\ \underline{\boldsymbol{u}}_2\end{pmatrix}=\begin{pmatrix}\mathbf{0}\\ \mathbf{0}\end{pmatrix}. \tag{3.180}$$

Next, the variables $\underline{\boldsymbol{u}}_1 = -\mathbf{J}_{11}^{-1}\,\mathbf{J}_{12}\,\underline{\boldsymbol{u}}_2$ are eliminated from the system, leading to

$$\underline{s}\big(\mathbf{D}_{22}-\mathbf{D}_{21}\,\mathbf{J}_{11}^{-1}\,\mathbf{J}_{12}\big)\underline{\boldsymbol{u}}_2+\big(\mathbf{J}_{22}-\mathbf{J}_{21}\,\mathbf{J}_{11}^{-1}\,\mathbf{J}_{12}\big)\underline{\boldsymbol{u}}_2=0\,. \tag{3.181}$$

This constitutes a regular eigenvalue problem

$$\mathbf{M}\underline{\boldsymbol{u}}_2=\underline{s}\,\underline{\boldsymbol{u}}_2\,, \tag{3.182}$$

with the dense matrix

$$\mathbf{M}=-\big(\mathbf{D}_{22}-\mathbf{D}_{21}\,\mathbf{J}_{11}^{-1}\,\mathbf{J}_{12}\big)^{-1}\big(\mathbf{J}_{22}-\mathbf{J}_{21}\,\mathbf{J}_{11}^{-1}\,\mathbf{J}_{12}\big)\,. \tag{3.183}$$

The eigenvalues $\underline{s}$ then correspond to the poles of $\underline{Y}$ in the complex plane. Since the terminal voltage equations were not changed, this has the effect of fixing their small-signal values to zero. In place of the voltage, there is also the possibility to fix the drain current instead ($\underline{I}_\mathrm{D} = 0$), which corresponds to the boundary conditions used by Dyakonov and Shur. The eigenvalues of such a modified system then coincide with the zeros of $\underline{Y}$.

In Figure 3.23 the eigenvalues for the N$^+$-N-N$^+$ device at equilibrium are plotted in their entirety. All of the eigenvalues have a negative real part, which again shows that the device is stable at equilibrium. The poles at $f \approx \pm 40\,\mathrm{THz}$ and $\mathrm{Re}\{\underline{s}\} \approx 0$ correspond to the peak which is visible in Figure 3.22. On the other hand, most of the eigenvalues are damped to such an extent, that they are essentially irrelevant and can be ignored.

In Figure 3.24 both the poles and the zeros of $\underline{Y}$ are shown for a small region close to the origin. Additionally, $\underline{Y}$ is calculated in that region and its complex phase plotted in the background. Note how at each zero the phase changes in opposite rotational direction compared to a pole.

The real part of the poles reveals some more information. First of all, there is a pole at zero frequency with a growth factor of $\sigma = -10/\mathrm{ps}$, which is equal to the inverse of the scattering time $\tau = 0.1\,\mathrm{ps}$. Additionally, all other poles (and most zeros) visible in

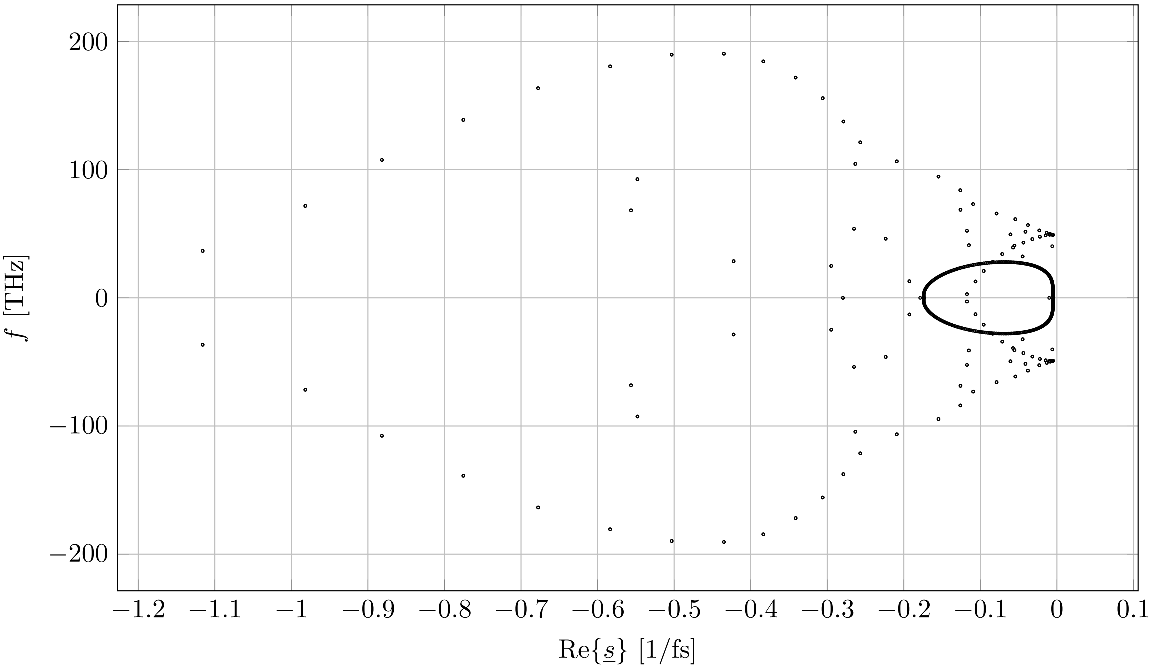

Figure 3.23: Eigenvalues for the CCFVM at equilibrium for the N$^+$-N-N$^+$ device.

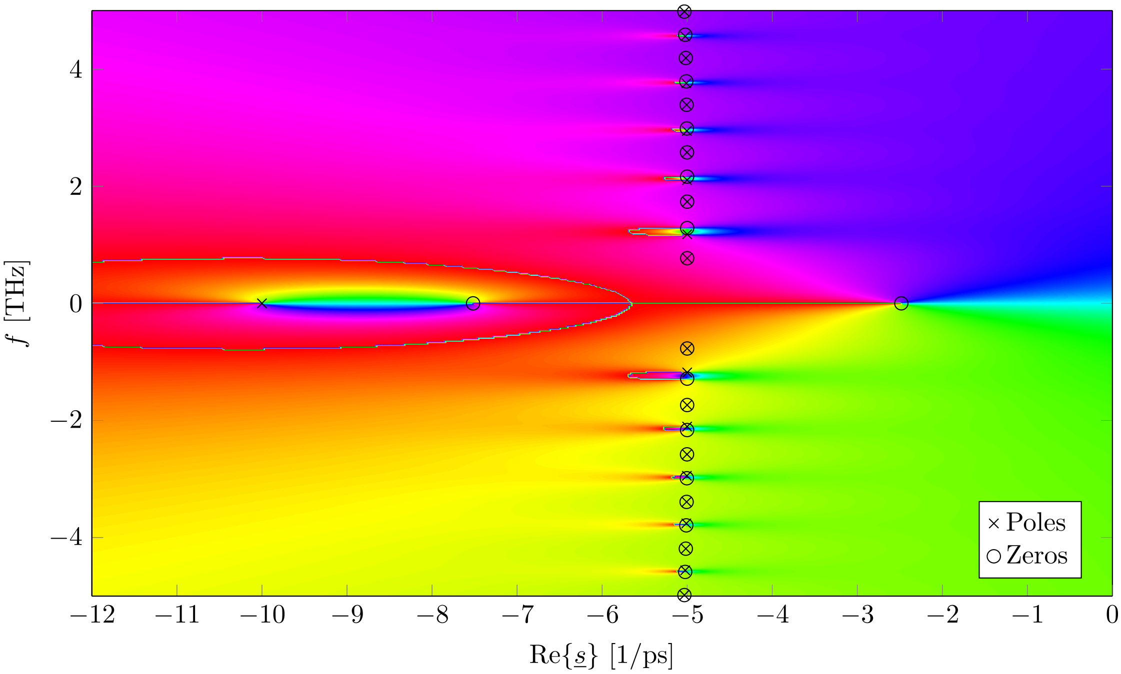

Figure 3.24: Poles, zeros and phase of $\underline{Y}$ at equilibrium close to the origin.

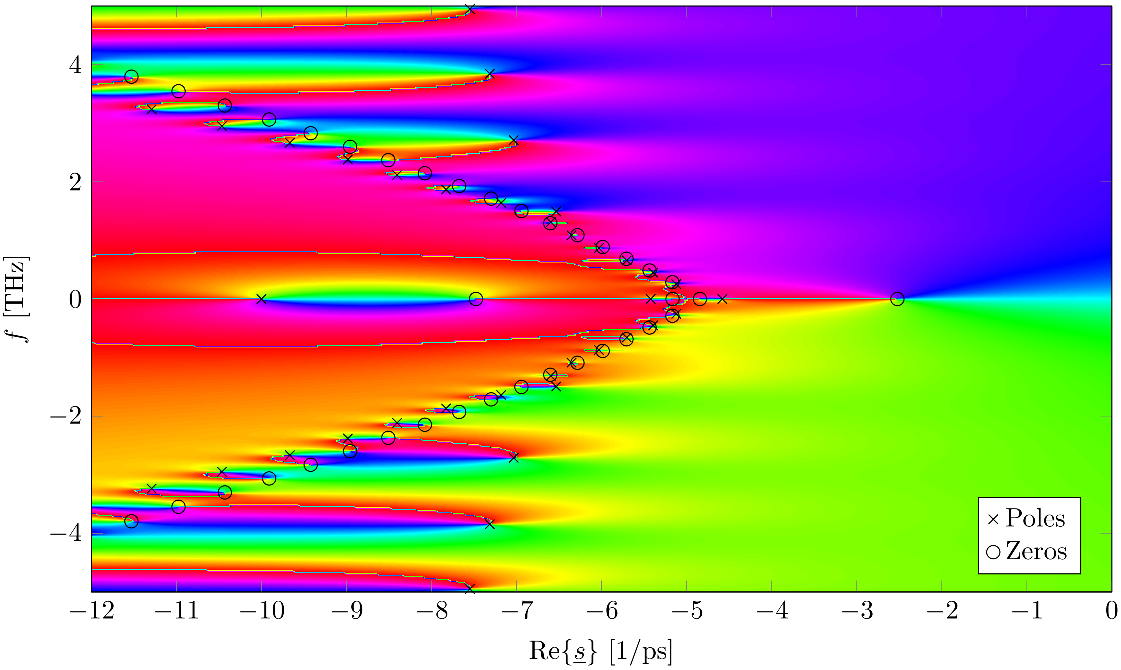

Figure 3.25: Poles, zeros and phase of $\underline{Y}$ for $V_{\mathrm{DS}} = 0.148\,\mathrm{V}$.

this figure have a real part of $\sigma \approx -\frac{1}{2\tau} = -5/\mathrm{ps}$.

In Figure 3.25 a DC voltage of $V_{\mathrm{DS}} = 0.148\,\mathrm{V}$ was applied. While most of the poles and zeros change their positions quite drastically, they still remain in the left half-plane ($\sigma < 0$), therefore the system is still stable.

4 Two-Dimensional Device Simulation

In this chapter, the methods developed for the one-dimensional case are adjusted and generalized to two dimensions. This is in general a non-trivial task, and even impossible for certain parts, e.g. the strategy to solve the stationary transport model with an ODE solver can not be adapted to more than one dimension.

The first part of this chapter focuses only on the extension of the PE to two dimensions, while the transport model is still solved only in one dimension. Only in the second part the fully two-dimensional case is considered. Results are given for two different devices, first a double-gate MOSFET, which can be described using only one-dimensional transport, and later a SOI device including two-dimensional transport.

4.1 Two-Dimensional Grid

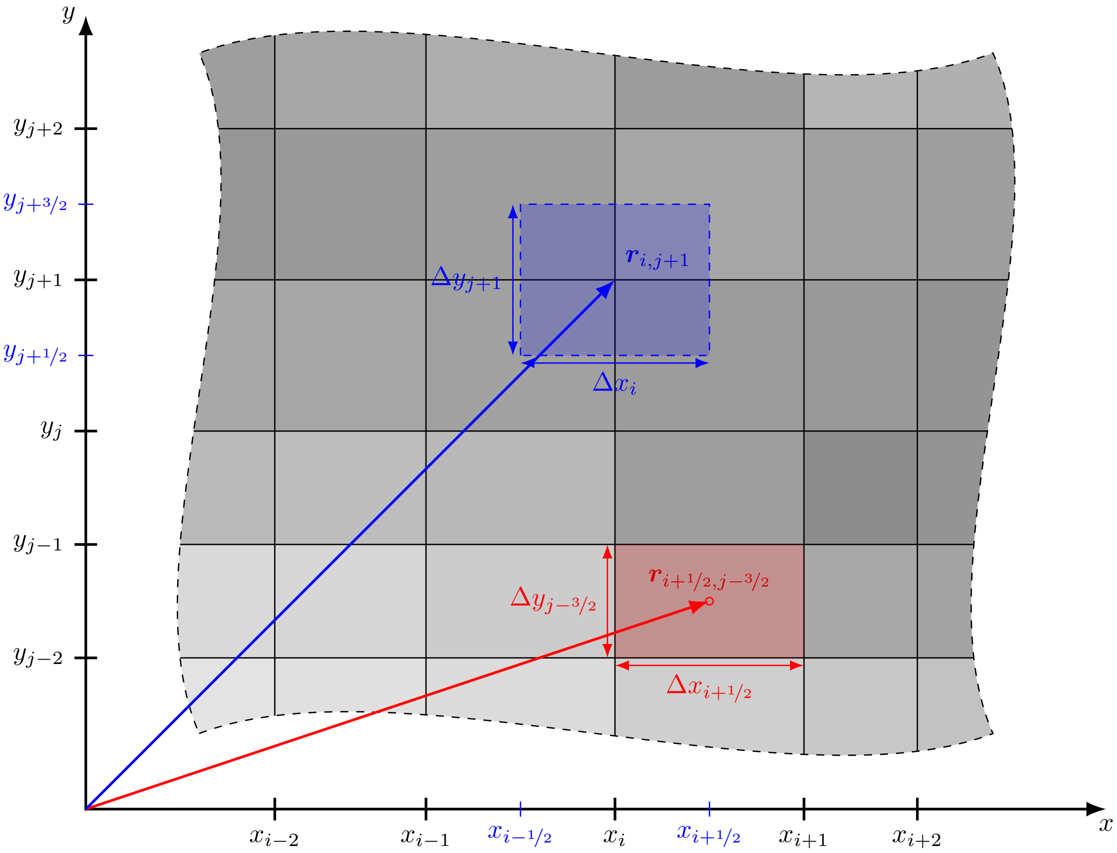

Figure 4.1: Exemplified two-dimensional tensor grid with a highlighted direct (red) and adjoint (blue) cell, where the variously shaded areas indicate some position dependent material constant.

As opposed to the one-dimensional case, in two dimensions many different types of grids can be used to split the solution domain into tiles, e.g. unstructured triangular grids. For simplicity reasons, only rectangular devices are considered in this work, and a simple and natural way to discretize such a device is by using a two-dimensional tensor grid, i.e. the tensor product of two one-dimensional grids. The grid nodes are then given by

$$\boldsymbol{r}_{i,j} = \begin{pmatrix} x_i \\ y_j \end{pmatrix} , \tag{4.1}$$

where $1 \leq i \leq N_x$ and $1 \leq j \leq N_y$ are integers. Like in the one-dimensional case, the resulting grid cells are then numbered by half-integers, where the cell centers are

$$\boldsymbol{r}_{i+1/2,j+1/2} = \begin{pmatrix} \frac{1}{2}(x_i + x_{i+1}) \\ \frac{1}{2}(y_j + y_{j+1}) \end{pmatrix} . \tag{4.2}$$

The cell extents for both directions are

$$\Delta x_{i+1/2} = x_{i+1} - x_i \quad \text{and} \quad \Delta y_{j+1/2} = y_{j+1} - y_j \, . \tag{4.3}$$

Using the cell centers as corners, adjoint cells are again introduced and numbered by whole integers (see Figure 4.1).

Like before, material constants are approximated as piecewise constant on the direct grid cells, for instance

$$\varepsilon(x,y) = \varepsilon_{i+1/2,j+1/2} \quad \text{for} \quad x \in (x_i, x_{i+1}) \quad \text{and} \quad y \in (y_j, y_{j+1}) \, . \tag{4.4}$$

As a two-dimensional device usually consists of some oxide and semiconductor regions, these regions are also modeled at a per cell basis, i.e. the Poisson equation will be solved for all oxide and semiconductor cells, while the transport model will be solved only for the semiconductor cells. Because some devices are best described by a transport layer embedded in a non-conductive environment, the case of mixed dimensionality will also be considered, e.g. solving a two-dimensional Poisson equation together with a one-dimensional transport model. In this case, that layer will be approximated by a single row of cells. For instance, all cells with some y index will belong to the transport layer, and the transport model will only be solved for these cells and only in x-direction.

The contacts in two dimensions are modeled by grouping one or more cell surfaces (lines in 2D) together. As opposed to one-dimensional devices, in addition to contacted boundaries also uncontacted boundaries exist, which require different boundary conditions.

4.2 Two-Dimensional Poisson Equation

In two dimensions the PE is given by

$$\boldsymbol{\nabla} \cdot \boldsymbol{D} = \frac{\partial}{\partial x} D_x(x,y) + \frac{\partial}{\partial y} D_y(x,y) = \varrho(x,y)\,. \tag{4.5}$$

As in the one-dimensional case, two different methods of discretization are shown here: A vertex-centered and a cell-centered finite volume method. Both methods are extensions of the corresponding one-dimensional ones.

4.2.1 Vertex-Centered Finite Volume Method in 2D

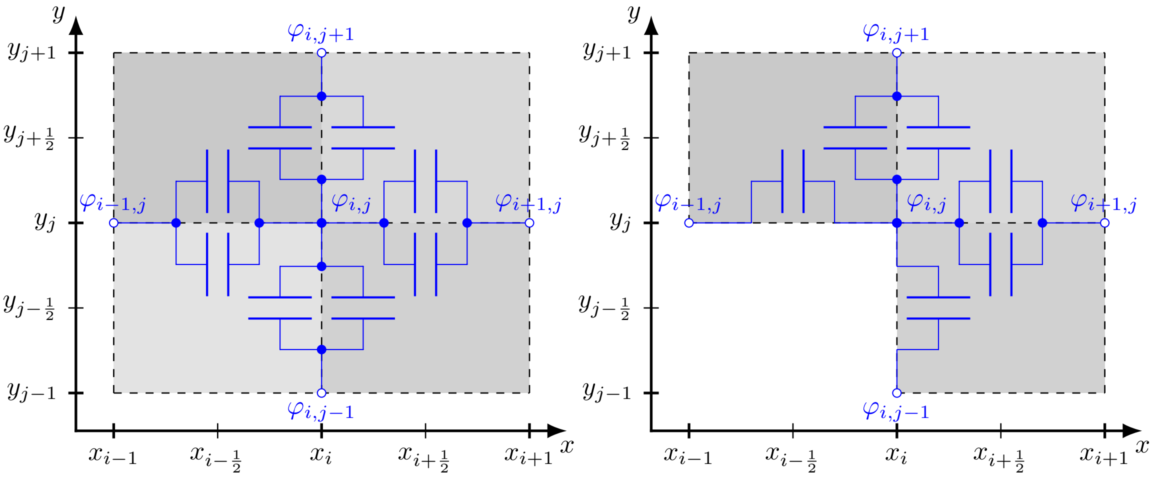

(a) Internal node away from boundaries.

(b) Inverse corner in the lower left.

Figure 4.2: Two different local device geometries surrounding a direct grid node with equivalent circuit diagrams highlighted.

In two dimensions, the integration volume for the VCFVM is again the adjoint cell, which can have different shapes depending on the local device geometry, i.e. boundaries, corners and inverse corners must be considered (see Figure 4.2). Integration over the cell yields

$$A_{i+1/2,j}\overline{D}_{i+1/2,j} - A_{i-1/2,j}\overline{D}_{i-1/2,j} + A_{i,j+1/2}\overline{D}_{i,j+1/2} - A_{i,j-1/2}\overline{D}_{i,j-1/2} = \Omega_{i,j}\overline{\varrho}_{i,j}\,, \tag{4.6}$$

where $A_{i\pm1/2,j}$ and $A_{i,j\pm1/2}$ are the adjoint cell x- and y-surfaces respectively, and $\Omega_{i,j}$ is the adjoint cell volume. $\overline{D}_{i\pm 1/2,j}$ and $\overline{D}_{i,j\pm 1/2}$ are the normal components of the electric flux density averaged over the adjoint cell surfaces, while $\overline{\varrho}_{i,j}$ is the average charge density in the adjoint cell.

Similarly to the one-dimensional case, it is convenient to introduce the capacitance coefficients

$$C^x_{i+1/2,j+1/2} = \frac{1}{2}\frac{\Delta y_{j+1/2}}{\Delta x_{i+1/2}}\,\varepsilon_{i+1/2,j+1/2} \quad \text{and} \quad C^y_{i+1/2,j+1/2} = \frac{1}{2}\frac{\Delta x_{i+1/2}}{\Delta y_{j+1/2}}\,\varepsilon_{i+1/2,j+1/2} \tag{4.7}$$

for each direct grid cell belonging to the solution domain. For cells outside of the solution domain, the coefficients are set to zero. Between two vertices, the capacitances from the two relevant cells are connected in parallel (see the equivalent circuit diagram in Figure 4.2), and can therefore be combined into

$$C_{i+1/2,j} = C^x_{i+1/2,j-1/2} + C^x_{i+1/2,j+1/2} \quad \text{and} \quad C_{i,j+1/2} = C^y_{i-1/2,j+1/2} + C^y_{i+1/2,j+1/2}\,. \tag{4.8}$$

The discrete PE can then be expressed by

$$\begin{aligned} -C_{i-1/2,j}\,\varphi_{i-1,j} - C_{i+1/2,j}\,\varphi_{i+1,j} - C_{i,j-1/2}\,\varphi_{i,j-1} - C_{i,j+1/2}\,\varphi_{i,j+1} \\ + \big(C_{i-1/2,j} + C_{i+1/2,j} + C_{i,j-1/2} + C_{i,j+1/2}\big)\varphi_{i,j} = \Omega_{i,j}\,\overline{\varrho}_{i,j}\,. \end{aligned} \tag{4.9}$$

In more than one dimension, there are two different types of boundaries: Contacted and uncontacted ones. For the uncontacted boundaries, homogeneous Neumann boundary conditions are used. These are automatically fulfilled with this approach, since the corresponding partial cell surfaces are not included in the integration of the electric flux density, which has the same effect as setting the electric flux to zero on these surfaces. For contacted vertices, the corresponding equation is replaced by the discrete Dirichlet boundary condition

$$\varphi_{i,j} = V_k + \phi_{\mathrm{MS},k}\,, \tag{4.10}$$

where k is the index of the associated contact.

Finally, the normal component of the electric field for each adjoint cell surface is approximated by

$$E_{i+1/2,j} = -\frac{\varphi_{i+1,j} - \varphi_{i,j}}{\Delta x_{i+1/2}} \quad \text{and} \quad E_{i,j+1/2} = -\frac{\varphi_{i,j+1} - \varphi_{i,j}}{\Delta y_{j+1/2}}\,. \tag{4.11}$$

4.2.2 Cell-Centered Finite Volume Method in 2D

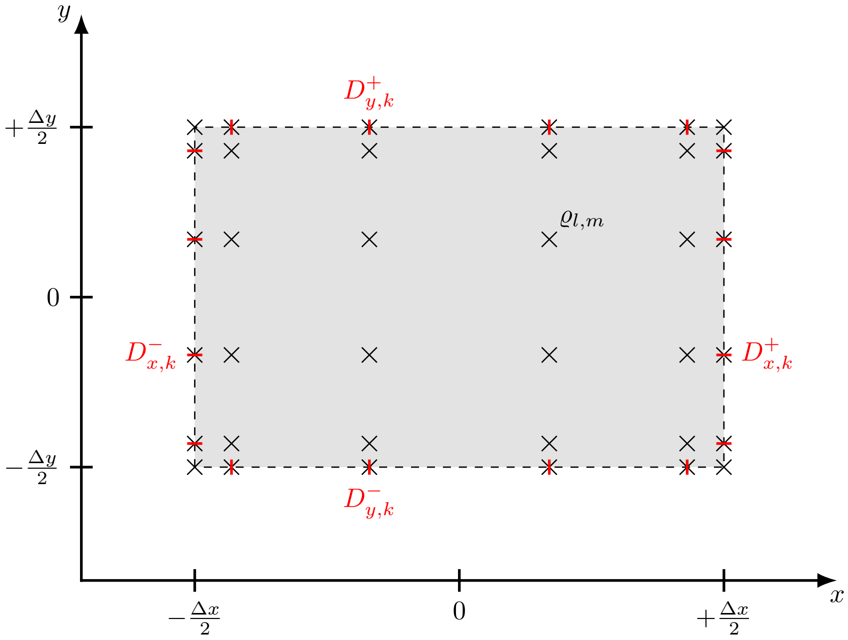

Figure 4.3: Single grid cell for the Cell-Centered Finite Volume Method in 2D.

The cell-centered method in two dimensions involves integrating the PE over a direct grid cell. Since the focus is on a single cell, for the sake of brevity, the cell indices are dropped and the origin is shifted to the cell center. The two-dimensional integration then yields

$$\Delta y\left(\overline{D}_x^+ - \overline{D}_x^-\right) + \Delta x\left(\overline{D}_y^+ - \overline{D}_y^-\right) = \Delta x\,\Delta y\,\overline{\varrho}\,, \tag{4.12}$$

where

$$\overline{D}_x^\pm = \frac{1}{\Delta y}\int_{-\Delta y/2}^{\Delta y/2} D_x\left(\pm\frac{\Delta x}{2}, y\right)\mathrm{d}y \quad \text{and} \quad \overline{D}_y^\pm = \frac{1}{\Delta x}\int_{-\Delta x/2}^{\Delta x/2} D_y\left(x, \pm\frac{\Delta y}{2}\right)\mathrm{d}x \tag{4.13}$$

are the normal components of the electric flux density averaged over the four cell surfaces. The average charge density is given by

$$\overline{\varrho} = \frac{1}{\Delta x\,\Delta y}\int_{-\Delta y/2}^{\Delta y/2}\int_{-\Delta x/2}^{\Delta x/2} \varrho(x,y)\,\mathrm{d}x\,\mathrm{d}y\;. \tag{4.14}$$

The integrals are approximated using the Gauss-Legendre quadrature

$$\overline{D}_x^{\pm} \approx \frac{1}{2}\sum_{k=1}^{N_\mathrm{G}} w_k\, D_{x,k}^{\pm}\,, \quad \overline{D}_y^{\pm} \approx \frac{1}{2}\sum_{k=1}^{N_\mathrm{G}} w_k\, D_{y,k}^{\pm} \quad \text{and} \quad \overline{\varrho} \approx \frac{1}{4}\sum_{l=0}^{N_\mathrm{G}+1}\sum_{m=0}^{N_\mathrm{G}+1} w_l\, w_m\, \varrho_{l,m}\,, \tag{4.15}$$

to which end the discrete values $D_{x,k}^{\pm} = D_x\big(\pm\frac{\Delta x}{2}, \frac{\Delta y}{2}\xi_k\big)$, $D_{y,k}^{\pm} = D_y\big(\frac{\Delta x}{2}\xi_k, \pm\frac{\Delta y}{2}\big)$ and $\varrho_{l,m} = \varrho\big(\frac{\Delta x}{2}\xi_l, \frac{\Delta y}{2}\xi_m\big)$ have been introduced (see Figure 4.3). The index k runs from 1 to N_G, while the two charge density indices l and m are extended to run from 0 to $N_\mathrm{G}+1$, to include the surface values as well. Note, however, that the weights $w_0 = w_{N_\mathrm{G}+1} = 0$ vanish, which is why they do not actually contribute to the value of the integral and are just included to get a more accurate interpolation polynomial.

Similar to the one-dimensional case, the idea is to solve the Neumann problem for a single cell, while using an interpolation polynomial to get a continuous expression for the charge density in the cell. In addition to that, the electric flux density on each cell surface is also expressed by an interpolation polynomial, giving a high resolution boundary condition. The solution variables are the average cell potential and the electric fluxes at the Gauss-Legendre points on each surface. The corresponding cell equation is eq. (4.12), while for the face equations, continuity of the potential across the interface at each Gauss-Legendre point on the face is demanded

$$\begin{aligned}
\varphi_{i+1/2,j+1/2}\left(x_i, y_{j+1/2} + \frac{\Delta y}{2}\xi_k\right) &\overset{!}{=} \varphi_{i-1/2,j+1/2}\left(x_i, y_{j+1/2} + \frac{\Delta y}{2}\xi_k\right)\\
\varphi_{i+1/2,j+1/2}\left(x_{i+1/2} + \frac{\Delta x}{2}\xi_k, y_j\right) &\overset{!}{=} \varphi_{i+1/2,j-1/2}\left(x_{i+1/2} + \frac{\Delta x}{2}\xi_k, y_j\right).
\end{aligned} \tag{4.16}$$

The resulting solution satisfies $\operatorname{Div}\boldsymbol{D} = 0$ everywhere, i.e. the normal component of the electric flux density is continuous across the interfaces. However, $\operatorname{Rot}\boldsymbol{E} = \boldsymbol{0}$ is in general only approximately fulfilled, i.e. the tangential components of the electric field are not guaranteed to be continuous. For that to hold, the potential would need to be continuous on the whole interface, not just on isolated points, which would require $N_\mathrm{G} \to \infty$.

In the following sections, the solution procedure is explained in more detail.

4.2.2.1 Exact Solution for a single Cell

The two-dimensional interpolation polynomial for ϱ is given in the Newton basis as

$$\varrho(x,y) = \sum_{r_{x,y}=0}^{N_\mathrm{G}+1} \sum_{s_{x,y}=0}^{N_\mathrm{G}+1} a_{r_x r_y s_x s_y} \prod_{t_x=0}^{r_x-1} (x - x_{t_x}) \prod_{t_y=0}^{r_y-1} \big(y - y_{t_y}\big) \varrho_{s_x s_y} \,, \tag{4.17}$$

with the interpolation coefficients $a_{r_x r_y s_x s_y}$. Analogously, the electric flux interpolation polynomials are

$$D_x^\pm(y) = \sum_{r=1}^{N_\mathrm{G}} \sum_{s=1}^{N_\mathrm{G}} b_{rs}^y \prod_{t=1}^{r-1} (y - y_t) D_{x,s}^\pm \tag{4.18}$$

and

$$D_y^\pm(x) = \sum_{r=1}^{N_\mathrm{G}} \sum_{s=1}^{N_\mathrm{G}} b_{rs}^x \prod_{t=1}^{r-1} (x - x_t) D_{y,s}^\pm \,, \tag{4.19}$$

where in contrast to the charge density, the interval end points (in this case the grid vertices) are not included in the interpolation (see Figure 4.3).

Since the permittivity is a cell-wise constant, the PE for a single cell can be written as

$$\nabla^2 \varphi(x,y) = -\frac{\varrho(x,y)}{\varepsilon} \,, \tag{4.20}$$

with the Neumann boundary conditions

$$\begin{aligned} \frac{\partial}{\partial x}\varphi(x,y)\bigg|_{x=\pm\Delta x/2} &= -\frac{D_x^\pm(y)}{\varepsilon} \\ \frac{\partial}{\partial y}\varphi(x,y)\bigg|_{y=\pm\Delta y/2} &= -\frac{D_y^\pm(x)}{\varepsilon} \,. \end{aligned} \tag{4.21}$$

Additionally, the condition

$$\frac{1}{\Delta x\,\Delta y} \int_{-\Delta y/2}^{\Delta y/2} \int_{-\Delta x/2}^{\Delta x/2} \varphi(x,y)\,\mathrm{d}x\,\mathrm{d}y \overset{!}{=} \overline{\varphi} \tag{4.22}$$

must be fulfilled, which completes the Neumann problem. It is well-posed, as long as eq. (4.12) is satisfied.

Solving the Neumann problem for a two-dimensional rectangular cell is a bit more involved than in the one-dimensional case. Like before, the charge density is split into an average and a fluctuation

$$\varrho(x,y) = \overline{\varrho} + \widetilde{\varrho}(x,y)\,, \tag{4.23}$$

with

$$\widetilde{\varrho}(x,y) = \sum_{r_{x,y}=0}^{N_\mathrm{G}+1} \sum_{s_{x,y}=0}^{N_\mathrm{G}+1} a_{r_x r_y s_x s_y} \prod_{t_x=0}^{r_x-1} (x - x_{t_x}) \prod_{t_y=0}^{r_y-1} \big(y - y_{t_y}\big) \big(\varrho_{s_x s_y} - \overline{\varrho}\big)\,. \tag{4.24}$$

Additionally, the same is done to the electric flux density on each surface

$$D_x^\pm(y) = \overline{D}_x^\pm + \widetilde{D}_x^\pm(y) \quad \text{and} \quad D_y^\pm(x) = \overline{D}_y^\pm + \widetilde{D}_y^\pm(x)\,, \tag{4.25}$$

where

$$\widetilde{D}_x^\pm(y) = \sum_{r=1}^{N_\mathrm{G}} \sum_{s=1}^{N_\mathrm{G}} b_{rs}^y \prod_{t=1}^{r-1} (y - y_t) \Big(D_{x,s}^\pm - \overline{D}_x^\pm\Big) \tag{4.26}$$

and

$$\widetilde{D}_y^\pm(x) = \sum_{r=1}^{N_\mathrm{G}} \sum_{s=1}^{N_\mathrm{G}} b_{rs}^x \prod_{t=1}^{r-1} (x - x_t) \Big(D_{y,s}^\pm - \overline{D}_y^\pm\Big)\,. \tag{4.27}$$

The potential is then split into six parts, one for the average, one for the density fluctuation and four for the boundary fluctuations, which can be done because the PE is linear:

$$\varphi(x,y) = \varphi^\mathrm{a}(x,y) + \widetilde{\varphi}(x,y) + \varphi^{x+}(x,y) + \varphi^{x-}(x,y) + \varphi^{y+}(x,y) + \varphi^{y-}(x,y)\,. \tag{4.28}$$

The corresponding electric field is similarly split

$$\boldsymbol{E}(x,y) = \boldsymbol{E}^\mathrm{a}(x,y) + \widetilde{\boldsymbol{E}}(x,y) + \boldsymbol{E}^{x+}(x,y) + \boldsymbol{E}^{x-}(x,y) + \boldsymbol{E}^{y+}(x,y) + \boldsymbol{E}^{y-}(x,y)\,, \tag{4.29}$$

with $\boldsymbol{E}^\mathrm{a} = -\boldsymbol{\nabla}\varphi^\mathrm{a}$, $\widetilde{\boldsymbol{E}} = -\boldsymbol{\nabla}\widetilde{\varphi}$ and $\boldsymbol{E}^{x,y\pm} = -\boldsymbol{\nabla}\varphi^{x,y\pm}$.

4.2.2.2 Average Contribution

The average contribution $\varphi^{\mathrm{a}}(x,y)$ is calculated by solving a modified Neumann problem, where only averages are considered. The PE in that case is

$$\nabla^2\varphi^{\mathrm{a}}(x,y) = -\frac{\overline{\varrho}}{\varepsilon}\,, \tag{4.30}$$

with the boundary conditions

$$\begin{aligned}\frac{\partial}{\partial x}\varphi^{\mathrm{a}}(x,y)\bigg|_{x=\pm\Delta x/2} &= -\frac{\overline{D}_x^{\pm}}{\varepsilon}\\ \frac{\partial}{\partial y}\varphi^{\mathrm{a}}(x,y)\bigg|_{y=\pm\Delta y/2} &= -\frac{\overline{D}_y^{\pm}}{\varepsilon}\,.\end{aligned} \tag{4.31}$$

The solution is simply given by the quadratic function

$$\begin{aligned}\varphi^{\mathrm{a}}(x,y) = \overline{\varphi} &+ \frac{1}{\varepsilon}\left(\frac{\Delta x}{24} - \frac{x}{2}\left(1+\frac{x}{\Delta x}\right)\right)\overline{D}_x^{+} + \frac{1}{\varepsilon}\left(-\frac{\Delta x}{24} - \frac{x}{2}\left(1-\frac{x}{\Delta x}\right)\right)\overline{D}_x^{-}\\ &+ \frac{1}{\varepsilon}\left(\frac{\Delta y}{24} - \frac{y}{2}\left(1+\frac{y}{\Delta y}\right)\right)\overline{D}_y^{+} + \frac{1}{\varepsilon}\left(-\frac{\Delta y}{24} - \frac{y}{2}\left(1-\frac{y}{\Delta y}\right)\right)\overline{D}_y^{-}\,,\end{aligned} \tag{4.32}$$

where eq. (4.22) is already fulfilled by φ^{a}, resulting in the fact that all the other contributions to the potential should have vanishing averages. Like in the one-dimensional case, this solution depends only indirectly on $\overline{\varrho}$ via eq. (4.12).

The contribution to the electric field is then

$$\begin{aligned}E_x^{\mathrm{a}}(x,y) = -\frac{\partial\varphi^{\mathrm{a}}}{\partial x} &= \frac{1}{\varepsilon}\left(\frac{1}{2}+\frac{x}{\Delta x}\right)\overline{D}_x^{+} + \frac{1}{\varepsilon}\left(\frac{1}{2}-\frac{x}{\Delta x}\right)\overline{D}_x^{-}\\ E_y^{\mathrm{a}}(x,y) = -\frac{\partial\varphi^{\mathrm{a}}}{\partial y} &= \frac{1}{\varepsilon}\left(\frac{1}{2}+\frac{y}{\Delta y}\right)\overline{D}_y^{+} + \frac{1}{\varepsilon}\left(\frac{1}{2}-\frac{y}{\Delta y}\right)\overline{D}_y^{-}\,.\end{aligned} \tag{4.33}$$

4.2.2.3 Charge Density Fluctuation Contribution

The contribution due to the charge density fluctuation is given by the solution to the Neumann problem

$$\nabla^2\widetilde{\varphi}(x,y) = -\frac{\widetilde{\varrho}(x,y)}{\varepsilon}\,, \tag{4.34}$$

with the homogeneous boundary conditions

$$\frac{\partial}{\partial x}\widetilde{\varphi}(x,y)\bigg|_{x=\pm\Delta x/2} = 0 \quad \text{and} \quad \frac{\partial}{\partial y}\widetilde{\varphi}(x,y)\bigg|_{y=\pm\Delta y/2} = 0\,. \tag{4.35}$$

Additionally, the cell average of $\widetilde{\varphi}(x,y)$ must also be zero, as already mentioned in the previous section.

Since an analytical solution does not exist in general, a cosine series expansion is used instead, where the ansatz

$$\widetilde{\varphi}(x,y) = \sum_{n=0}^{\infty}\sum_{m=0}^{\infty} \widetilde{\varphi}_{nm} \cos\!\left(\frac{n\pi}{\Delta x}\left(x+\frac{\Delta x}{2}\right)\right)\cos\!\left(\frac{m\pi}{\Delta y}\left(y+\frac{\Delta y}{2}\right)\right) \tag{4.36}$$

fulfills the boundary conditions by construction. The application of the Laplacian to this ansatz yields

$$\begin{aligned}\nabla^2\widetilde{\varphi}(x,y) = -\sum_{n=0}^{\infty}\sum_{m=0}^{\infty}\widetilde{\varphi}_{nm} \cos\!\left(\frac{n\pi}{\Delta x}\left(x+\frac{\Delta x}{2}\right)\right)\cos\!\left(\frac{m\pi}{\Delta y}\left(y+\frac{\Delta y}{2}\right)\right)\\ \cdot\left(\left(\frac{n\pi}{\Delta x}\right)^2+\left(\frac{m\pi}{\Delta y}\right)^2\right).\end{aligned} \tag{4.37}$$

To derive an expression for $\widetilde{\varphi}_{nm}$, the right-hand side of eq. (4.34) is similarly expanded into a cosine series, such that the method of equating coefficients can be applied:

$$\begin{aligned}\widetilde{\varrho}(x,y) &= \sum_{r_{x,y}=0}^{N_\mathrm{G}+1}\sum_{s_{x,y}=0}^{N_\mathrm{G}+1} a_{r_x r_y s_x s_y}\prod_{t_x=0}^{r_x-1}\left(x-x_{t_x}\right)\prod_{t_y=0}^{r_y-1}\left(y-y_{t_y}\right)\left(\varrho_{s_x s_y}-\overline{\varrho}\right)\\ &\overset{!}{=}\sum_{n=0}^{\infty}\sum_{m=0}^{\infty}\widetilde{\varrho}_{nm}\cos\!\left(\frac{n\pi}{\Delta x}\left(x+\frac{\Delta x}{2}\right)\right)\cos\!\left(\frac{m\pi}{\Delta y}\left(y+\frac{\Delta y}{2}\right)\right),\end{aligned} \tag{4.38}$$

where

$$\widetilde{\varrho}_{nm} = \sum_{r_{x,y}=0}^{N_\mathrm{G}+1}\sum_{s_{x,y}=0}^{N_\mathrm{G}+1} a_{r_x r_y s_x s_y}\, c^{x}_{r_x n}\, c^{y}_{r_y m}\left(\varrho_{s_x s_y}-\overline{\varrho}\right). \tag{4.39}$$

For simplicity, the values

$$c^x_{rn} = \left\{\begin{array}{lll} 1 & \text{for} & n=0 \\ 2 & \text{for} & n>0 \end{array}\right\} \frac{1}{\Delta x} \int_{-\Delta x/2}^{\Delta x/2} \prod_{t=0}^{r-1} (x - x_t) \cos\left(\frac{n\pi}{\Delta x}\left(x + \frac{\Delta x}{2}\right)\right) \mathrm{d}x \quad \text{and}$$

$$c^y_{rn} = \left\{\begin{array}{lll} 1 & \text{for} & n=0 \\ 2 & \text{for} & n>0 \end{array}\right\} \frac{1}{\Delta y} \int_{-\Delta y/2}^{\Delta y/2} \prod_{t=0}^{r-1} (y - y_t) \cos\left(\frac{n\pi}{\Delta y}\left(y + \frac{\Delta y}{2}\right)\right) \mathrm{d}y \tag{4.40}$$

are calculated by numerical integration using the well-known QUADPACK library [67]. Note that $\widetilde{\varrho}_{00} = 0$, since the cell average of the fluctuation vanishes by construction. Equating the coefficients then results in

$$\widetilde{\varphi}_{nm} = \sum_{r_{x,y}=0}^{N_\mathrm{G}+1} \sum_{s_{x,y}=0}^{N_\mathrm{G}+1} \frac{a_{r_x r_y s_x s_y}\, c^x_{r_x n}\, c^y_{r_y m}}{\varepsilon\Big(\big(\frac{n\pi}{\Delta x}\big)^2 + \big(\frac{m\pi}{\Delta y}\big)^2\Big)} \big(\varrho_{s_x s_y} - \overline{\varrho}\big) \tag{4.41}$$

for $n > 0$ and/or $m > 0$. For $n = 0$ and $m = 0$ the value of $\widetilde{\varphi}_{00} = 0$ is chosen such that the condition of a vanishing cell average of $\widetilde{\varphi}(x, y)$ is met.

Finally, the charge density fluctuation contribution can be written as

$$\widetilde{\varphi}(x, y) = \sum_{s_{x,y}=0}^{N_\mathrm{G}+1} d_{s_x s_y}(x, y) \big(\varrho_{s_x s_y} - \overline{\varrho}\big) , \tag{4.42}$$

where

$$\begin{aligned} d_{s_x s_y}(x, y) = \sum_{r_{x,y}=0}^{N_\mathrm{G}+1} \sum_{n=0}^{\infty} \sum_{m=0}^{\infty} a_{r_x r_y s_x s_y}\, c^x_{r_x n}\, c^y_{r_y m} \frac{u_{nm}}{\varepsilon} \\ \cdot \cos\left(\frac{n\pi}{\Delta x}\left(x + \frac{\Delta x}{2}\right)\right) \cos\left(\frac{m\pi}{\Delta y}\left(y + \frac{\Delta y}{2}\right)\right) , \end{aligned} \tag{4.43}$$

with

$$u_{nm} = \begin{cases} 0 & \text{for} \quad n = m = 0 \\ \frac{1}{\left(\frac{n\pi}{\Delta x}\right)^2 + \left(\frac{m\pi}{\Delta y}\right)^2} & \text{else} \end{cases} . \tag{4.44}$$

The infinite series converges rather quickly, and in practice is only evaluated up to $n_\mathrm{max} = m_\mathrm{max} = 2N_\mathrm{G} + 1$.

The contribution to the electric field is given by

$$\widetilde{\boldsymbol{E}}(x,y) = -\sum_{s_{x,y}=0}^{N_{\mathrm{G}}+1} \boldsymbol{\nabla} d_{s_x s_y}(x,y)\big(\varrho_{s_x s_y} - \overline{\varrho}\big)\,. \tag{4.45}$$

4.2.2.4 Boundary Fluctuation Contributions

In addition to the charge density fluctuation, the boundary fluctuations of the electric flux density must be considered. For each boundary, a modified Neumann problem is solved, where at all but one boundary the flux is set to zero. The charge density inside of the cell is also set to zero, since its effects are already completely contained in φ^{a} and $\widetilde{\varphi}$.

Considering for example the boundary at $x = +\frac{\Delta x}{2}$, the Laplace equation

$$\nabla^2 \varphi^{x+}(x,y) = 0\,, \tag{4.46}$$

with

$$\frac{\partial}{\partial x}\varphi^{x+}(x,y)\bigg|_{x=+\Delta x/2} = -\frac{\widetilde{D}_x^{+}(y)}{\varepsilon} \tag{4.47}$$

on the inhomogeneous boundary, and

$$\frac{\partial}{\partial x}\varphi^{x+}(x,y)\bigg|_{x=-\Delta x/2} = 0 \quad \text{and} \quad \frac{\partial}{\partial y}\varphi^{x+}(x,y)\bigg|_{y=\pm\Delta y/2} = 0 \tag{4.48}$$

on the remaining boundaries is solved. Note, that even though one of the boundaries is inhomogeneous and a charge density of zero is considered, the problem is still well-posed, since the average value of the electric flux density on the inhomogeneous boundary is zero by construction (fluctuations have an average of zero).

Similar to the charge density fluctuation, the general idea is to use a series expansion together with the method of equating the coefficients, to get a solution. An ansatz, that fulfills the Laplace equation including all of the homogeneous boundary conditions and also has a vanishing cell average, is

$$\varphi^{x+}(x,y) = \sum_{n=1}^{\infty} \varphi_n^{x+} \cosh\!\left(\frac{n\pi}{\Delta y}\left(x + \frac{\Delta x}{2}\right)\right) \cos\!\left(\frac{n\pi}{\Delta y}\left(y + \frac{\Delta y}{2}\right)\right). \tag{4.49}$$

The coefficients φ_n^{x+} must be chosen such that the remaining inhomogeneous boundary condition eq. (4.47) is also fulfilled. To that end, the normal derivative at the $x = +\frac{\Delta x}{2}$ boundary

$$\frac{\partial}{\partial x}\varphi^{x+}(x,y)\bigg|_{x=+\Delta x/2} = \sum_{n=1}^{\infty} \varphi_n^{x+} \frac{n\pi}{\Delta y} \sinh\!\left(\frac{n\pi\Delta x}{\Delta y}\right) \cos\!\left(\frac{n\pi}{\Delta y}\left(y + \frac{\Delta y}{2}\right)\right) \tag{4.50}$$

is calculated first. Next, the electric flux density fluctuation is expanded into the cosine series

$$\begin{aligned} \widetilde{D}_x^+(y) &= \sum_{r=1}^{N_\mathrm{G}} \sum_{s=1}^{N_\mathrm{G}} b_{rs}^y \prod_{t=1}^{r-1} (y - y_t) \left(D_{x,s}^+ - \overline{D}_x^+\right) \\ &\overset{!}{=} \sum_{n=1}^{\infty} \widetilde{D}_{xn}^+ \cos\!\left(\frac{n\pi}{\Delta y}\left(y + \frac{\Delta y}{2}\right)\right), \end{aligned} \tag{4.51}$$

where the coefficients are given by

$$\begin{aligned} \widetilde{D}_{xn}^+ &= \frac{2}{\Delta y} \int_{-\Delta y/2}^{\Delta y/2} \widetilde{D}_x^+(y) \cos\!\left(\frac{n\pi}{\Delta y}\left(y + \frac{\Delta y}{2}\right)\right) \mathrm{d}y \\ &= \sum_{r=1}^{N_\mathrm{G}} \sum_{s=1}^{N_\mathrm{G}} b_{rs}^y \, \zeta_{rn}^y \left(D_{x,s}^+ - \overline{D}_x^+\right). \end{aligned} \tag{4.52}$$

The quantities

$$\zeta_{rn}^y = \frac{2}{\Delta y} \int_{-\Delta y/2}^{\Delta y/2} \prod_{t=1}^{r-1} (y - y_t) \cos\!\left(\frac{n\pi}{\Delta y}\left(y + \frac{\Delta y}{2}\right)\right) \mathrm{d}y \tag{4.53}$$

differ from c_{rn}^y in that the case $n = 0$ is excluded, and that the product in the integrand starts from $t = 1$ instead of $t = 0$. They are again calculated by numerical integration.

Inserting eqs. (4.50) and (4.51) into eq. (4.47) and equating the coefficients then yields

$$\varphi_n^{x+} = -\frac{\widetilde{D}_{xn}^+}{\varepsilon \frac{n\pi}{\Delta y} \sinh\!\left(\frac{n\pi\Delta x}{\Delta y}\right)}. \tag{4.54}$$

Finally, the contribution by that particular boundary is given by

$$\varphi^{x+}(x,y) = \sum_{s=1}^{N_\mathrm{G}} e_s^{x+}(x,y)\Big(D_{x,s}^{+} - \overline{D}_x^{+}\Big)\,, \tag{4.55}$$

with

$$e_s^{x+}(x,y) = -\sum_{r=1}^{N_\mathrm{G}}\sum_{n=1}^{\infty} \frac{b_{rs}^{y}\zeta_{rn}^{y}}{\varepsilon\frac{n\pi}{\Delta y}\sinh\!\Big(\frac{n\pi\Delta x}{\Delta y}\Big)} \cosh\!\bigg(\frac{n\pi}{\Delta y}\bigg(x+\frac{\Delta x}{2}\bigg)\bigg)\cos\!\bigg(\frac{n\pi}{\Delta y}\bigg(y+\frac{\Delta y}{2}\bigg)\bigg)\,. \tag{4.56}$$

The remaining boundaries are treated analogously, resulting in

$$\begin{aligned}\varphi^{x\pm}(x,y) &= \sum_{s=1}^{N_\mathrm{G}} e_s^{x\pm}(x,y)\Big(D_{x,s}^{\pm} - \overline{D}_x^{\pm}\Big)\\ \varphi^{y\pm}(x,y) &= \sum_{s=1}^{N_\mathrm{G}} e_s^{y\pm}(x,y)\Big(D_{y,s}^{\pm} - \overline{D}_y^{\pm}\Big)\,,\end{aligned} \tag{4.57}$$

with

$$\begin{aligned}e_s^{x\pm}(x,y) &= \mp\sum_{r=1}^{N_\mathrm{G}}\sum_{n=1}^{\infty} \frac{b_{rs}^{y}\zeta_{rn}^{y}}{\varepsilon\frac{n\pi}{\Delta y}\sinh\!\Big(\frac{n\pi\Delta x}{\Delta y}\Big)} \cosh\!\bigg(\frac{n\pi}{\Delta y}\bigg(x\pm\frac{\Delta x}{2}\bigg)\bigg)\cos\!\bigg(\frac{n\pi}{\Delta y}\bigg(y+\frac{\Delta y}{2}\bigg)\bigg)\\ e_s^{y\pm}(x,y) &= \mp\sum_{r=1}^{N_\mathrm{G}}\sum_{n=1}^{\infty} \frac{b_{rs}^{x}\zeta_{rn}^{x}}{\varepsilon\frac{n\pi}{\Delta x}\sinh\!\Big(\frac{n\pi\Delta y}{\Delta x}\Big)} \cos\!\bigg(\frac{n\pi}{\Delta x}\bigg(x+\frac{\Delta x}{2}\bigg)\bigg)\cosh\!\bigg(\frac{n\pi}{\Delta x}\bigg(y\pm\frac{\Delta y}{2}\bigg)\bigg)\,.\end{aligned} \tag{4.58}$$

The contributions to the electric field by the boundary fluctuations are then

$$\begin{aligned}\boldsymbol{E}^{x\pm}(x,y) &= -\sum_{s=1}^{N_\mathrm{G}} \boldsymbol{\nabla} e_s^{x\pm}(x,y)\Big(D_{x,s}^{\pm} - \overline{D}_x^{\pm}\Big)\\ \boldsymbol{E}^{y\pm}(x,y) &= -\sum_{s=1}^{N_\mathrm{G}} \boldsymbol{\nabla} e_s^{y\pm}(x,y)\Big(D_{y,s}^{\pm} - \overline{D}_y^{\pm}\Big)\,.\end{aligned} \tag{4.59}$$

This concludes the solution procedure in two dimensions, where due to the linearity of the PE, the sum of all contributions fulfills the PE for a single grid cell including all boundary conditions.

4.3 Double Gate MOSFET

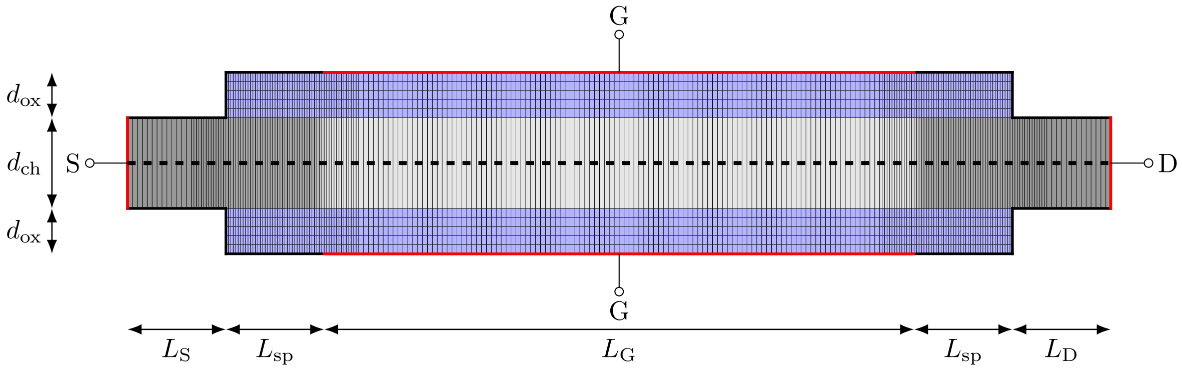

Figure 4.4: Double-Gate MOSFET including discretization grid, where the shading in the channel indicates the doping concentration N_{D}.

At this point, it is already possible to simulate somewhat more complex devices, where the PE is solved for two dimensions, but the transport is still one-dimensional. In Figure 4.4 a double-gate MOSFET similar to the one from [2] is shown, with a one-dimensional channel in the middle, sandwiched between two non-conducting oxide regions. Contacted boundaries are indicated by thick red, while uncontacted boundaries by thick black lines. The source and drain contact sizes are chosen as $L_{\mathrm{S}} = L_{\mathrm{D}} = 10\,\mathrm{nm}$, the spacer length is $L_{\mathrm{sp}} = 10\,\mathrm{nm}$ and the gate length $L_{\mathrm{G}} = 60\,\mathrm{nm}$. The channel and oxide thicknesses are $d_{\mathrm{ch}} = 5\,\mathrm{nm}$ and $d_{\mathrm{ox}} = 2.5\,\mathrm{nm}$, respectively. The permittivities are $\varepsilon_{\mathrm{ox}} = 3.9\,\varepsilon_0$ and $\varepsilon_{\mathrm{ch}} = 11.7\,\varepsilon_0$. The contact regions are doped with $N_{\mathrm{D}} = 4 \cdot 10^{20}\,\mathrm{cm}^{-3}$, which is reduced to $N_{\mathrm{D}} = 10^{20}\,\mathrm{cm}^{-3}$ in the spacer regions and $N_{\mathrm{D}} = 10^{15}\,\mathrm{cm}^{-3}$ between the gate contacts, with transition regions of about $t_{\mathrm{dop}} = 2\,\mathrm{nm}$. The relaxation time is again set to the constant value $\tau = 0.1\,\mathrm{ps}$. The work function difference for the gate contacts is set to $\phi_{\mathrm{MS}} = 0.3\,\mathrm{V}$.

For the discretization, a base grid size of $\Delta x = 0.5\,\mathrm{nm}$ is chosen, which is refined to $\Delta x = 0.25\,\mathrm{nm}$ in the spacer regions. In y-direction a grid size of $\Delta y = 0.5\,\mathrm{nm}$ is used for the oxide. For the CCFVM, the channel consists only of a single row of cells, while the VCFVM needs an additional grid line in the middle of the channel as the one-dimensional transport region, which is indicated by the dashed line in Figure 4.4.

To get a consistent coupling between the one-dimensional transport model and the two-dimensional PE, depending on the discretization method two different approaches are taken, which are related to the way the charge carriers are distributed perpendicular to the channel. For the VCFVM, the carriers are assumed to be located in an infinitesimal sheet in the middle of the channel, while the CCFVM assumes a uniform distribution in the channel. Quantum effects due to confinement are ignored in both cases.

For the VCFVM, coupling between the PE and the transport model is straightforward, the only thing to note is that the adjoint cell size in y-direction must be replaced by the actual channel thickness for the two-dimensional PE:

$$\Omega_{i,j} = \Delta x_i \, d_{\mathrm{ch}} \neq \Delta x_i \, \Delta y_j \, . \tag{4.60}$$

When calculating the terminal currents, this must be handled in a similar manner.

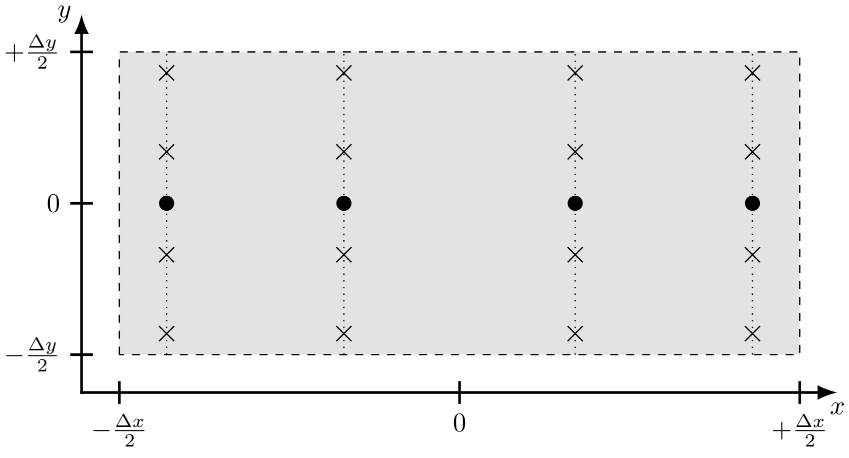

Figure 4.5: Two-dimensional PE cell merged with one-dimensional transport cell.

In the case of the CCFVM, the PE and the transport model have different Gauss-Legendre nodes (indicated by the cross-marks for the PE and the circles for the transport model in Figure 4.5). The charges given by the transport model are therefore uniformly distributed from the circles to the cross-marks, while on the other hand, the electric field supplied by the PE is averaged from the cross-marks to the circles (both processes are indicated by the dotted lines).

4.3.1 Stationary Results

In Figure 4.6 the cell averages of the potential $\overline{\varphi}$ for the CCFVM at equilibrium with a gate voltage of $V_{\mathrm{G}} = 0.2\,\mathrm{V}$ are shown. The solution appears to be very smooth, and no

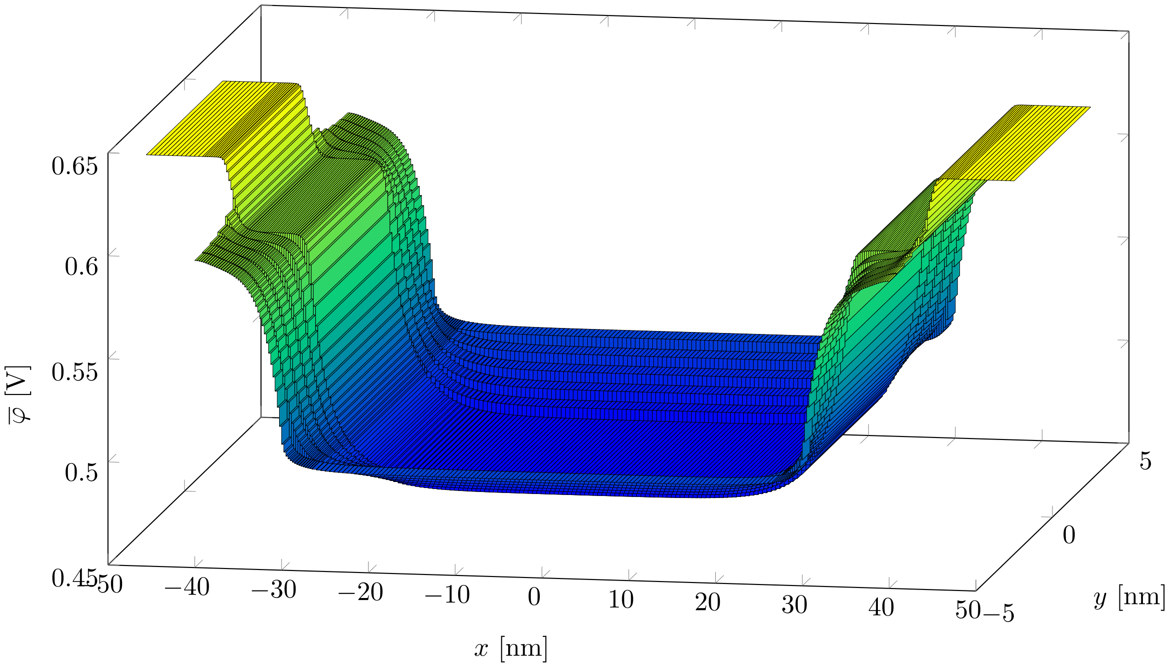

Figure 4.6: Cell averages of the potential at equilibrium for the double-gate MOSFET using the CCFVM at $V_{\mathrm{G}} = 0.2\,\mathrm{V}$.

artificial over- or undershoots are visible.

Similarly to the completely one-dimensional N^+-N-N^+ device from the previous chapter, the density and current density in the one-dimensional channel are compared for both discretization methods. In Figure 4.7 the equilibrium and non-equilibrium ($V_{\mathrm{DS}} = 50\,\mathrm{mV}$) electron density is shown for both the CCFVM and the VCFVM using the CDD model in both cases.

Like before, the results from the stationary system and the dynamic system under stationary conditions are in excellent agreement for the CCFVM. For the VCFVM however, the results show small deviations from the CCFVM. This is to be expected due to the different electron distribution perpendicular to the channel. To somewhat alleviate this difference, the gate voltage was increased slightly to $V_{\mathrm{G}} = 0.203\,\mathrm{V}$ for the VCFVM, since otherwise the density would have been consistently smaller (the graph in Figure 4.7 was calculated using the slightly increased voltage). Nevertheless, some small differences in the density between the VCFVM and the CCFVM persist.

Analogously, the current density is shown in Figure 4.8. As expected and similar to the purely one-dimensional case, there are artifacts in the dynamic system solution,

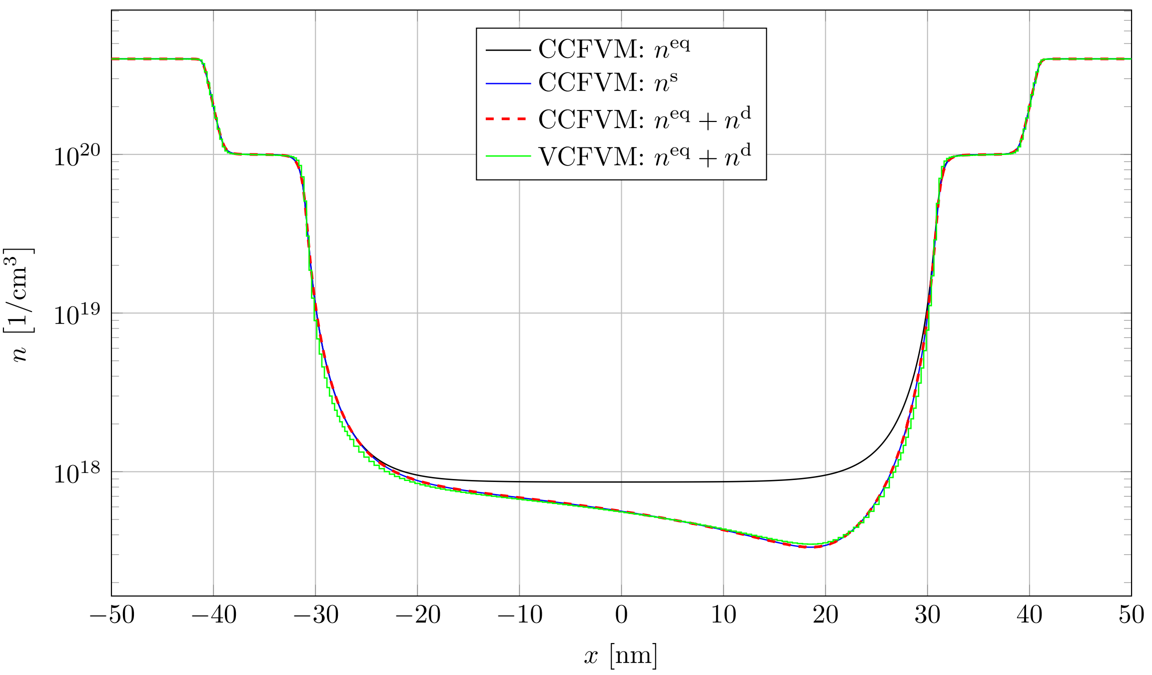

Figure 4.7: Electron density under equilibrium and non-equilibrium ($V_{\mathrm{DS}} = 50\,\mathrm{mV}$) conditions for the double-gate MOSFET using the CDD model at $V_{\mathrm{G}} = 0.2\,\mathrm{V}$.

which are much more pronounced in the only first-order accurate VCFVM compared to the third-order accurate CCFVM.

In Figure 4.9 the stationary output characteristics of the double-gate MOSFET using both the DD and CDD model are shown. For the DD model there are no limitations to the applied voltages, and the typical transition between linear and saturation behavior for MOSFETs can be seen. For small voltages, both models coincide, however, due to the limitation on the allowed drift velocity in case of the CDD model, it can not be solved for larger drain-source voltages. Keeping the drain-source voltage constant and increasing the gate voltage, leads to a larger density in the channel and at the same time a reduced drift velocity. Therefore, the CDD model is solvable for a larger region of drain-source voltages, when the gate voltage is increased.

The transfer characteristics are shown In Figure 4.10, where a DC voltage of $V_{\mathrm{DS}} = 50\,\mathrm{mV}$ is applied. In the subthreshold region the DD model has a slope of about $62\,\mathrm{mV/dec}$, which is very close to the theoretical limit of $60\,\mathrm{mV/dec}$ at $T = 300\,\mathrm{K}$. Therefore, almost no drain-induced barrier lowering takes place, as the double-gate exercises a very tight control over the relatively long channel. Again, the CDD model can

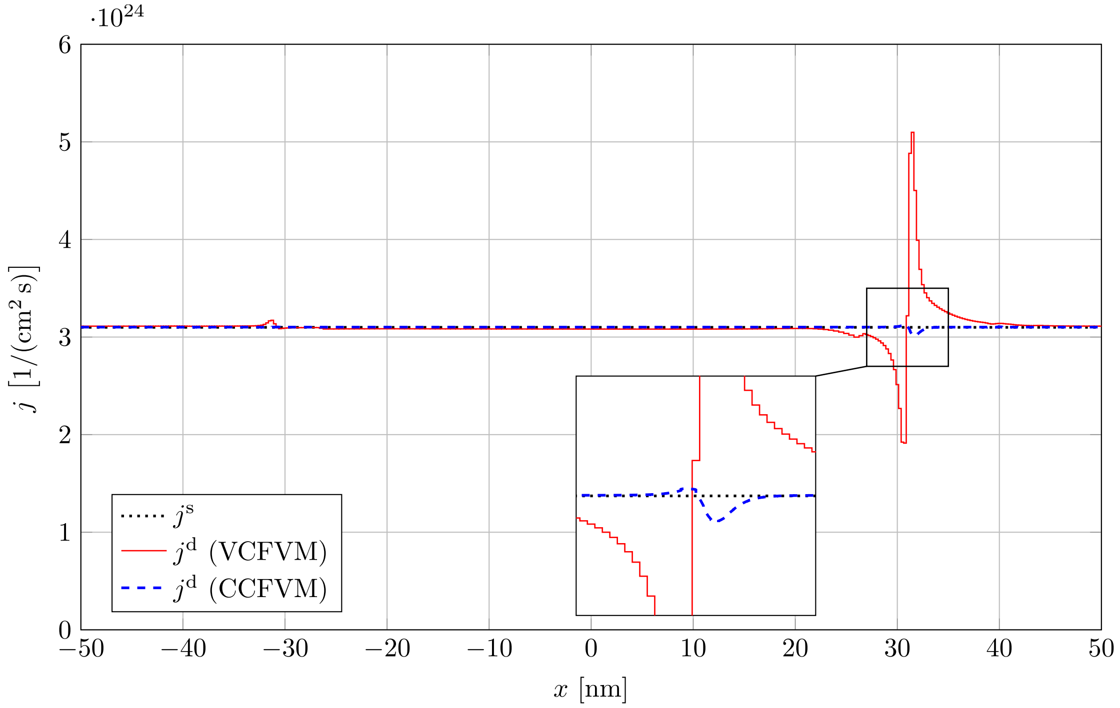

Figure 4.8: Current density for the double-gate MOSFET using the CDD model at $V_{\mathrm{G}} = 0.2\,\mathrm{V}$ and $V_{\mathrm{DS}} = 50\,\mathrm{mV}$.

not be solved for arbitrary voltages, but yields similar results in the regions where it can be solved.

4.3.2 Small-Signal Results

In addition to the stationary results, the small-signal results for both discretization methods are compared. In Figure 4.11 the drain-drain admittance for a wide frequency range is shown. Slight deviations between the two methods can be seen especially for lower frequencies, which can be explained in part again due to the different distribution of carriers in the channel. On the other hand, for very high frequencies the methods are in nearly perfect agreement, because the displacement current becomes the dominant term. At these high frequencies there is no relevant electron transport in the channel, and the device acts more like a capacitor.

For the more relevant frequency range of 1 THz to 10 THz, some resonances can be seen, which appear to be much more pronounced for the CCFVM compared to the VCFVM. This effect can be seen much more clearly in Figure 4.12, which shows the

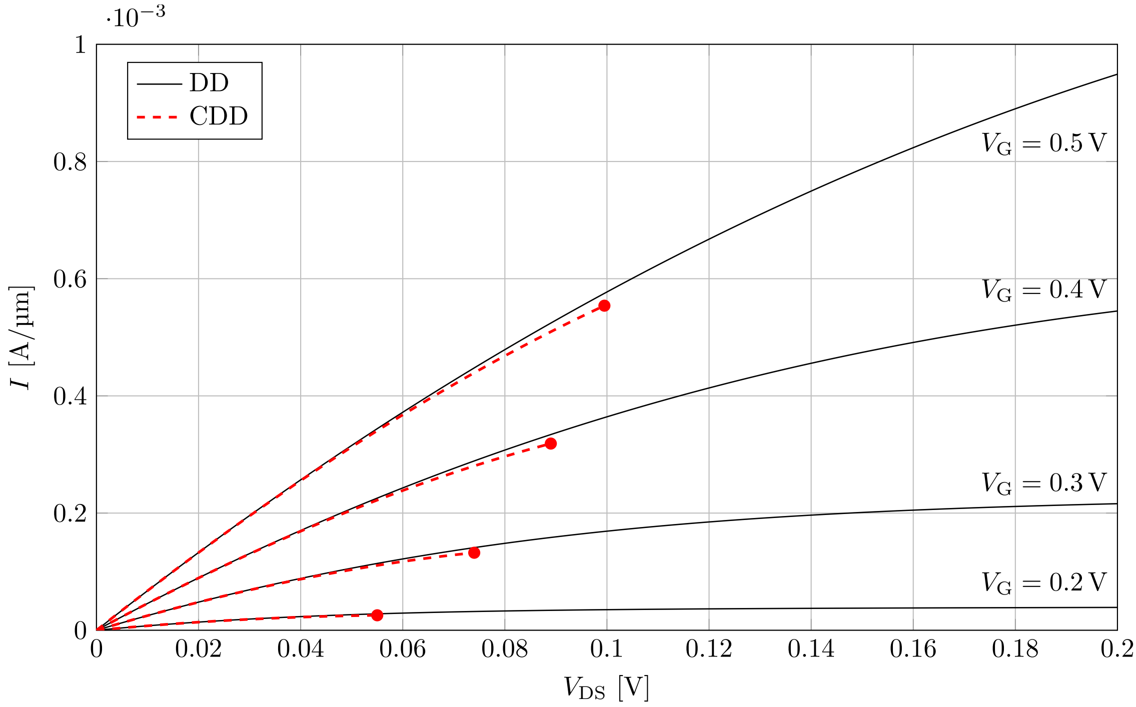

Figure 4.9: Output characteristics of the double-gate MOSFET.

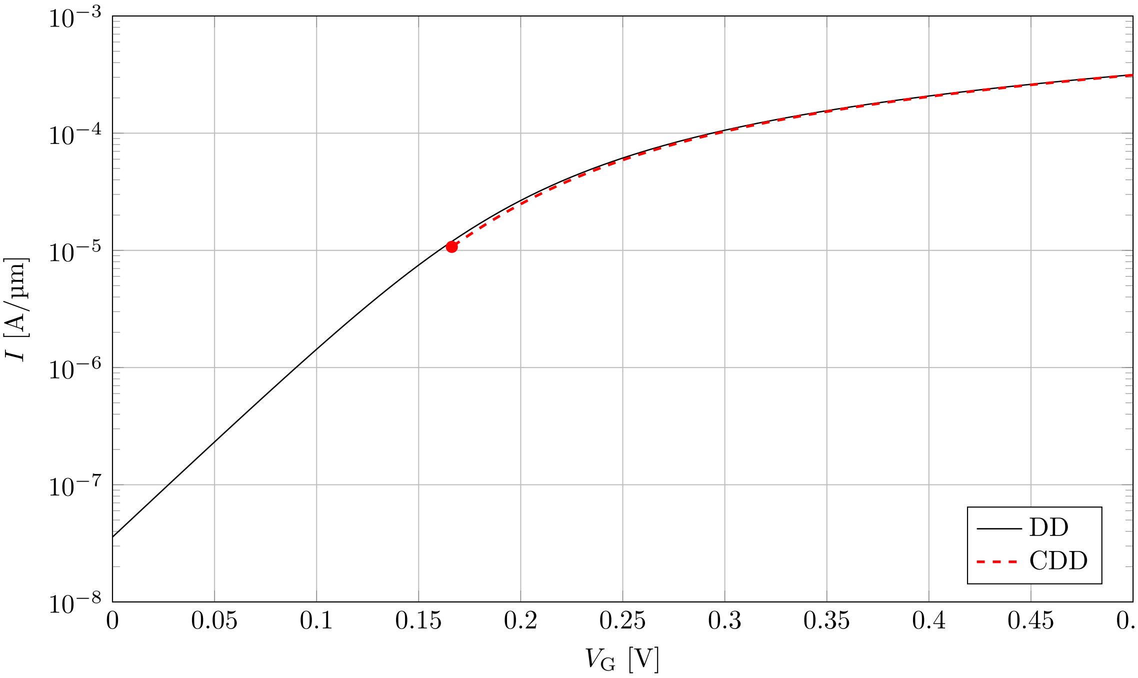

Figure 4.10: Transfer characteristics of the double-gate MOSFET at $V_{DS} = 50\,\text{mV}$.

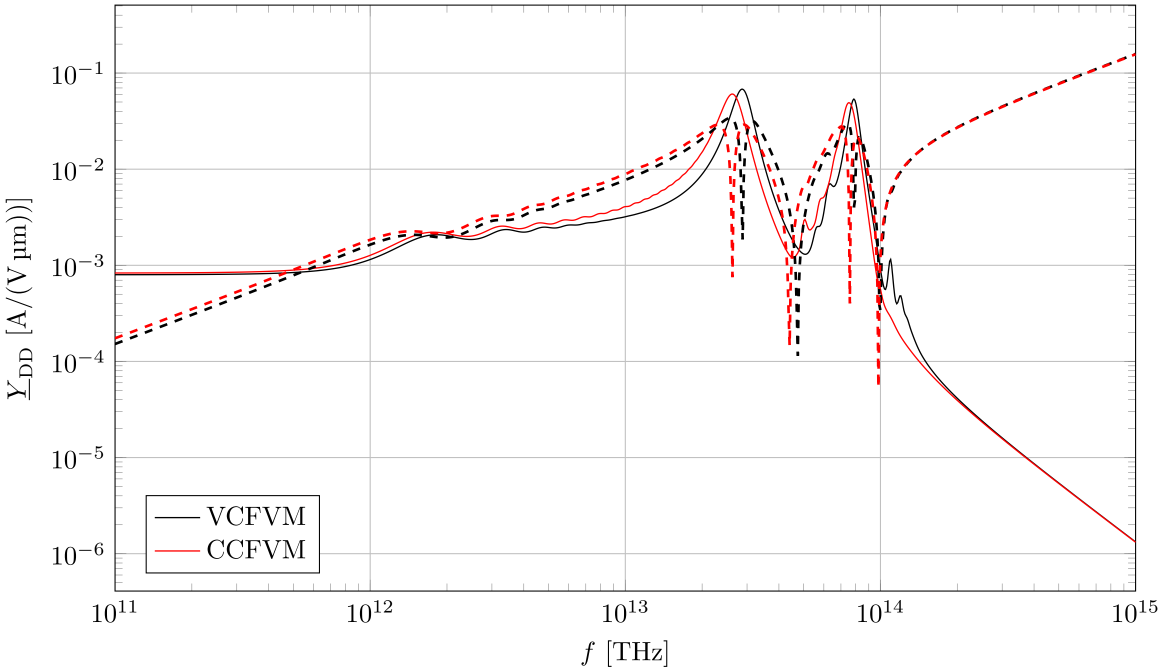

Figure 4.11: Real (solid) and absolute value of the imaginary (dashed) part of $\underline{Y}_{\mathrm{DD}}$ at equilibrium.

drain-source admittance in that range. In [2] it was already shown, that this effect is due to the first-order nature of the VCFVM, which introduces a large amount of damping at higher frequencies. In contrast, the resonances are almost undamped by the third-order accurate CCFVM.

4.3.3 Large-Signal Transient Results

For further analysis, the detector circuit from [18, 3], shown in Figure 4.13, is considered. Similar to [68, 3, 2], the circuit is simplified by applying the AC voltage to the source terminal and keeping the gate and drain terminals AC-wise grounded, which can be justified due to the high admittance of the coupling capacitance $C_{\mathrm{GD,ext}}$ at high frequencies.

The large-signal results shown in this section are generated using the CCFVM in combination with the method of lines approach. After discretization of the spatial derivatives, the equation system has the form

$$\mathbf{D}\frac{\partial}{\partial t}\boldsymbol{u} + \boldsymbol{f}(\boldsymbol{u}, t) = \mathbf{0}\,. \tag{4.61}$$

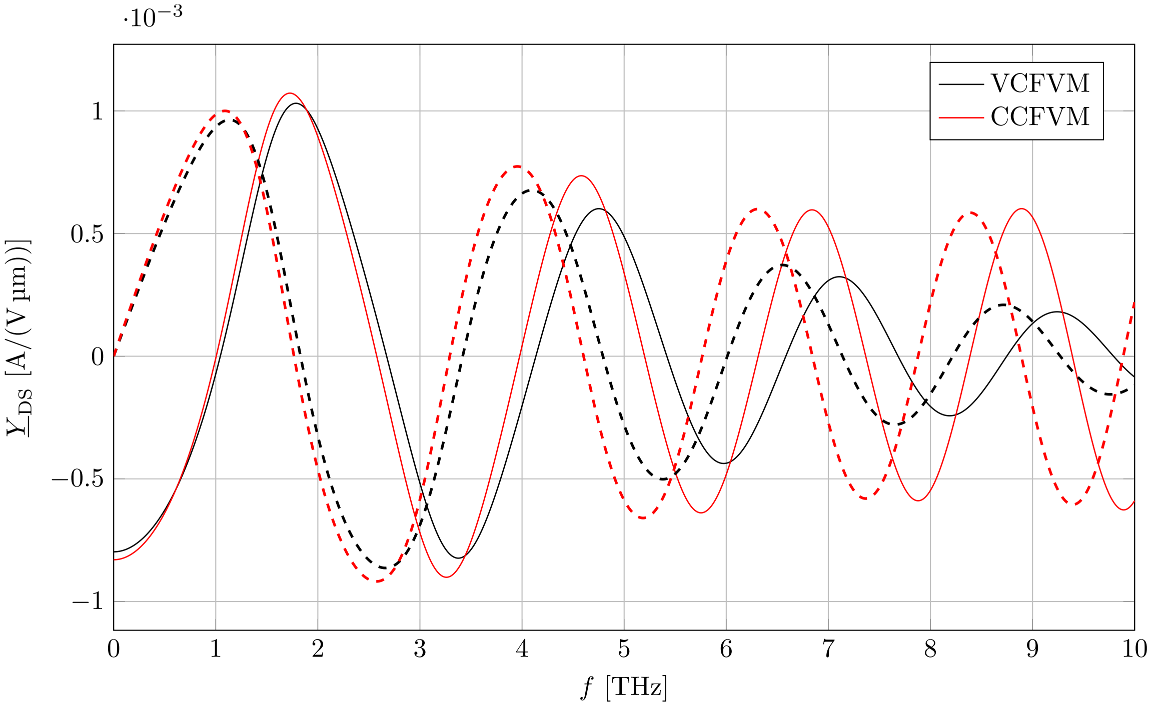

Figure 4.12: Real (solid) and imaginary (dashed) part of $\underline{Y}_{\mathrm{DS}}$ at equilibrium.

Transient analysis is done by applying the linear multistep BDF2 method [69, 70]. The time derivative at a time step $t^{(n+1)}$ is approximated by

$$\left.\frac{\partial}{\partial t}\boldsymbol{u}\right|_{t=t^{(n+1)}} \approx \alpha^{(n)}\boldsymbol{u}^{(n-1)} + \beta^{(n)}\boldsymbol{u}^{(n)} + \gamma^{(n)}\boldsymbol{u}^{(n+1)}\,, \tag{4.62}$$

with

$$\begin{aligned}
\alpha^{(n)} &= \frac{\Delta t^{(n)}}{\Delta t^{(n-1)}(\Delta t^{(n)} + \Delta t^{(n-1)})} \\
\beta^{(n)} &= -\frac{\Delta t^{(n)} + \Delta t^{(n-1)}}{\Delta t^{(n)}\Delta t^{(n-1)}} \\
\gamma^{(n)} &= \frac{\Delta t^{(n-1)} + 2\Delta t^{(n)}}{\Delta t^{(n)}}\,,
\end{aligned} \tag{4.63}$$

and $\Delta t^{(n)} = t^{(n+1)} - t^{(n)}$. Alternatively, the modified BDF2 (MBDF2) method based on trigonometric functions [71] with frequency dependent weights and much less numerical damping can be used.

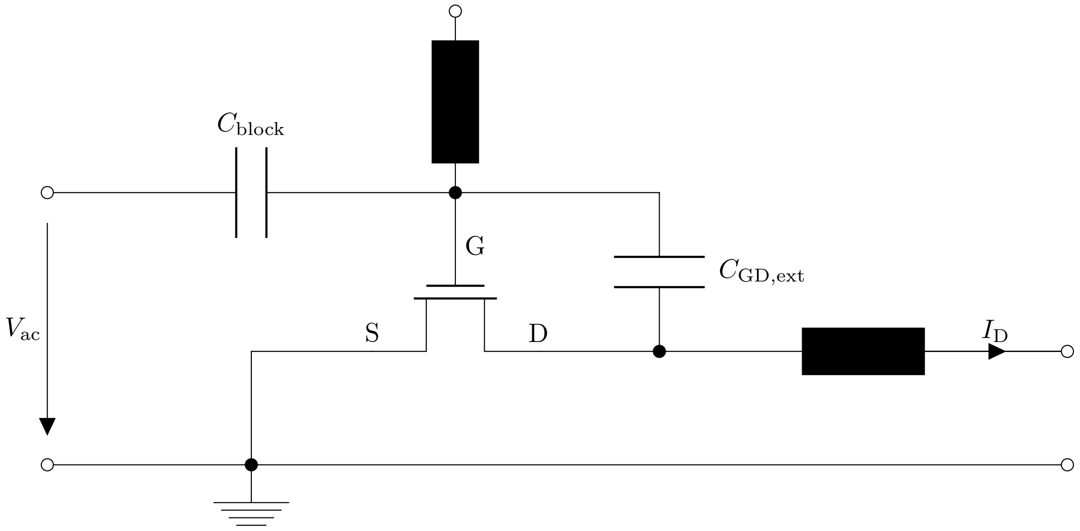

Figure 4.13: Detector circuit for resistive mixing [18, 3].

The resulting non-linear equation system

$$\mathbf{D}\big(\alpha^{(n)}\boldsymbol{u}^{(n-1)} + \beta^{(n)}\boldsymbol{u}^{(n)} + \gamma^{(n)}\boldsymbol{u}^{(n+1)}\big) + \boldsymbol{f}\big(\boldsymbol{u}^{(n+1)}, t^{(n+1)}\big) = \mathbf{0} \tag{4.64}$$

is solved for $\boldsymbol{u}^{(n+1)}$ by a Newton iteration, similar to the steady-state. The time step size is automatically adjusted by a heuristic adaptive step size algorithm, which does not require any additional information about the equation system [2].

In Figure 4.14 the source and drain currents over time for a sinusoidal voltage applied to the source terminal $V_{\mathrm{S}}(t) = V_{\mathrm{A}}\sin(\omega t)$ with different amplitudes are shown. The frequency was fixed to $f = 1\,\mathrm{THz}$. Especially for large amplitudes, the non-linearity of the device can be seen in the drain current, which becomes asymmetric and deviates significantly from a harmonic oscillation. For the largest amplitude of $40\,\mathrm{mV}$, a high-frequency oscillation that is superimposed on the base signal can be seen.

After only a few oscillations, the transient simulation reaches the PSS, which alternatively could also be calculated directly by the harmonic balance approach [72]. Figure 4.15 shows the cell averages of the dynamic part of the density, as well as the total interface current density for a single period of the PSS. In the contact regions the density stays almost constant, however at the transition between source region and channel a large oscillation is visible, which travels as a damped wave into the channel. Corresponding to the almost constant density in time, the current density is nearly constant in space in the contact regions. Only in the channel a moving wave can be seen, leading

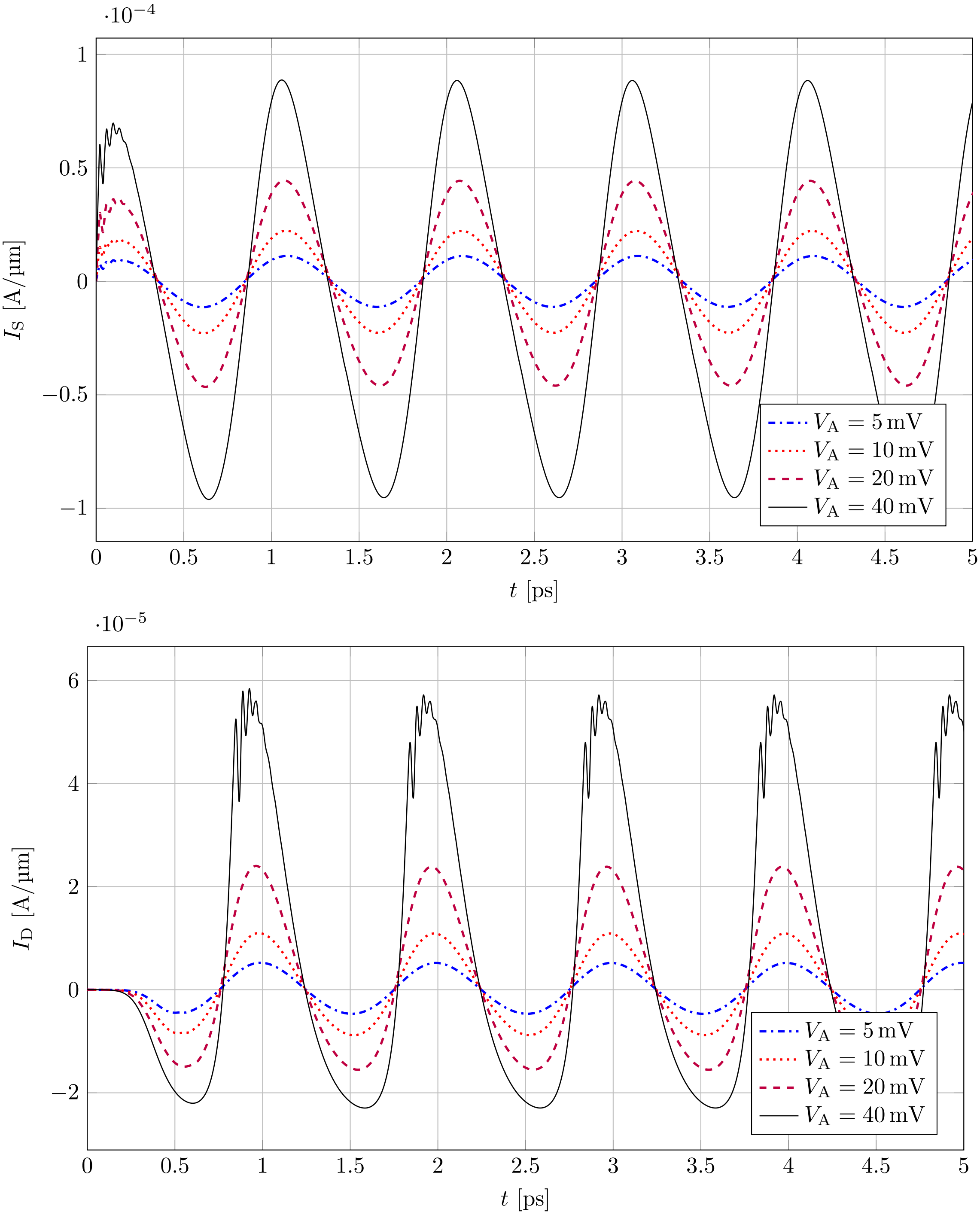

Figure 4.14: Source and drain currents over time for a sinusoidal signal applied to the source terminal for the CCFVM.

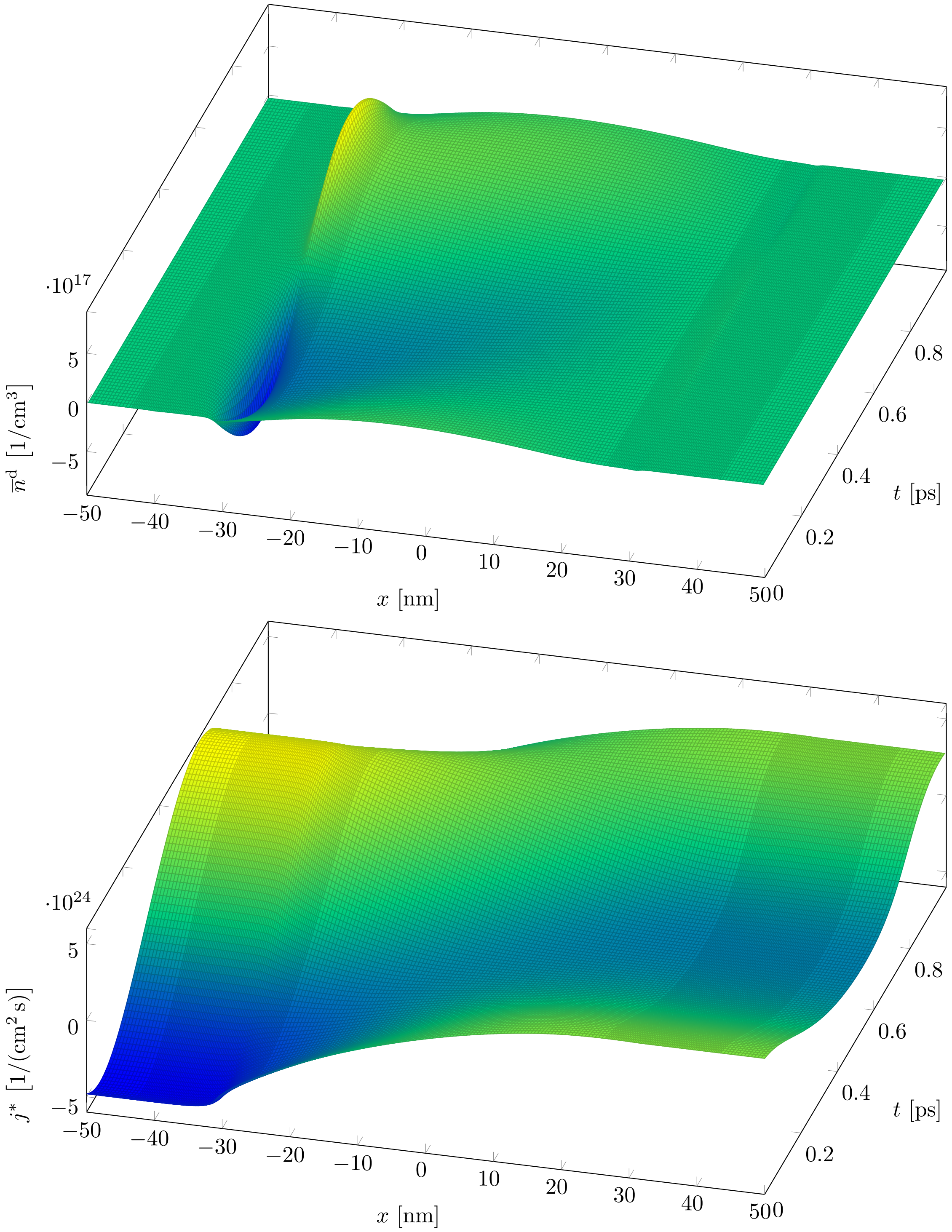

Figure 4.15: Electron density and current density for the PSS.

to a phase shift for the current density between the source and drain side [2]. Since for the actual charge transport the interface current density is relevant, only this quantity is shown here. It is smoother than the cell average current density, which exhibits some numerical artifacts, as demonstrated before in the steady-state simulations.

Using the PSS results, the current responsivity of the detector can be calculated by dividing the DC component of the drain current by the source AC input power [3]

$$R_\mathrm{I} = \frac{I_\mathrm{D}^\mathrm{DC}}{P_\mathrm{S}^\mathrm{AC}} \,, \tag{4.65}$$

where the AC input power is given by the time average of the instantaneous power

$$P_\mathrm{S}^\mathrm{AC} = \frac{1}{T}\int_0^T V_\mathrm{S}(t) I_\mathrm{S}(t)\,\mathrm{d}t \;. \tag{4.66}$$

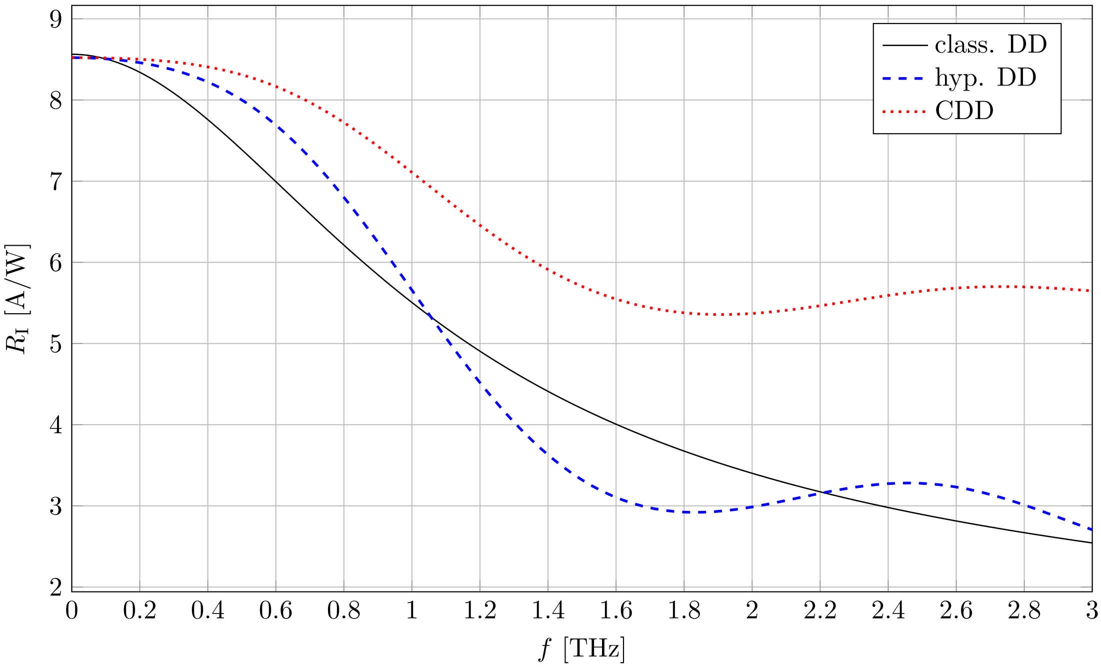

Figure 4.16: Detector responsivity over frequency for the classical and the hyperbolic DD model as well as the CDD model.

In Figure 4.16 the responsivity is shown for frequencies up to $f = 3\,\mathrm{THz}$ for both the DD and the CDD model as well as the classical (non-hyperbolic) DD model. The amplitude of the AC signal was set to $V_\mathrm{A} = 0.1\,\mathrm{mV}$, which is small enough to not influence the result, since the responsivity is independent on V_A for small V_A. For low frequencies, all three models yield the same result, with a responsivity of $R_\mathrm{I} \approx 8.5\,\mathrm{A/W}$. However, for larger frequencies in the THz regime, the responsivity given by the classical DD model is simply monotonically decreasing, while the hyperbolic DD and the CDD model show some oscillatory behaviour, due to the resonant coupling between the signal and the electron plasma. Furthermore, the CDD model yields a much larger responsivity compared to the hyperbolic DD model, which at first glance seems counterintuitive, since for a DC bias of $0\,\mathrm{V}$ the convective term has no effect on small-signal results. Then again, the responsivity is a non-linear effect which can not be captured by the linearized small-signal calculations [2], as there is no DC shift of the current in the small-signal regime. The difference in the responsivities shown here therefore highlights the need for non-linear large-signal simulations.

4.4 Two-Dimensional Transport Model

Up to this point, the transport was only simulated in one dimension. However, for fully two-dimensional devices, it should be solved in two dimensions as well. In that case, the models considered in this work have the form

$$\frac{\partial}{\partial t}\boldsymbol{U} + \frac{\partial}{\partial x}\boldsymbol{F}_x + \frac{\partial}{\partial y}\boldsymbol{F}_y = \boldsymbol{S}\,, \tag{4.67}$$

with $\boldsymbol{F}_x = \boldsymbol{F}_x(\boldsymbol{U})$, $\boldsymbol{F}_y = \boldsymbol{F}_y(\boldsymbol{u})$ and $\boldsymbol{S} = \boldsymbol{S}(\boldsymbol{U}, \boldsymbol{E})$.

For instance, the two-dimensional CDD model is given by

$$\boldsymbol{U} = \begin{pmatrix} n \\ j_x \\ j_y \end{pmatrix}, \ \boldsymbol{F}_x = \begin{pmatrix} j_x \\ c_\mathrm{T}^2 n + \frac{j_x^2}{n} \\ \frac{j_x j_y}{n} \end{pmatrix}, \ \boldsymbol{F}_y = \begin{pmatrix} j_y \\ \frac{j_x j_y}{n} \\ c_\mathrm{T}^2 n + \frac{j_y^2}{n} \end{pmatrix} \quad \text{and} \quad \boldsymbol{S} = \begin{pmatrix} 0 \\ -\frac{e}{m^*}E_x n - \frac{j_x}{\tau} \\ -\frac{e}{m^*}E_y n - \frac{j_y}{\tau} \end{pmatrix}. \tag{4.68}$$

In order to discretize such equations in a well-balanced way, the variables are again split into a stationary and a dynamic part

$$\begin{aligned} \boldsymbol{U}(\boldsymbol{r}, t) &= \boldsymbol{U}^\mathrm{s}(\boldsymbol{r}) + \boldsymbol{U}^\mathrm{d}(\boldsymbol{r}, t) \\ \boldsymbol{E}(\boldsymbol{r}, t) &= \boldsymbol{E}^\mathrm{s}(\boldsymbol{r}) + \boldsymbol{E}^\mathrm{d}(\boldsymbol{r}, t)\,, \end{aligned} \tag{4.69}$$

where the stationary part must satisfy

$$\frac{\partial}{\partial x}\boldsymbol{F}_x^\mathrm{s} + \frac{\partial}{\partial y}\boldsymbol{F}_y^\mathrm{s} = \boldsymbol{S}^\mathrm{s}\,, \tag{4.70}$$

with $\boldsymbol{F}_x^\mathrm{s} = \boldsymbol{F}_x(\boldsymbol{U}^\mathrm{s})$, $\boldsymbol{F}_y^\mathrm{s} = \boldsymbol{F}_y(\boldsymbol{U}^\mathrm{s})$ and $\boldsymbol{S}^\mathrm{s} = \boldsymbol{S}(\boldsymbol{U}^\mathrm{s}, \boldsymbol{E}^\mathrm{s})$. In contrast to the one-dimensional case, this is still difficult to solve, and it is not possible to adapt the approach using a numerical ODE solver to this case. Instead, the well-known equilibrium solution is used as a stationary solution

$$\boldsymbol{U}^\mathrm{s}(x, y) = \boldsymbol{U}^\mathrm{eq}(x, y)\,. \tag{4.71}$$

Subtracting eq. (4.70) from eq. (4.67) then results in

$$\frac{\partial}{\partial t}\boldsymbol{U} + \frac{\partial}{\partial x}(\boldsymbol{F}_x - \boldsymbol{F}_x^\mathrm{s}) + \frac{\partial}{\partial y}\big(\boldsymbol{F}_y - \boldsymbol{F}_y^\mathrm{s}\big) = \boldsymbol{S} - \boldsymbol{S}^\mathrm{s}\,, \tag{4.72}$$

which is well-balanced exactly for the equilibrium state by construction.

4.4.1 Discretization of the Two-Dimensional Transport Model

Unfortunately, for two dimensions the piecewise constant reconstruction used by the vertex-centered method is not applicable, because even under stationary conditions, although it is divergence-free, the current density is not necessarily constant in the device. The piecewise constant reconstruction allows the current density to change only on the integration volume interfaces, resulting in discontinuities at these points. These do not even approximately vanish for stationary conditions, resulting in the creation of moving waves with non-zero amplitude by the Riemann solver. This in turn leads to strong artificial oscillations.

To alleviate this problem, the components of the current density must be allowed to change inside of the cells. Therefore, only the high-order cell-centered discretization is considered for the two-dimensional transport case.

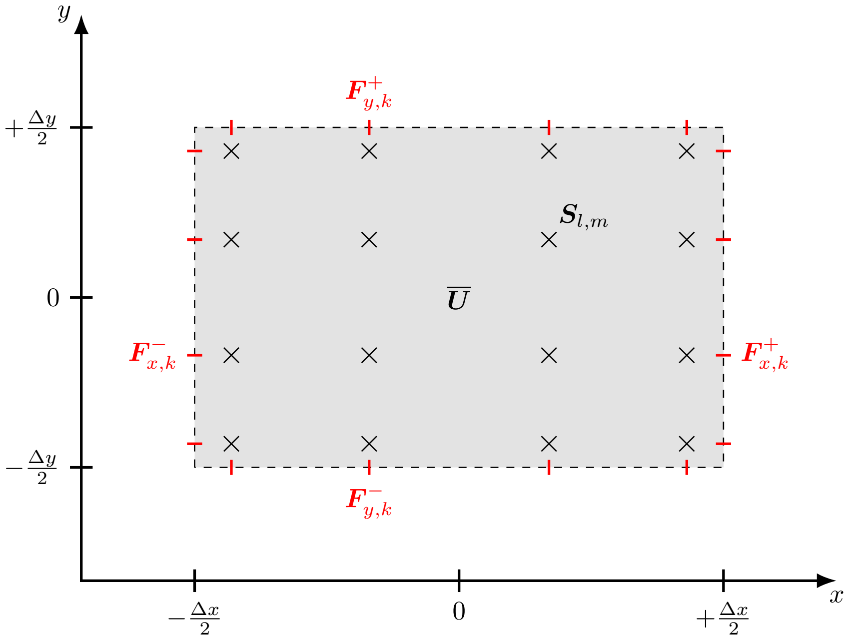

Figure 4.17: Discretizing the transport model using four Gauss-Legendre nodes for both directions.

Like before, only a single cell is considered for the derivation of the discretized scheme, which is why all grid indices can be dropped. Integrating eq. (4.72) over a rectangular cell yields

$$\frac{\partial}{\partial t}\overline{\boldsymbol{U}} + \frac{\left(\overline{\boldsymbol{F}}_x^{+} - \overline{\boldsymbol{F}}_x^{\mathrm{s}+}\right) - \left(\overline{\boldsymbol{F}}_x^{-} - \overline{\boldsymbol{F}}_x^{\mathrm{s}-}\right)}{\Delta x} + \frac{\left(\overline{\boldsymbol{F}}_y^{+} - \overline{\boldsymbol{F}}_y^{\mathrm{s}+}\right) - \left(\overline{\boldsymbol{F}}_y^{-} - \overline{\boldsymbol{F}}_y^{\mathrm{s}-}\right)}{\Delta y} = \overline{\boldsymbol{S}} - \overline{\boldsymbol{S}}^{\mathrm{s}}\,, \tag{4.73}$$

where the cell average value

$$\overline{\boldsymbol{U}} = \frac{1}{\Delta x\,\Delta y}\int_{-\Delta y/2}^{\Delta y/2}\int_{-\Delta x/2}^{\Delta x/2}\boldsymbol{U}(x,y)\,\mathrm{d}x\,\mathrm{d}y \tag{4.74}$$

is chosen as the discrete solution variable. Similarly, the source terms are given by

$$\overline{\boldsymbol{S}}^{(\mathrm{s})} = \frac{1}{\Delta x\,\Delta y}\int_{-\Delta y/2}^{\Delta y/2}\int_{-\Delta x/2}^{\Delta x/2}\boldsymbol{S}^{(\mathrm{s})}(x,y)\,\mathrm{d}x\,\mathrm{d}y\ , \tag{4.75}$$

and the average fluxes on the cell surfaces are

$$\begin{aligned}\overline{\boldsymbol{F}}_x^{(\mathrm{s})\pm} &= \frac{1}{\Delta y}\int_{-\Delta y/2}^{\Delta y/2}\boldsymbol{F}_x^{(\mathrm{s})}\left(\pm\frac{\Delta x}{2}, y\right)\mathrm{d}y\\ \overline{\boldsymbol{F}}_y^{(\mathrm{s})\pm} &= \frac{1}{\Delta x}\int_{-\Delta x/2}^{\Delta x/2}\boldsymbol{F}_y^{(\mathrm{s})}\left(x, \pm\frac{\Delta y}{2}\right)\mathrm{d}x\ .\end{aligned} \tag{4.76}$$

Both eqs. (4.75) and (4.76) are approximated using the Gauss-Legendre quadrature (see Figure 4.17)

$$\overline{\boldsymbol{S}}^{(\mathrm{s})} \approx \frac{1}{4}\sum_{l=1}^{N_{\mathrm{G}}}\sum_{m=1}^{N_{\mathrm{G}}}\boldsymbol{S}^{(\mathrm{s})}\left(\frac{\Delta x}{2}\xi_l, \frac{\Delta y}{2}\xi_m\right)w_l\,w_m = \frac{1}{4}\sum_{k=1}^{N_{\mathrm{G}}}\sum_{l=1}^{N_{\mathrm{G}}}\boldsymbol{S}_{l,m}^{(\mathrm{s})}\,w_l\,w_m \tag{4.77}$$

and

$$\begin{aligned}\overline{\boldsymbol{F}}_x^{(\mathrm{s})\pm} &\approx \frac{1}{2}\sum_{k=1}^{N_{\mathrm{G}}}\boldsymbol{F}_x^{(\mathrm{s})}\left(\pm\frac{\Delta x}{2}, \frac{\Delta y}{2}\xi_k\right)w_k = \frac{1}{2}\sum_{k=1}^{N_{\mathrm{G}}}\boldsymbol{F}_{x,k}^{(\mathrm{s})}\,w_k\\ \overline{\boldsymbol{F}}_y^{(\mathrm{s})\pm} &\approx \frac{1}{2}\sum_{k=1}^{N_{\mathrm{G}}}\boldsymbol{F}_y^{(\mathrm{s})}\left(\frac{\Delta x}{2}\xi_k, \pm\frac{\Delta y}{2}\right)w_k = \frac{1}{2}\sum_{k=1}^{N_{\mathrm{G}}}\boldsymbol{F}_{y,k}^{(\mathrm{s})}\,w_k\,,\end{aligned} \tag{4.78}$$

where the surface fluxes at the individual points are calculated using a one-dimensional Riemann solver in the direction normal to the face. For example, at a face in x-direction, the equation

$$\frac{\partial}{\partial t}\boldsymbol{U} + \frac{\partial}{\partial x}\boldsymbol{F}_x(\boldsymbol{U}) = \boldsymbol{0} \tag{4.79}$$

is solved for each Gauss-Legendre point on the surface, using initial data for $\boldsymbol{U}$ from both neighboring cells. Note, that in addition to the normal component of the vectorial variables, in two dimensions also a tangential component is included in $\boldsymbol{U}$, so the Riemann solver needs to be changed to account for that. For instance, the state vector of the CDD model in two dimensions has three components (one density and two current densities), leading to a Riemann solution with three waves, instead of two. However, the additional wave is a simple linear wave, only coupling to the tangential current density. Therefore, no drastic changes to the solver have to be made. The tangential current density on the interface is simply given by either one of the two initial values on both sides of the interface, depending on the sign of the drift velocity normal to the interface.

In Figure 4.17 all Gauss-Legendre points needed for the flux and source term calculation are shown. To reconstruct $\boldsymbol{U}$ at these points, the one-dimensional reconstruction procedure used before has to be extended to two dimensions.

4.4.2 Two-Dimensional Extension of the LDLR

As the LDLR is inherently one-dimensional, in order to extend it to two dimensions, it is simply applied successively in both directions.

Starting with the x-direction, the LDLR is applied to the center, left and right cells to reconstruct values on the cell surfaces as well as at the Gauss-Legendre nodes inside of the center cell. The surface values are located infinitesimally close to the surfaces, however still inside of the center cell. Since no reconstruction in y-direction has been performed yet, the reconstructed values represent point values in x-, but average values in y-direction (see Figure 4.18a). In the second step, these y-averages can then be used to reconstruct point values in both x- and y-direction. For that purpose, the LDLR is applied in y-direction once for each of the half average values (see Figure 4.18b). The resulting point values are third-order accurate in both x- and y-direction, and the full stencil shown in Figure 4.18 is used, consisting of nine cells in total. The point values are also consistent with the average value for the center cell, which is given by the two-dimensional Gauss-Legendre quadrature rule.

In contrast to the one-dimensional case, additional boundary conditions have to be

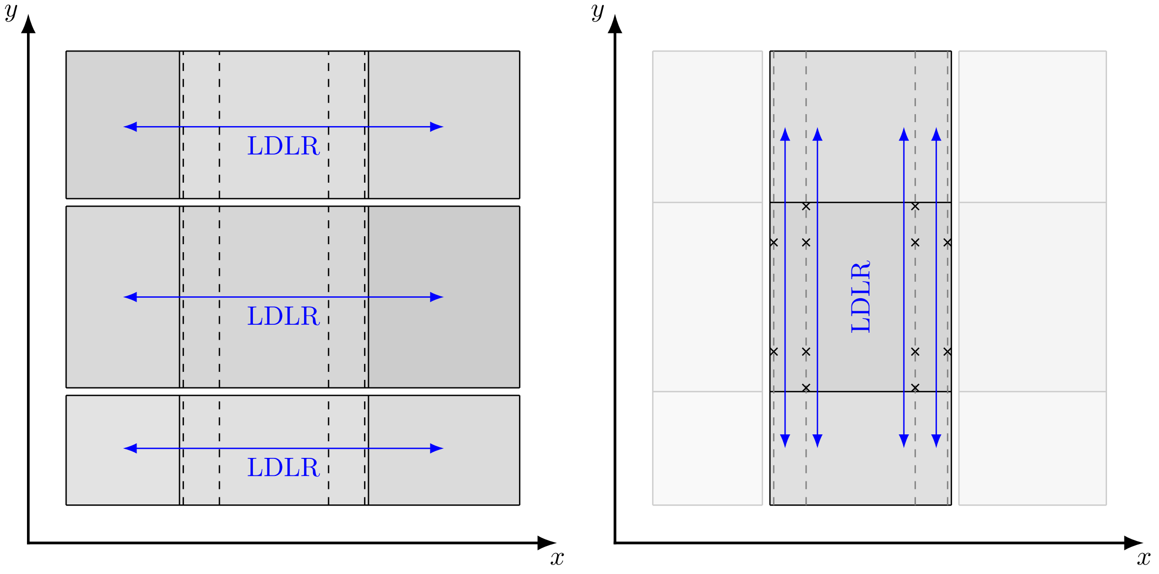

(a) Reconstruction in x-direction.
(b) Subsequent reconstruction in y-direction.

Figure 4.18: Reconstruction procedure in two dimensions.

implemented for the transport cells bordering on oxide regions, or uncontacted device boundaries. Since electrons can only enter and leave the device through its contacts, the normal component of the current density on such boundaries must be zero, corresponding to a Dirichlet boundary condition. For the tangential component, homogeneous Neumann boundary conditions are used. Finally, to get a consistent boundary condition for the electron density as well, the underlying PDE is considered. Assuming a transport cell is bordering an uncontacted device boundary at $x = -\frac{\Delta x}{2}$, the constitutive equation for the current density in x-direction for the CDD model is then given by

$$\frac{\partial}{\partial t} j_x + \frac{\partial}{\partial x}\left(c_{\mathrm{T}}^2 n + \frac{j_x^2}{n}\right) + \frac{\partial}{\partial y}\left(\frac{j_x j_y}{n}\right) = -\frac{e}{m^*} E_x n - \frac{j_x}{\tau}\,. \tag{4.80}$$

Using $j_x\big|_{-\Delta x/2} = 0$, the resulting boundary condition involving n, $\frac{\partial}{\partial x} n$ and E_x is then given by

$$\left.\left(c_{\mathrm{T}}^2 \frac{\partial n}{\partial x} + \frac{e}{m^*} E_x n\right)\right|_{x=-\Delta x/2} = 0\,, \tag{4.81}$$

which is the same for both the DD and CDD model. This condition then replaces one of the equations from eq. (3.156) in the non-negative reconstruction of the density.

4.5 Silicon-On-Insulator MOSFET

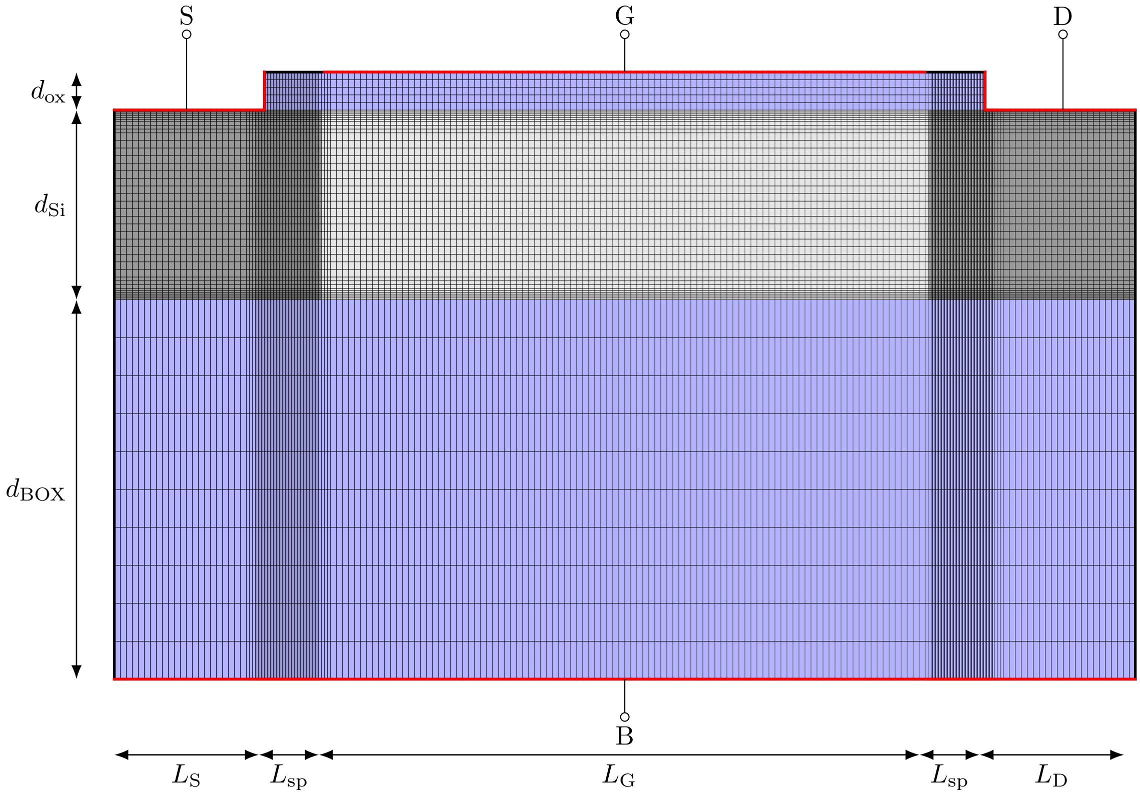

Figure 4.19: Simplified SOI MOSFET including discretization grid.

In this section the discretization scheme is applied to a two-dimensional SOI MOSFET, as shown in Figure 4.19. For simplicity reasons, a back gate is connected directly to the Buried Oxide Layer (BOX), and the substrate is neglected. The thicknesses of the BOX, the silicon layer and the gate oxide are given by $d_{\mathrm{BOX}} = 50\,\mathrm{nm}$, $d_{\mathrm{Si}} = 25\,\mathrm{nm}$ and $d_{\mathrm{ox}} = 5\,\mathrm{nm}$ respectively. The source and drain regions have a length of $L_{\mathrm{S}} = L_{\mathrm{D}} = 25\,\mathrm{nm}$. The spacer length is $L_{\mathrm{sp}} = 10\,\mathrm{nm}$ and the gate length is $L_{\mathrm{G}} = 100\,\mathrm{nm}$. The buried as well as the gate oxide have the same permittivity of $\varepsilon_{\mathrm{ox}} = 3.9\,\varepsilon_0$, while the silicon permittivity is $\varepsilon_{\mathrm{Si}} = 11.7\,\varepsilon_0$. The relaxation time in the whole transport region is assumed to be constant at $\tau = 0.1\,\mathrm{ps}$ and an effective mass of $m^* = 0.28621\,m_{\mathrm{e}}$ is used. The doping concentrations are $N_{\mathrm{D}} = 10^{20}\,\mathrm{cm}^{-3}$ in the contact regions, while the region under the gate is slightly p-doped with $N_{\mathrm{A}} = 10^{16}\,\mathrm{cm}^{-3}$. For both gate contacts a metal-semiconductor work-function difference of $\phi_{\mathrm{MS}} = 0.3\,\mathrm{V}$ is assumed.

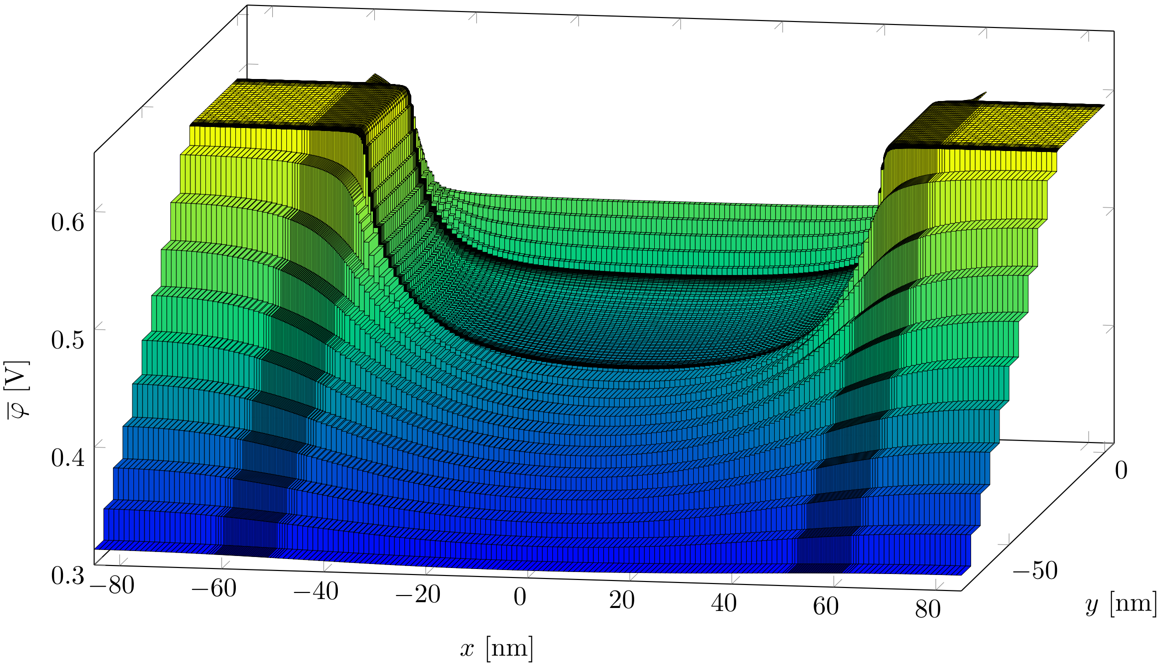

Figure 4.20: Cell average potential at equilibrium.

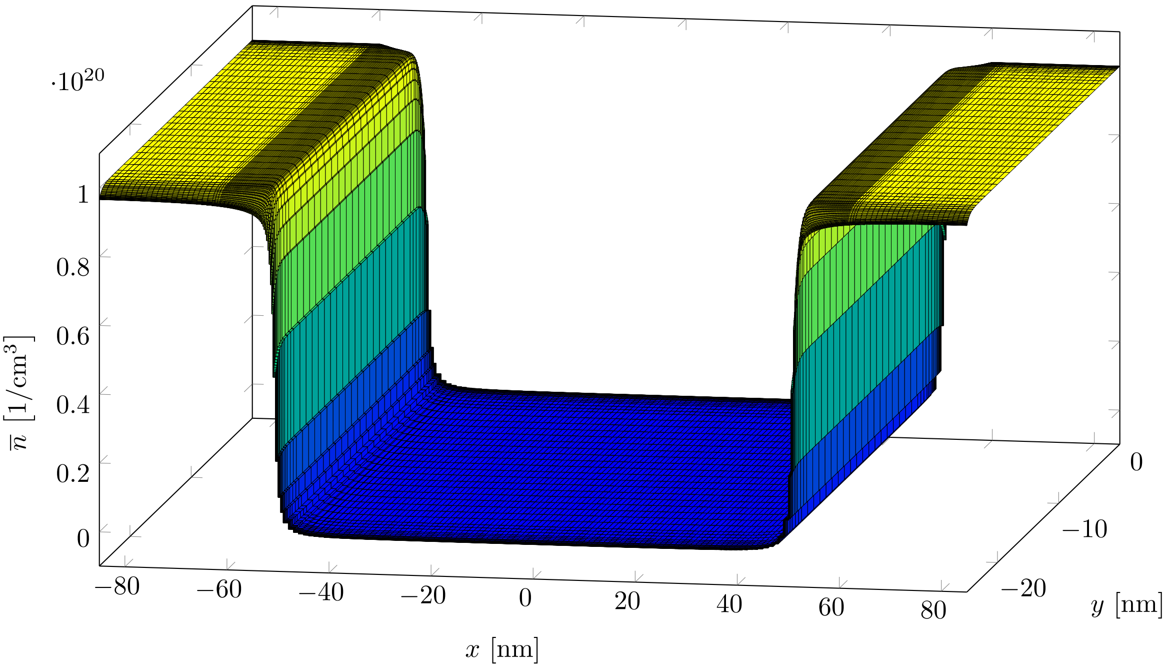

Figure 4.21: Cell average electron density at equilibrium.

Figure 4.20 shows the average potential in each cell for the whole device under equilibrium conditions. In Figure 4.21 the corresponding electron density in the semiconductor region is shown. The solution seems to be sufficiently stable and no artificial oscillations are visible, demonstrating the stability of the two-dimensional discretization scheme for the PE. In the following the steady-state is calculated when a small drain-source voltage is applied.

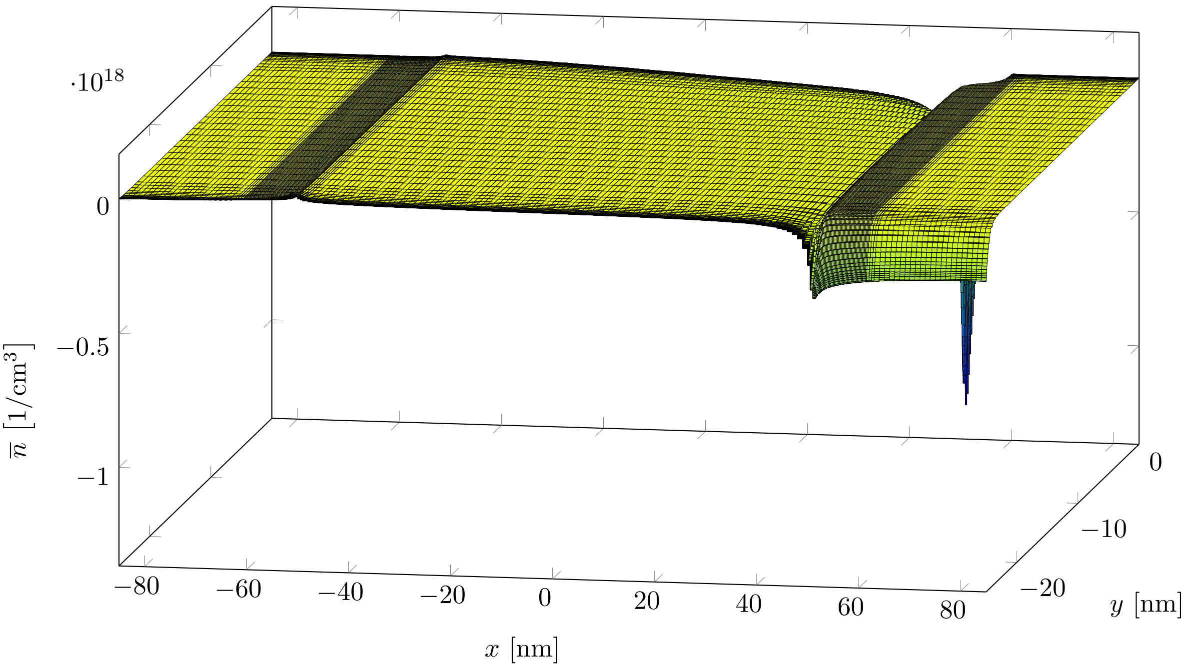

Figure 4.22: Dynamic density under stationary conditions.

Figure 4.22 displays the the dynamic density ($n^{\mathrm{d}} = n - n^{\mathrm{eq}}$) for a stationary applied drain-source voltage of $V_{\mathrm{DS}} = 20\,\mathrm{mV}$. While the total density is still positive, near the drain contact and close to $y = 0\,\mathrm{nm}$ a spike is clearly visible, hinting at numerical instability.

When the current density is considered, the situation can be seen more clearly, as shown in Figures 4.23 and 4.24. While the two spikes in current density located directly at the corners of the source and drain contact are to be expected, in the highly doped spacer region on the drain side artificial oscillations are visible, especially close to the gate oxide but also at the BOX. While the cell averages of the current density show numerical artifacts even in the one-dimensional case, at least the cell surface current densities are smooth. However, for the two-dimensional case this does not seem to hold,

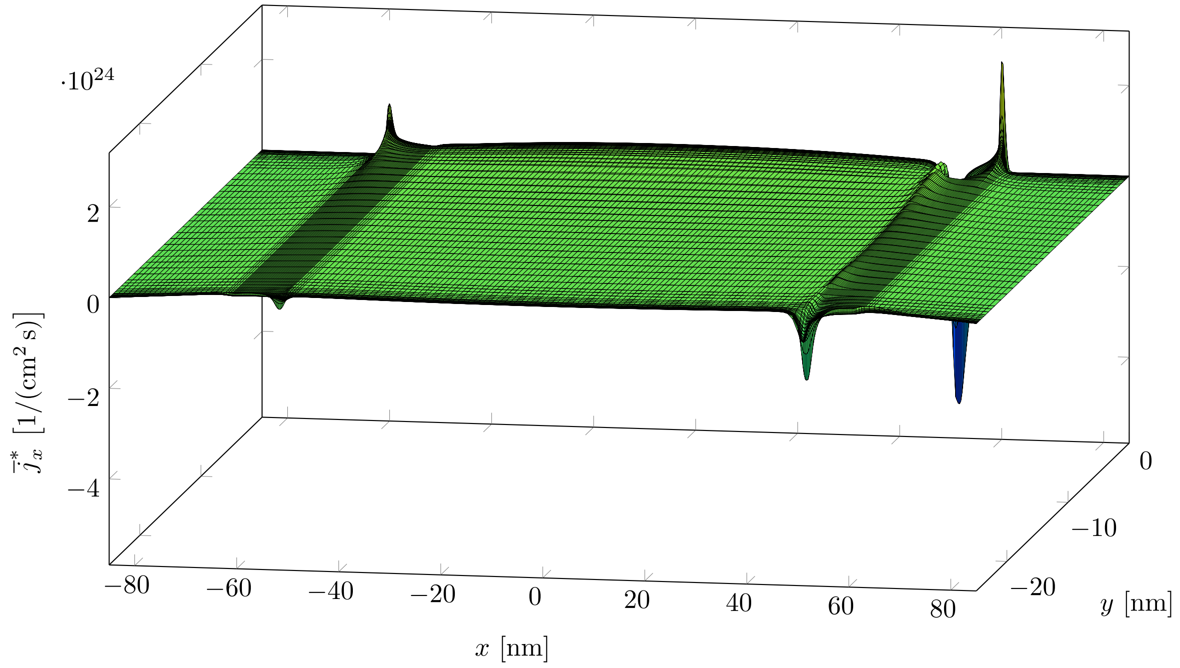

Figure 4.23: Face average current density in x-direction.

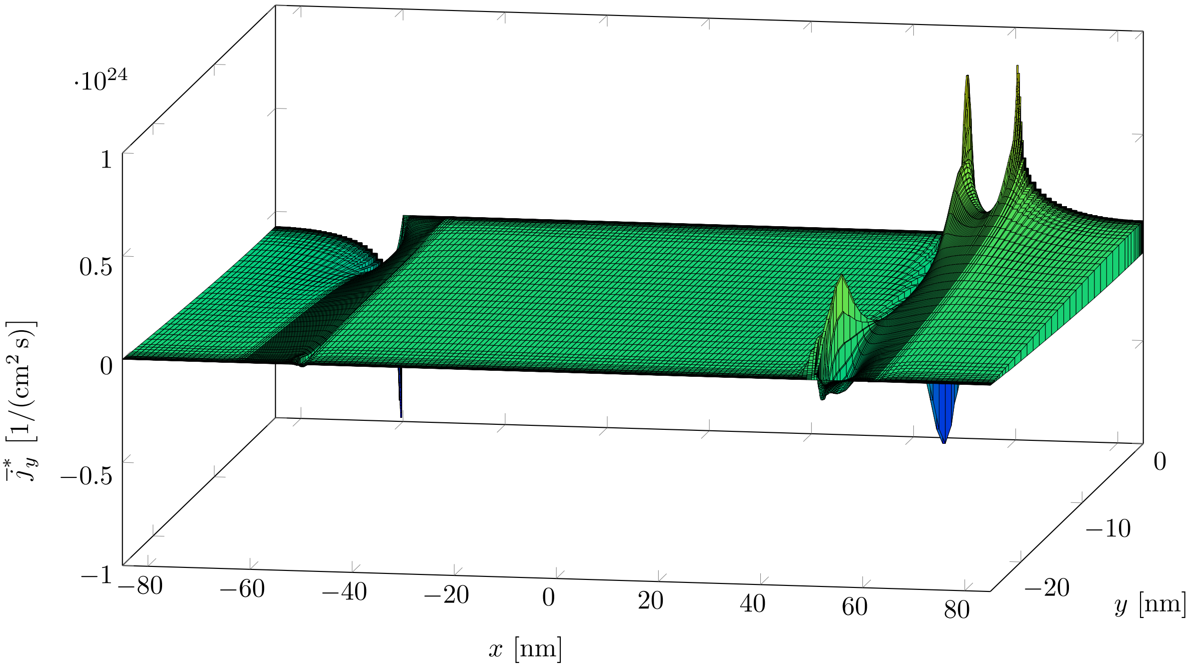

Figure 4.24: Face average current density in y-direction.

since in the figures already only the surface currents are shown.

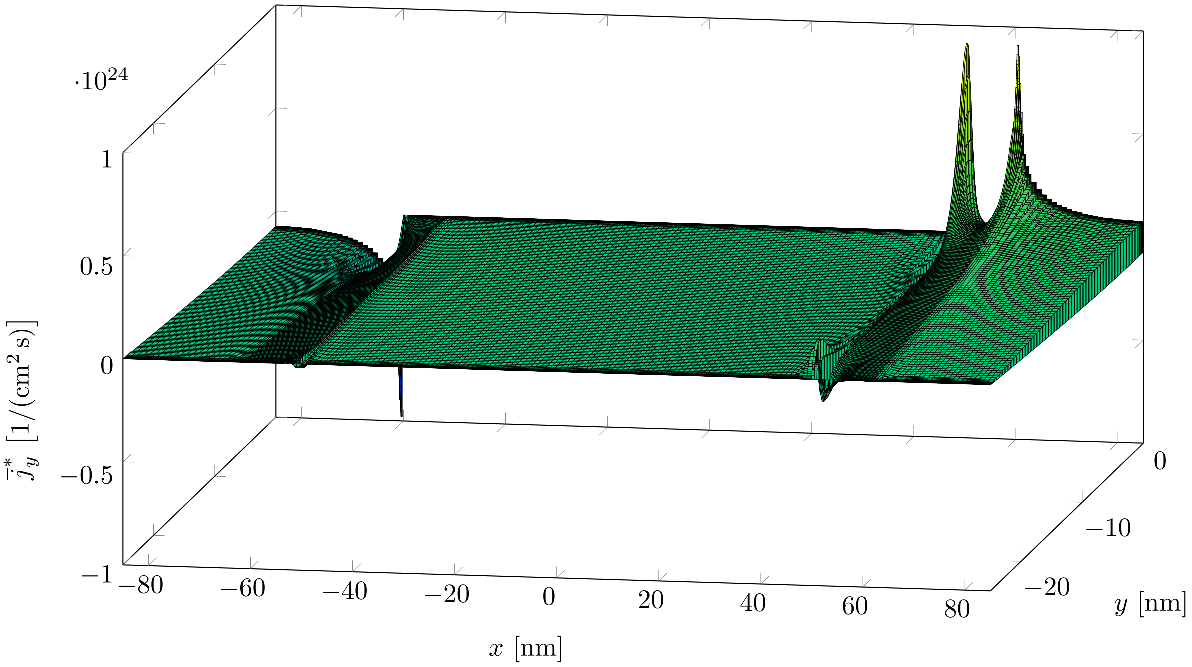

Figure 4.25: Face average current density in y-direction using a refined grid.

A strategy to suppress these instabilities could be the refinement of the grid. As shown in Figure 4.25, this actually works somewhat, and especially the instability close to the BOX at $y \approx -25\,\text{nm}$ is significantly reduced. Unfortunately, to fully suppress the instabilities, the grid would probably have to be multiple orders of magnitude finer, which quickly becomes computationally infeasible. For that reason, no further simulations for the fully two-dimensional case are presented here, since such results would be highly questionable, when the stationary case already appears to be numerically unstable.

5 Conclusion and Outlook

In this work several simpler models for electron transport in semiconductor devices were derived from the BTE and analyzed with special regard to plasma oscillations. For the homogeneous case, the models were compared to the BTE, and the plasma wave instability predicted by Dyakonov and Schur was investigated. It was found, that the convective hydrodynamic model is the most accurate and gives results most similar to the homogeneous BTE. The convective term was shown to be necessary to properly capture the anisotropy of the distribution function. Furthermore, the influence of the boundary conditions was investigated, leading to the conclusion that the instability is presumably just an artifact due to improperly chosen boundary conditions.

In the next part of the thesis, numerical device simulations were performed. Approximations usually done for numerical stabilization purposes could not be made, and typically used schemes proved to be unstable under these aggravated conditions. Therefore, an entirely new discretization scheme had to be developed, and it was successfully applied to purely one-dimensional devices.

After this, the discretization was extended to two dimensions. Starting with a two-dimensional PE, a double-gate MOSFET with one-dimensional transport was investigated. By performing large-signal simulations, the influence of the convective derivative under dynamic conditions for frequencies in the THz-range could be demonstrated successfully.

As the final step, the discretization scheme for the transport model was extended to two dimensions as well. Unfortunately, the scheme proved to be too unstable to be used for transient simulations. While the refinement of the grid could improve the situation somewhat, it would be computationally infeasible to completely suppress the numerical instabilities; especially considering that the simplified transport models considered in this work are supposed to be more efficient to simulate than the BTE.

The problem seems to be the collocation of scalar and vectorial quantities, i.e. the solution variables for the density and current density are defined on the same grid primitives (grid cells). In the case of the Scharfetter-Gummel stabilization for the simple drift-diffusion model, a staggered grid is used instead, where the current densities are calculated for the adjoint grid points. However, when the convective derivative is included in the model, this approach leads to further problems, since both the density and current density are needed at the same position to evaluate that term. This results in the need for some kind of interpolation, which introduces further instability and ultimately renders it unusable for this case.

A transport model, which only contains scalar quantities would be the BTE, discretized in $\boldsymbol{k}$-space. Even though it is expected to be computationally far more expensive, due to its higher dimensionality, the underlying structure could be considered quite a bit simpler than the CDD model, since the flux term contains no non-linearity. In the future it would be quite interesting to apply the insights developed in this work to the BTE instead, hopefully resulting in a more stable, as well as physically more accurate solution. Especially the non-negative reconstruction procedure could be valuable in developing a high-order scheme for the BTE, since its distribution function also has the requirement to always stay non-negative.

Bibliography

[1] T. Linn, Z. Kargar, and C. Jungemann, "Investigation of moments-based transport models applied to plasma waves and the Dyakonov–Shur instability," Semiconductor Science and Technology, vol. 34, no. 1, p. 014002, 2018.

[2] T. Linn, K. Bittner, H.-G. Brachtendorf, and C. Jungemann, "Simulation of THz oscillations in semiconductor devices based on balance equations," Journal of scientific computing, vol. 85, no. 1, pp. 1–15, 2020.

[3] C. Jungemann, T. Linn, K. Bittner, and H.-G. Brachtendorf, "Numerical investigation of plasma effects in silicon MOSFETs for THz-wave detection," Solid-State Electronics, vol. 128, pp. 129–134, 2017.

[4] Z. Kargar, T. Linn, D. Ruić, and C. Jungemann, "Investigation of transport modeling for plasma waves in THz devices," IEEE Transactions on Electron Devices, vol. 63, no. 11, pp. 4402–4408, 2016.

[5] Z. Kargar, D. Ruić, T. Linn, and C. Jungemann, "Numerical simulation of plasma waves in a quasi-2D electron gas based on the Boltzmann transport equation," Journal of Computational Electronics, vol. 16, no. 3, pp. 487–496, 2017.

[6] Z. Kargar, T. Linn, and C. Jungemann, "Investigation of the Dyakonov–Shur instability for THz wave generation based on the Boltzmann transport equation," Semiconductor Science and Technology, vol. 33, no. 10, p. 104001, 2018.

[7] M. Noei, T. Linn, and C. Jungemann, "A numerical approach to quasi-ballistic transport and plasma oscillations in junctionless nanowire transistors," Journal of Computational Electronics, vol. 19, no. 3, pp. 975–986, 2020.

[8] M. Noei, T. Linn, P. Luckner, and C. Jungemann, "A Godunov-type stabilization scheme for large-signal simulations of a THz nanowire transistor based on the

Boltzmann equation," IEEE Transactions on Electron Devices, vol. 68, no. 11, pp. 5407–5413, 2021.

[9] M. Noei, P. Luckner, T. Linn, and C. Jungemann, "Numerical aspects of a Godunov-type stabilization scheme for the Boltzmann transport equation," Journal of Computational Electronics, in press.

[10] U. Pfeiffer, Y. Zhao, J. Grzyb, R. Al Hadi, N. Sarmah, W. Förster, H. Rücker, and B. Heinemann, "A 0.53 THz reconfigurable source module with up to 1 mW radiated power for diffuse illumination in terahertz imaging applications," IEEE Journal of Solid-State Circuits, vol. 49, no. 12, pp. 2938–2950, 2014.

[11] J. Grzyb, K. Statnikov, R. Al Hadi, and U. Pfeiffer, "All-silicon integrated THz harmonic source and receiver components for future active imaging modalities," in 2014 39th International Conference on Infrared, Millimeter, and Terahertz waves (IRMMW-THz). IEEE, 2014, pp. 1–2.

[12] T. Otsuji and M. Shur, "Terahertz plasmonics: Good results and great expectations," IEEE Microwave Magazine, vol. 15, no. 7, pp. 43–50, 2014.

[13] M. Dyakonov and M. Shur, "Shallow water analogy for a ballistic field effect transistor: New mechanism of plasma wave generation by dc current," Phys. Rev. Lett., vol. 71, pp. 2465–2468, Oct 1993.

[14] M. Dyakonov and M. Shur, "Plasma wave electronics: Novel terahertz devices using two dimensional electron fluid," Electron Devices, IEEE Transactions on, vol. 43, no. 10, pp. 1640–1645, Oct 1996.

[15] V. Popov, G. Tsymbalov, and M. Shur, "Plasma wave instability and amplification of terahertz radiation in field-effect-transistor arrays," Journal of Physics: Condensed Matter, vol. 20, no. 38, p. 384208, 2008.

[16] G. Aizin, J. Mikalopas, and M. Shur, "Current-driven plasmonic boom instability in three-dimensional gated periodic ballistic nanostructures," Physical Review B, vol. 93, no. 19, p. 195315, 2016.

[17] U. Pfeiffer and E. Ojefors, "A 600-GHz CMOS focal-plane array for terahertz imaging applications," in ESSCIRC 2008-34th European Solid-State Circuits Conference. IEEE, 2008, pp. 110–113.

[18] E. Öjefors, U. Pfeiffer, A. Lisauskas, and H. Roskos, “A 0.65 THz focal-plane array in a quarter-micron CMOS process technology,” Solid-State Circuits, IEEE Journal of, vol. 44, no. 7, pp. 1968–1976, July 2009.

[19] R. Al Hadi, J. Grzyb, B. Heinemann, and U. Pfeiffer, “Terahertz detector arrays in a high-performance SiGe HBT technology,” in 2012 IEEE Bipolar/BiCMOS Circuits and Technology Meeting (BCTM). IEEE, 2012, pp. 1–4.

[20] M. Dyakonov and M. Shur, “Detection, mixing, and frequency multiplication of terahertz radiation by two-dimensional electronic fluid,” Electron Devices, IEEE Transactions on, vol. 43, no. 3, pp. 380–387, Mar 1996.

[21] O. Madelung, Introduction to Solid State Theory. Springer, 1978.

[22] C. Jungemann and B. Meinerzhagen, Hierarchical Device Simulation: The Monte-Carlo Perspective, ser. Computational Microelectronics. Wien, New York: Springer, 2003.

[23] R. Stratton, “Diffusion of hot and cold electrons in semiconductor barriers,” Physical Review, vol. 126, no. 6, p. 2002, 1962.

[24] K. Bløtekjær, “Transport equations for electrons in two-valley semiconductors,” Electron Devices, IEEE Transactions on, vol. 17, no. 1, pp. 38–47, 1970.

[25] N. G. Van Kampen, Stochastic processes in physics and chemistry. Elsevier, 1981, vol. 1.

[26] R. Thoma, A. Emunds, B. Meinerzhagen, H.-J. Peifer, and W. Engl, “Hydrodynamic equations for semiconductors with nonparabolic band structure,” IEEE transactions on electron devices, vol. 38, no. 6, pp. 1343–1353, 1991.

[27] R. Brunetti, C. Jacoboni, F. Nava, L. Reggiani, G. Bosman, and R. Zijlstra, “Diffusion coefficient of electrons in silicon,” Journal of Applied Physics, vol. 52, no. 11, pp. 6713–6722, 1981.

[28] C. Jungemann, A. Pham, B. Meinerzhagen, C. Ringhofer, and M. Bollhöfer, “Stable discretization of the Boltzmann equation based on spherical harmonics, box integration, and a maximum entropy dissipation principle,” Journal of applied physics, vol. 100, no. 2, p. 024502, 2006.

[29] S.-M. Hong and C. Jungemann, “A fully coupled scheme for a Boltzmann-Poisson equation solver based on a spherical harmonics expansion,” Journal of computational electronics, vol. 8, no. 3, pp. 225–241, 2009.

[30] S.-M. Hong, G. Matz, and C. Jungemann, “A deterministic Boltzmann equation solver based on a higher order spherical harmonics expansion with full-band effects,” IEEE transactions on electron devices, vol. 57, no. 10, pp. 2390–2397, 2010.

[31] S.-M. Hong, A.-T. Pham, and C. Jungemann, Deterministic solvers for the Boltzmann transport equation, ser. Computational Microelectronics, S. Selberherr, Ed. Wien, New York: Springer Science & Business Media, 2011.

[32] L. D. Landau and E. M. Lifshitz, Fluid Mechanics. Pergamon, New York, 1966.

[33] M. Nekovee, B. J. Geurts, H. M. Boots, and M. F. Schuurmans, “Failure of extended-moment-equation approaches to describe ballistic transport in submicrometer structures,” Physical Review B, vol. 45, no. 12, p. 6643, 1992.

[34] C. Jungemann, T. Grasser, B. Neinhuus, and B. Meinerzhagen, “Failure of moments-based transport models in nanoscale devices near equilibrium,” IEEE Transactions on Electron Devices, vol. 52, no. 11, pp. 2404–2408, 2005.

[35] R. S. Varga, Matrix Iterative Analysis, ser. Series in Automatic Computation. Englewood Cliffs, New Jersey: Prentice-Hall, 1962.

[36] S. Selberherr, Analysis and Simulation of Semiconductor Devices. Wien: Springer, 1984.

[37] G. H. Golub and J. H. Welsch, “Calculation of Gauss quadrature rules,” Mathematics of computation, vol. 23, no. 106, pp. 221–230, 1969.

[38] C. Runge, “Über empirische funktionen und die interpolation zwischen äquidistanten ordinaten,” Zeitschrift für Mathematik und Physik, vol. 46, no. 224-243, p. 20, 1901.

[39] D. Scharfetter and H. Gummel, “Large-signal analysis of a silicon Read diode oscillator,” IEEE Transactions on Electron Devices, vol. 16, no. 1, pp. 64–77, 1969.

[40] S. K. Godunov, “A difference method for numerical calculation of discontinuous solutions of the equations of hydrodynamics,” Matematicheskii Sbornik, vol. 89, no. 3, pp. 271–306, 1959.

[41] P. D. Lax, “Weak solutions of nonlinear hyperbolic equations and their numerical computation,” Communications on pure and applied mathematics, vol. 7, no. 1, pp. 159–193, 1954.

[42] H. Bateman, “Some recent researches on the motion of fluids,” Monthly Weather Review, vol. 43, no. 4, pp. 163–170, 1915.

[43] J. M. Burgers, “A mathematical model illustrating the theory of turbulence,” in Advances in applied mechanics. Elsevier, 1948, vol. 1, pp. 171–199.

[44] W. J. M. Rankine, “XV. On the thermodynamic theory of waves of finite longitudinal disturbance,” Philosophical Transactions of the Royal Society of London, vol. 160, pp. 277–288, 1870.

[45] H. Hugoniot, “Memoir on the propagation of movements in bodies, especially perfect gases (first part),” J. de l’Ecole Polytechnique, vol. 57, no. 3, 1887.

[46] H. Hugoniot, “Memoir on the propagation of movements in bodies, especially perfect gases (second part),” J. de l’Ecole Polytechnique, vol. 58, no. 1, 1889.

[47] E. F. Toro, Riemann solvers and numerical methods for fluid dynamics: a practical introduction. Springer Science & Business Media, 2013.

[48] P. L. Roe, “Approximate Riemann solvers, parameter vectors, and difference schemes,” Journal of computational physics, vol. 43, no. 2, pp. 357–372, 1981.

[49] A. Harten and J. M. Hyman, “Self adjusting grid methods for one-dimensional hyperbolic conservation laws,” Journal of computational physics, vol. 50, no. 2, pp. 235–269, 1983.

[50] R. J. LeVeque and R. J. Leveque, Numerical methods for conservation laws. Springer, 1992, vol. 132.

[51] M. Pelanti, L. Quartapelle, and L. Vigevano, “A review of entropy fixes as applied to Roe’s linearization,” Teaching material of the Aerospace and Aeronautics Department of Politecnico di Milano, 2001.

[52] P. Degond and P. A. Markowich, "On a one-dimensional steady-state hydrodynamic model for semiconductors," Applied Mathematics Letters, vol. 3, no. 3, pp. 25–29, 1990.

[53] G. Irene Martínez, "Stationary transonic solutions of a one–dimensional hydrodynamic model for semiconductors," Communications in Partial Differential Equations, vol. 17, no. 3-4, pp. 225–267, 1992.

[54] J. M. Greenberg and A.-Y. LeRoux, "A well-balanced scheme for the numerical processing of source terms in hyperbolic equations," SIAM Journal on Numerical Analysis, vol. 33, no. 1, pp. 1–16, 1996.

[55] R. J. LeVeque, "A well-balanced path-integral f-wave method for hyperbolic problems with source terms," Journal of scientific computing, vol. 48, no. 1, pp. 209–226, 2011.

[56] P. Jenny and B. Müller, "Rankine–Hugoniot–Riemann solver considering source terms and multidimensional effects," Journal of Computational Physics, vol. 145, no. 2, pp. 575–610, 1998.

[57] P. Goatin and P. G. LeFloch, "The Riemann problem for a class of resonant hyperbolic systems of balance laws," Annales de l'Institut Henri Poincaré (C) Non Linear Analysis, vol. 21, no. 6, pp. 881–902, 2004.

[58] P. G. LeFloch and M. D. Thanh, "A Godunov-type method for the shallow water equations with discontinuous topography in the resonant regime," Journal of Computational Physics, vol. 230, no. 20, pp. 7631–7660, 2011.

[59] G. Wanner and E. Hairer, Solving ordinary differential equations II. Springer Berlin Heidelberg, 1996, vol. 375.

[60] H. K. Gummel, "A self-consistent iterative scheme for one-dimensional steady state transistor calculations," IEEE Transactions on electron devices, vol. 11, no. 10, pp. 455–465, 1964.

[61] D. M. Caughey and R. E. Thomas, "Carrier mobilities in silicon empirically related to doping and field," IEEE Proc., vol. 55, no. 12, pp. 2192–2193, 1967.

[62] S. Godunov, "Difference methods for shock waves," Ph.D. dissertation, Ph. D. dissertation, Moscow State University, Moscow, Russia, 1954.

[63] R. Artebrant and H. J. Schroll, "Limiter-free third order logarithmic reconstruction," SIAM Journal on Scientific Computing, vol. 28, no. 1, pp. 359–381, 2006.

[64] W. Shockley, "Currents to conductors induced by a moving point charge," J. Appl. Phys., vol. 9, pp. 635–636, 1938.

[65] S. Ramo, "Currents induced by electron motion," Proc. IRE, vol. 27, pp. 584–585, 1939.

[66] H. Kim, H. S. Min, T. W. Tang, and Y. J. Park, "An extended proof of the Ramo-Shockley theorem," Solid–State Electron., vol. 34, pp. 1251–1253, 1991.

[67] R. Piessens, E. de Doncker-Kapenga, C. W. Überhuber, and D. K. Kahaner, QUADPACK: A Subroutine Package for Automatic Integration. Springer Berlin Heidelberg, 1983.

[68] C. Jungemann, K. Bittner, and H.-G. Brachtendorf, "Simulation of plasma resonances in MOSFETs for THz-signal detection," in 2016 Joint International EUROSOI Workshop and International Conference on Ultimate Integration on Silicon (EUROSOI-ULIS), 2016, pp. 48–51.

[69] C. F. Curtiss and J. O. Hirschfelder, "Integration of stiff equations," Proceedings of the National Academy of Sciences of the United States of America, vol. 38, no. 3, p. 235, 1952.

[70] C. W. Gear, "Numerical initial value problems in ordinary differential equations," Prentice-Hall series in automatic computation, 1971.

[71] H.-G. Brachtendorf and K. Bittner, "Grid size adapted multistep methods for high q oscillators," IEEE Transactions on Computer-Aided Design of Integrated Circuits and Systems, vol. 32, no. 11, pp. 1682–1693, 2013.

[72] R. J. Gilmore and M. B. Steer, "Nonlinear circuit analysis using the method of harmonic balance — A review of the art. Part I. introductory concepts," International Journal of Microwave and Millimeter-Wave Computer-Aided Engineering, vol. 1, no. 1, pp. 22–37, 1991.